# Deformation Mechanisms in B2 Aluminides; Shear Faults and Dislocation Core Structures in FeAl, NiAl, CoAl and FeNiAl

by

Christophe N. P. Vailhé

Dissertation submitted to the faculty of the

Virginia Polytechnic Institute and State University

in partial fulfillment of the requirements for the degree of

## DOCTOR OF PHILOSOPHY

in

Materials Science and Engineering
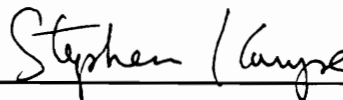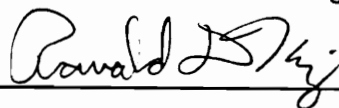
©Christophe N. P. Vailhé and VPI & SU 1996
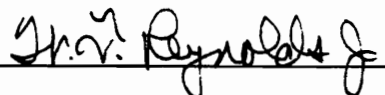
APPROVED:

_____

Dr. Diana Farkas, Chairperson

_____     _____

Dr. Alex O. Aning                    Dr. Stephen L. Kampe

_____     _____

Dr. Ronald D. Kriz                  Dr. William T. Reynolds

March, 1996

Blacksburg, Virginia

KEYWORDS: Dislocations, Intermetallics, Ductility, Atomistic Simulations, In-Situ TEM

c.2

LD
5655
V856
1996
V355
c.2

# Deformation Mechanisms in B2 Aluminides; Shear Faults and Dislocation Core Structures in FeAl, NiAl, CoAl and FeNiAl

by

Christophe N. P. Vailhé

Committee Chairperson: Dr. Diana Farkas

Materials Engineering Science

## (ABSTRACT)

Although aluminides with the B2 crystal structures have good properties for high temperature applications, the strong ordered bonds that make them durable at high temperature also make them too brittle at room temperature for industrial fabrication. In order to better understand this lack of ductility, molecular statics simulations of planar fault defects and dislocation core structures were conducted in a series of B2 aluminides with increasing ordering energy (FeAl, NiAl, CoAl). The simulation results in NiAl were compared with in-situ straining observations of dislocation motion.

The dislocations simulated were of $\langle 100 \rangle$ and $\langle 111 \rangle$ types. The simulations results obtained indicate a strong influence of the planar fault energies on the mobility of the dislocations. As the cohesive energy increases from FeAl to CoAl, antiphase boundary and unstable stacking fault energies increase resulting in more constricted dislocation core spreadings. This constriction of the cores decreases the mobility of dislocation with planar core structures and increases the mobility of dislocations with non-planar cores.

The $\langle 100 \rangle$ screw dislocations were found with planar cores in $\{110\}$ planes for FeAl, NiAl and CoAl. For very high APB values, the cores were very compact, as predicted by the Peierls- Nabarro model. As the APB energies decrease, increasingly two dimensional spreading of the cores was observed and ultimately dislocation dissociation into partials. As a result of the deviation of the stable planar fault energy from the APB fault, the partials were not exact $1/2\langle 111 \rangle$ but deviate to the point corresponding to the actual minima of the $\gamma$-surfaces for these compounds. Alloying NiAl with Fe was found to promote the dissociation of the $\langle 100 \rangle$ dislocation.

The in-situ straining of a single crystal of NiAl only revealed the motion of $\langle 100 \rangle$ dislocations. Both in-situ observations and atomistic simulations agreed on the zig-zag shape of the $\langle 100 \rangle$ dislocation with an average screw orientation. In this configuration, the mobility of the dislocation is severely reduced.

# ACKNOWLEDGEMENTS

This research has been made possible thanks to the great help, guidance and friendship of my advisor, Dr. Diana Farkas. I also wish to thank my committee members, Dr. A. Aning, Dr. S. Kampe, Dr. R. Kriz and Dr. W. Reynolds for their suggestions and help.

For showing me the beauty of in-situ straining experiments, I especially thank Dr. D. Caillard, Dr. G. Molenat and Dr. A. Couret from the Centre d'Elaboration de Materiaux et d'Etudes Structurales in Toulouse (Merci à tous).

For the congenial atmosphere and their help, I wish to thank my office-mates: Chris Jones, Batsirai Mutasa, Julia Panova, Kevin Ternes, Vijay Shastry, Yuri Mishin, Anne Vilette. We all came from different countries, united in a common battle to smooth the brittle edge of these intermetallics.

I could not finish these acknowledgments without thinking about some good friends from the department: Dilip Vijay, Ashraf Khan, Justin Gainor, Greg Menk ... Thank you for your friendship.

Finally but not least, I would like to thank my "pétillante" wife, Elizabeth, for her support and understanding, and her monster cat, Jody, for waking me up every night.

I also wish to thank my family for their help and support.

iv

# TABLE OF CONTENTS

*CONTENTS*

# LIST OF FIGURES

## LIST OF FIGURES

## LIST OF FIGURES

# LIST OF TABLES

## 0.1 INTRODUCTION

The development of performing intermetallics is mainly directed by the aerospace industry. A first objective is to find lighter materials that can replace conventional superalloys for application at temperatures up to 900°c. Efforts are especially directed towards developing the skin and structural parts of the National Aerospace Plane where friction caused by hypersonic flight can bring the temperature up to 800°c. A second objective is to increase the operating temperature of engines towards the ultimate 2200°c where combustion of jet fuel is most efficient. Development of high temperature materials at low cost would also have a direct application in the automotive industry by suppression of the cooling systems. To achieve this goal, new materials that can withstand higher temperatures have to be developed since engine efficiency is now limited by the melting point of superalloys or brittleness of ceramic materials.

Among high temperature materials, intermetallics present interesting properties scaled between those of superalloys and ceramics. They have high melting temperatures, low density and good corrosion resistance. One of the primary problems encountered in their development is that the strong, ordered bonds that make intermetallics more durable at higher temperature compared to superalloys also make them brittle at room temperature. Unlike in ceramics, a limited ductility can be achived through alloying and processing.

Among intermetallic alloys, aluminides with the B2 crystal structure present excellent properties for high temperature applications. In order to understand the mechanisms controlling the plastic deformation of these intermetallics, atomistic simulations of crystal defects have been successfuly conducted, especially in the Ni-Al system. The purpose of these simulations is to compute the unstable stacking fault energies and the dislocation core structures that are known to influence the dislocation mobility. Such parameters are only accessible through atomistic simulation. This study presents the results of atomistic simulations of planar faults and dislocations in a series of B2 aluminides. The compounds simulated, FeAl, NiAl and CoAl, have increasing ordering energy and decreasing fracture

toughness.

The successful approaches to solve the ductility problem in intermetallic alloys are reported in Chapter 1. This chapter also reports the results obtained from previous experimetal observations, atomistic simulations and modeling of dislocations in the B2 aluminides. The interatomic potentials and embedded atom method used in this study for the simulations of the crystal defects are presented in Chapter 2. The simulation results for the planar fault energies along the {110} and {112} planes in FeAl, NiAl and CoAl are reported in Chapter 3. Chapter 4 presents the simulated core structures for the $\langle 100 \rangle$ and $\langle 111 \rangle$ dislocations in FeAl and CoAl. The results were compared with the experimental observation of slip systems in these compounds. The results were also analyzed to identify the trends in the simulated material properties.

In order to explain the lack of ductility in NiAl, in-situ experimental observation of dislocations in a single crystal of NiAl was conducted at the CNRS Laboratory (France) as part of this work. The characteristics of the observed dislocations and their behavior under an applied stress are described in Chapter 5.

The study on the strain in the $\langle 100 \rangle$ dislocation cores in FeAl, NiAl and CoAl is described in Chapter 6. The mobility of the dislocations simulated was rationalized in terms of the shape of the core structures and the unstable stacking fault energies along the slip plane. The validity of the Peierls-Nabarro model for the planar cores simulated is also discussed.

Finally, the $\langle 100 \rangle$ screw dislocations were simulated in a ternary B2 Ni-35Al-12Fe system. The developement of interatomic potentials for this system was driven by the experiemtal observation of ductility in these ternary alloys. The developement of the interatomic potentials and the results of the dislocation simulations are reported in Chapter 7.

# Chapter 1
# LITERATURE SURVEY

## 1.1 METALLURGY OF HIGH TEMPERATURE INTERMETALLICS

The development of structural alloys for high temperature applications is a difficult exercise due to the overall balance of engineering properties required. A perfect high temperature alloy should be strong and creep resistant at high temperature. The material also has to be tough enough at room temperature to avoid crack initiation during formation and temperature cycles experienced in its life time. After fifty years of development of nickel and titanium superalloys, they have become state of the art materials for high temperature applications. There are no other structural materials capable of a service temperature as close to their melting points as the superalloys.

To be in competition with superalloys, high temperature intermetallics must offer high temperature strength and oxidation resistance together with room temperature ductility and low density. Efforts have been especially concentrated on the improvement of room temperature ductility of nickel and titanium aluminides (see Table 1.1). As presented in the following examples, controlling the room temperature ductility of these intermetallics is a difficult task which has some consequences on the initial material properties.

### 1.1.1 Ti$_3$Al and TiAl Based Intermetallics

Among intermetallics, Ti$_3$Al is in the most advanced stage of development. Both Pratt & Whitney and General Electric produce a ductile version of Ti$_3$Al usable up to 700-800 °C which is currently being tested by several turbine builders [8]. Hexagonal DO$_{19}$ Ti$_3$Al compound is brittle by nature and industrial applications would not have been possible

without the discovery of a ductile multiphase form of this intermetallic [9]. The ductile TiAl alloys have two phases, $\alpha_2$ (Ti$_3$Al) and $\beta$ (Ti-Al-Nb). Niobium, which substitutes titanium (10-30% in overall alloy), enhances the majority of the material properties with the exception of creep performance [5]. In other words, the increase in Nb percentage increases ductility at room temperature but decreases high temperature creep resistance. Niobium can be replaced by Mo, Ta or Cr for improved strength, Mo for creep resistance or Ta and Mo for oxidation resistance. Still, the application temperature cannot exceed 800 °C.

The ductility in these multiphase alloys is strongly related to the control of the distribution and morphology of the $\beta$ phase through alloying and processing. It is important to notice that $\alpha_2$ is the strengthening phase and the deformability is insured by the presence of the second phase, $\beta$. Reviews of the recent development of the two phases TiAl alloys [5, 10, 11, 6] emphasize the importance to produce an elongated plate-like $\alpha_2$ microstructure to obtain the optimum balance of room temperature ductility and elevated temperature properties. However, the mechanisms responsible for the increase in ductility at room temperature are still unclear.

TiAl also has some interesting properties for high temperature structural material applications [5, 10, 11, 6]. It has low density and good oxidation resistance as a result of the 50% Al content, associated with high specific strength and high modulus. Two kinds of alloys have been developed based on this compound: A single phase $\gamma$ (L1$_0$) and two phase $\gamma$ (L1$_0$ TiAl) + $\alpha_2$ (DO$_{19}$ Ti$_3$Al). Single phase $\gamma$ alloys contain a third element (1-10% of V,Cr,Mn) to promote strengthening and oxidation resistance but ductility at room temperature ($< 1\%$) has not been improved through alloying. As for Ti$_3$Al, enhanced ductility (2 to 5%) has been achieved in the development of two phase alloys, $\gamma + \alpha_2$ Ti-48Al, as a function of microstructure refinement.

In contrast with Ti$_3$Al, neither of the $\alpha_2$ and $\gamma$ phases are known to be ductile. One of the possible explanations for the enhanced ductility of the two phase alloys is that the $\alpha_2$ phase acts as a trap for interstitial impurities from the $\gamma$ matrix. Nevertheless it has not been

4

proven that very pure TiAl is intrinsically ductile. The other possible explanation comes from the formation of lamellar structure typical of the $\gamma + \alpha_2$ alloys. This microstructure is formed by the movement of Shockley partials that modify the stacking sequences of both phases. The success in the development of TiAl and $Ti_3Al$ alloys clearly shows the potential of multiphase alloys to improve room temperature ductility of intermetallics. However, the mechanisms through which the deformability is enhanced have not been identified.

## 1.1.2  $Ni_3Al$ and NiAl Based Intermetallics

A considerable amount of research has been devoted to the compound $Ni_3Al$ ($\gamma\prime$) for the reason that $Ni_3Al$ is the strengthening phase of many nickel based $\gamma + \gamma\prime$ superalloys [12]. $Ni_3Al$ ($L1_2$ structure) was one of the first intermetallics to be made ductile. A small addition of boron prevents the intergranular brittle fracture of the polycrystal material [13]. Unfortunately, $Ni_3Al$ oxidizes and becomes brittle around 600-700°C. To overcome the oxidation problem, a large amount of Cr has to be added and this makes the material more dense when compared to Ni-based superalloys. Second, $Ni_3Al$ shows poor strength and creep resistance at high temperature when compared with $\gamma$ - $\gamma\prime$ superalloys [11]. Strengthening of $Ni_3Al$ single crystals was obtained through the addition of Hf and Si but at the expense of ductility. These alloys are brittle in the temperature range 500-700°C.

Researchers have turned towards the cubic B2 structure of NiAl which has a higher melting temperature (1638°C) than TiAl and forms a better alumina surface coating preventing corrosion at high temperatures [14]. The higher percentage of aluminum in NiAl also ensures lower density than $Ni_3Al$ and $Ti_3Al$. NiAl applications could also emerge due to its high thermal conductivity which is four to eight times higher than in the Ni based superalloys. The poor mechanical strength and creep resistance of NiAl can be improved by adding a second phase $Ni_2AlTi$ to the B2 structure. The two phase alloys present better high temperature mechanical properties than the current nickel based superalloys. Nevertheless, the two phase alloys are even more brittle than single crystal NiAl and no solution has yet been found for its lack of ductility ($\sim$1%) at room temperature.

Unlike $Ni_3Al$, NiAl is believed to be intrinsically brittle due to the insufficient number of slip systems [2]. When deformation occurs, the grain boundaries rupture as a result of the stress concentration in the boundary. The attempts to improve ductility were directed towards the decrease of the grain size to put less stress on the grain boundary. NASA-Lewis and General Electric have obtained enhanced ductility by producing NiAl single crystals. Due to an unknown mechanism, tensile elongation is also increased from 1% to 6% in the $\langle 110 \rangle$ direction when the single crystals are doped with $\sim 1000$ ppm of Fe, Mo or Ga. Besides these successful developments, the $\langle 001 \rangle$ oriented crystals still exhibit essentially zero plastic strain to failure at temperatures below 330°C [15]. Because of the high potential of B2 NiAl, the mechanisms of deformation in B2 aluminides have been studied intensively and the results of these investigations are presented in the following section.

## 1.2 EXPERIMENTAL OBSERVATIONS ON THE MECHANISMS OF DEFORMATION IN B2 ALUMINIDES

Beside NiAl, other B2 aluminides, mainly FeAl and CoAl, have been studied not only for high temperature applications but also for comparison with NiAl [16, 17]. These intermetallics have the same B2 crystal structure (see Figure 1.1) and have very close lattice parameters ($\sim 2.8$ Å). One important property of this crystal structure is the existence of an Anti Phase Boundary (APB) which corresponds to a stable $1/2\langle 111 \rangle$ planar fault along the {110} and {112} planes. The existence of this stable stacking fault is the main difference between B2 intermetallics and b.c.c. metals. This fault that would bring back a b.c.c. crystal to the perfect lattice position generates a chemical disorder along the plane of fault in the B2 structure. Along the series of aluminides - FeAl, NiAl and CoAl - ordering energy and APB energy increases. In contrast, decreasing fracture toughness has been observed experimentally at room temperature from FeAl to CoAl [18] (see Table 1.1). These intermetallics also have different mechanisms of deformation which are presented below.

6
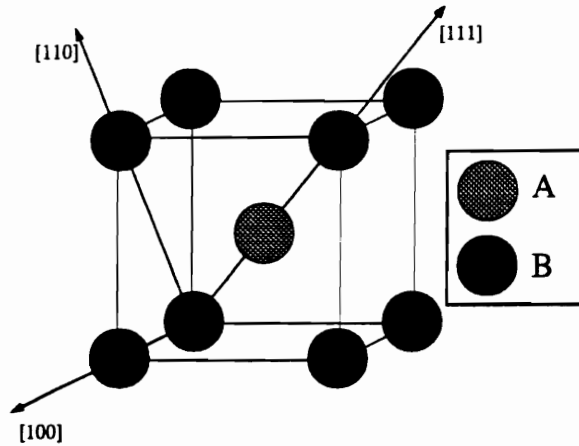
Figure 1.1: The B2 crystal structure for an AB compound.

Table 1.1: Properties of high temperature intermetallics [5, 6, 7].

| Intermetallics | Structure | Melting Temperature (°C) | Density g/cm$^3$ | Fracture Toughness $K_{1c}$ at RT (MPa$\sqrt{m}$) |
|---|---|---|---|---|
| Ti$_3$Al $\alpha_2$ | D0$_{19}$ | 800 † | 4.1-4.7 | 19 |
| TiAl $\gamma$ | L1$_0$ | 950 † | 3.7-3.9 | 12 |
| Ni$_3$Al | L1$_2$ | 1390 | 7.5 | |
| NiAl | B2 | 1640 | 5.92 | 4.5 |
| CoAl | B2 | 1638 | 6.08 | 3 |
| FeAl | B2 | 1330 | 5.6 | 12 |

†Tensile Creep Limit (°C)

### 1.2.1 NiAl Compound

Due to the amount of research concerning NiAl, a couple of reviews dedicated to the physical and mechanical properties of this intermetallic have been published recently [2, 15]. As can be seen from the phase diagram (Figure 1.2), significant deviations from stoichiometric composition are possible without altering the B2 crystal structure of NiAl. However, a minimum in flow stress and hardness and a corresponding maximum in ductility are observed at stoichiometric composition.

Possible Burgers vectors that do not disrupt the order of the B2 crystal lattice are $\langle 100 \rangle$, $\langle 110 \rangle$ and $\langle 111 \rangle$. The high ordering energy of NiAl prevents all other translation that would break the order of the lattice. All the Burgers vectors mentioned above have been observed experimentally. Nevertheless, the activation of these slip directions strongly depends on the orientation of the crystal with respect to the direction of loading. When stress is applied along $\langle 100 \rangle$, so called hard orientation, the stress necessary for deformation is many times higher than in any other non-$\langle 100 \rangle$ orientation. As a consequence, all other non-$\langle 100 \rangle$ loading directions are denoted as soft orientations.

Transmission electron microscopy and surface trace analysis performed on crystal deformed in tension and compression in the soft orientation revealed almost exclusive existence of $\langle 100 \rangle$ dislocations. The only slip systems responsible for deformation have been identified as $\langle 100 \rangle \{110\}$ and $\langle 100 \rangle \{100\}$, independent of deformation temperature and orientations. It is also important to mention that slip along the $\{100\}$ plane was only obtained for the $\langle 110 \rangle$ crystal orientation. Other high order slip planes with an orientation close to $\{100\}$, such as $\{210\}$, have also been reported based on trace analysis but it is believed that the slip traces observed were the result of an active cross-slip onto orthogonal $\{110\}$ slip planes.

In the hard orientation, the resolved shear stress for the $\langle 100 \rangle$ slip is close to zero and the stress required for deformation is several times greater than in any other orientation ($\sim$ 600 MPa versus $\sim$100 MPa in a soft orientation at room temperature). Below 600K, only $\langle 111 \rangle$ slip on $\{112\}$, $\{123\}$ or $\{110\}$ has been observed in compression tests. In contrast,
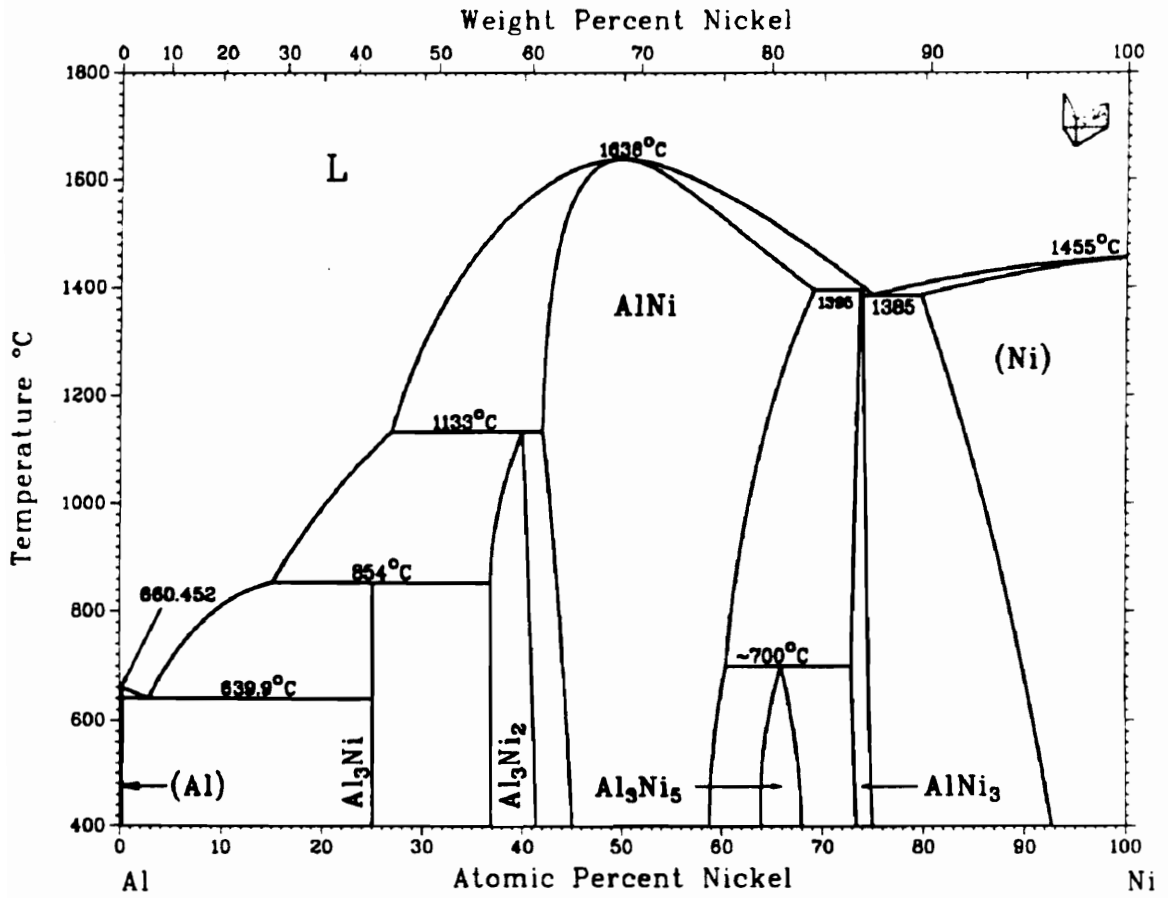
Figure 1.2: NiAl phase diagram from Nash [1].

at temperatures above 600K, ductility in tension can be achieved and the slip direction reported are $\langle 110 \rangle$ and $\langle 100 \rangle$. According to these observations on hard and soft orientation it is clear that $\langle 100 \rangle$ dislocations are the easiest ones to activate in the plastic deformation of NiAl single crystal at room temperature.

Finally, all the measurements of critical resolved shear stress as a function of temperature and dislocation type have been summarized by Miracle [2] in figure 1.3. The different symbols represented on these figures correspond to different studies. The results indicated with dark circles were obtained in the study of Ni-48Al and present systematic higher values of critical resolved shear stress at any temperature. This confirms the fact that off-stoichiometric alloys are known to be more brittle than stoichiometric NiAl.

The observed slip behavior observed in polycrystalline NiAl is very consistent with single crystal observations. Room temperature deformation of the polycrystal shows that $\langle 100 \rangle$ is the only active slip direction. Other Burgers vectors (essentially $\langle 110 \rangle$) were observed but they were probably created during the extrusion process or as a result of interactions between gliding $\langle 100 \rangle$ dislocations. There is no evidence that these $\langle 110 \rangle$ dislocations participate in the room temperature deformation. This indicates that the $\langle 100 \rangle$ $\{110\}$ slip system, which by itself contains three independent slip systems, does not meet the von Mises criterion for polycrystalline ductility (= five independent slip systems).

### 1.2.2 CoAl Compound

CoAl system has been subject to less investigation than NiAl because of its relative higher brittleness. In many respects both of these compounds are very similar. They have similar congruent melting point (1932K for NiAl and 1921K for CoAl), close lattice parameters (0.288 nm and 0.286 respectively) and similar density (5.92 g/cm$^3$ for NiAl versus 6.08 for CoAl). However, when compared to NiAl, CoAl is harder and has higher yield and creep strength.

The different mechanical behavior of CoAl has been attributed to the dislocation slip behavior and a greater internal lattice friction that lowers the dislocation mobility [19].
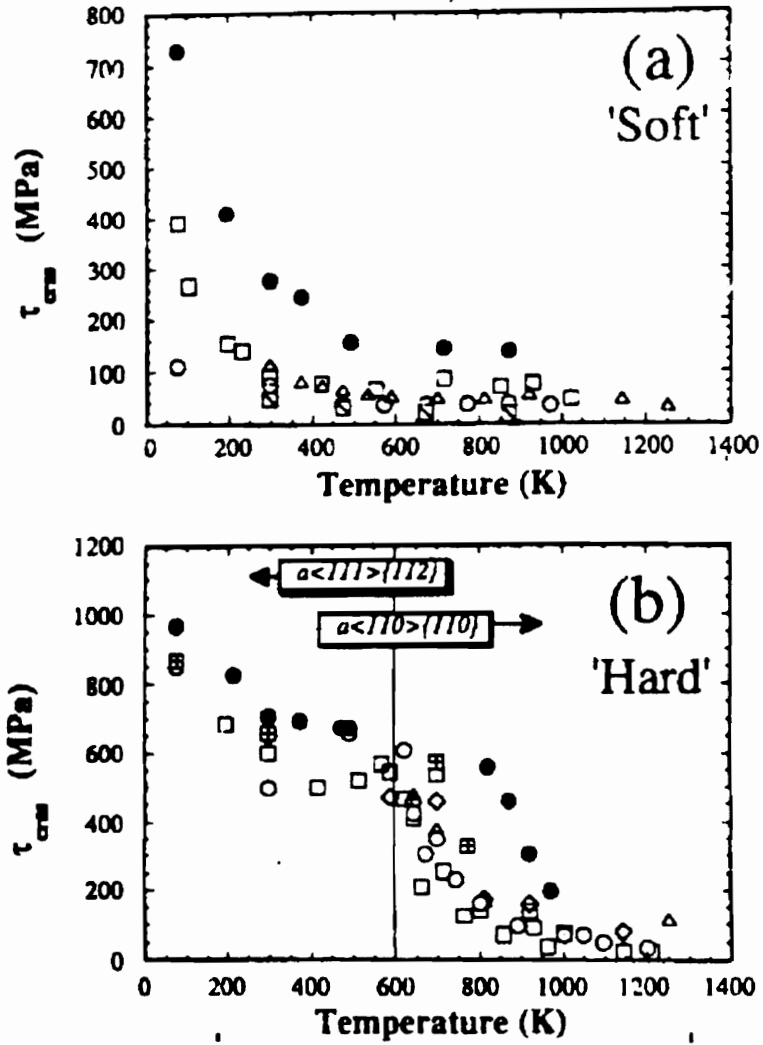
Figure 1.3: The critical resolved shear stress in NiAl single crystals for (a) $\langle 100 \rangle$ slip in soft orientation, (b) $\langle 111 \rangle$ $\{112\}$ and $\langle 110 \rangle$ $\{110\}$ slip in hard orientation [2].

11
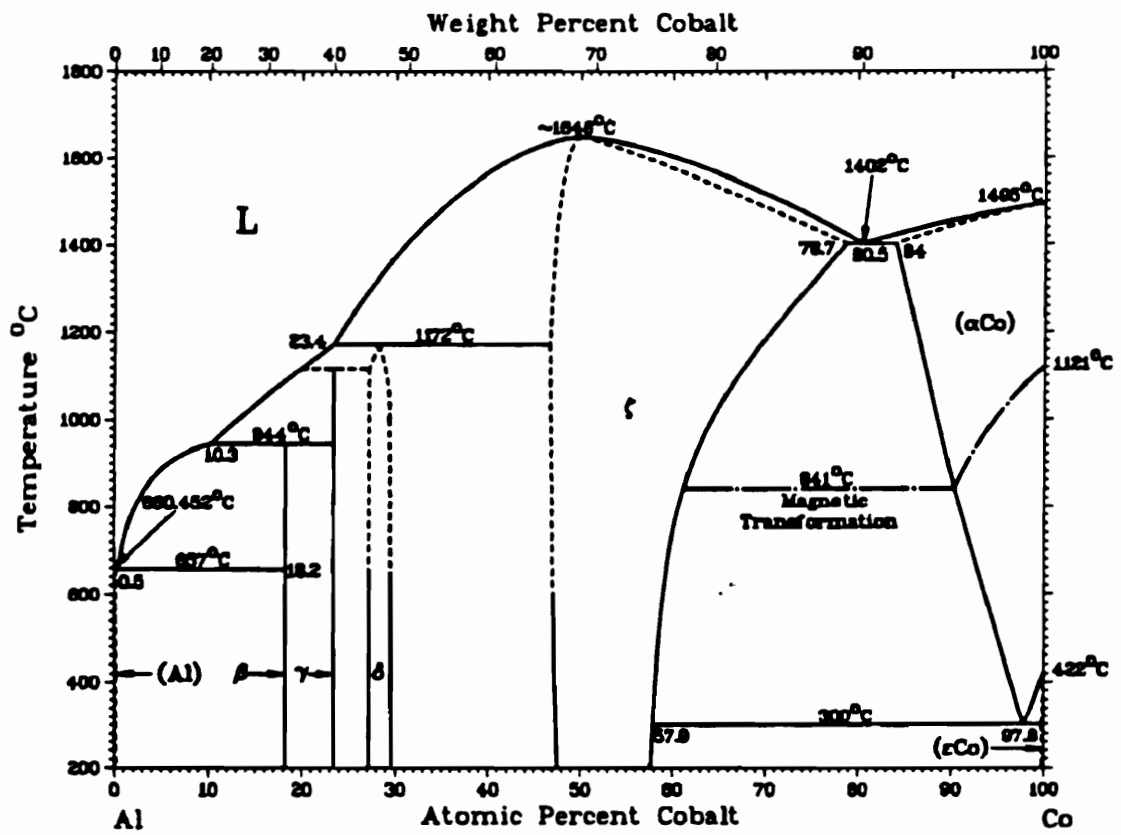
Figure 1.4: CoAl phase diagram

12

Nevertheless, dislocation characteristics have been the focus of very few investigations. Polycrystalline CoAl has been examined, revealing the existence and mobility of the $\langle 100 \rangle$ and $\langle 111 \rangle$ dislocations related to the high temperature 1505K extrusion process [20]. As in NiAl, dislocations were observed to move along the $\{110\}$ or $\{100\}$ planes in the polycrystal. In contrast to NiAl, $\langle 110 \rangle$ dislocations have never been observed in CoAl. Studies of dislocations have also been conducted in parallel with NiAl using single crystals deformed at 673K in the $\langle 110 \rangle$ orientation [17]. In agreement with the polycrystal observations, $\langle 100 \rangle$ slip was active at moderate temperatures and it was the only slip activated in these experimental conditions. In contrast, observation of the single crystal deformed at room temperature has revealed a large number of $\langle 111 \rangle$ dislocations [21].

### 1.2.3   FeAl Compound

FeAl has been studied more intensively than CoAl. It is now recognized that FeAl is intrinsically ductile and the commonly observed brittleness has been attributed to hydrogen embrittlement [22]. A transition temperature has also been identified in the mechanism of deformation of polycrystals. The principal slip is along $\langle 111 \rangle$ at temperatures below 0.4-0.5 $T_m$ and changes to $\langle 100 \rangle$ at higher temperatures. The temperature at which the transition occurs was seen to increase with increasing Al content for single crystals [23, 24] but decrease with increasing aluminum content in polycrystalline samples [25]. At present, this transition from $\langle 111 \rangle$ to $\langle 100 \rangle$ slip is not well understood.

As observed in NiAl and CoAl, the slip planes for the $\langle 100 \rangle$ dislocations have been identified as $\{100\}$ and $\{110\}$ [23]. At temperatures lower than the transition temperature, $\langle 111 \rangle$ dislocations can glide along $\{110\}$ and $\{112\}$ planes [25, 26]. As a result of the low antiphase boundary (APB) in FeAl, it is believed that the $\langle 111 \rangle$ dislocation dissociates into two $1/2\langle 111 \rangle$ superpartials separated by the APB. Dissociated $\langle 111 \rangle$ dislocations have been observed in Fe-35Al [27]. Nevertheless, as the aluminum content increases toward stoichiometric FeAl, ordering energy and APB energy increases in the B2 structure and $\langle 111 \rangle$ dislocations are closely dissociated or undissociated [28].

13
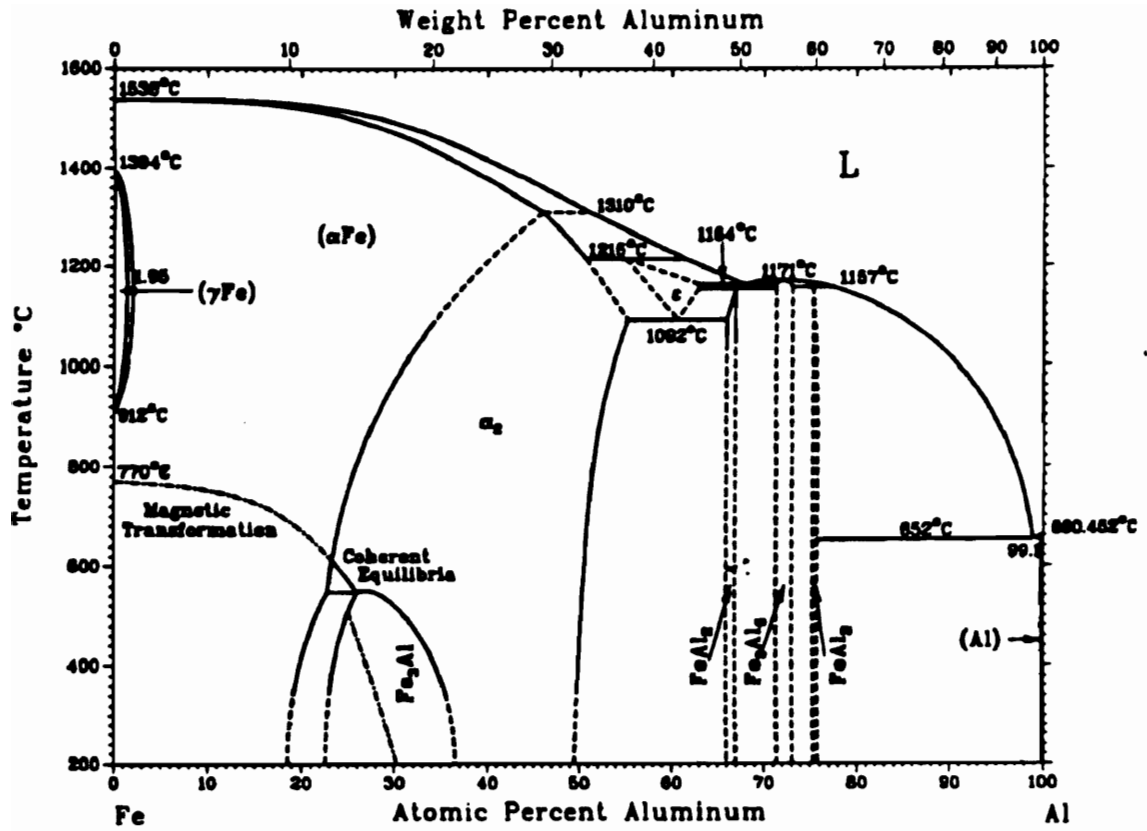
Figure 1.5: FeAl phase diagram

## 1.3 MODELING AND ATOMISTIC SIMULATION

The intrinsic brittleness of intermetallics such as NiAl and CoAl suggests that intricate details of dislocation motion and nucleation play a profound role in the deformation behavior of single crystals. In a continuous isotropic or anisotropic media, the strain and stress resulting from a dislocation can be accurately described using linear elasticity theory [29]. However, linear elasticity fails in the close vicinity of the dislocation line where atoms experience large displacements. The Peierls-Naborro dislocation model presents the advantage of describing the core structure of the dislocation in the discrete lattice. This model reveals the importance of the dislocation core structure on the dislocation properties. However, the Peierls-Nabarro nonlinear elastic model is now supplanted by atomic calculations of dislocation core structures.

### 1.3.1 Dislocation Dissociations and Elasticity Theory in the B2 Crystal Structure

In contrast with b.c.c. metals, the $1/2\langle 111 \rangle$ dislocation in the B2 structure is not a perfect dislocation. In the B2 structure, sublattice 1 and 2 (that can be seen as the corner and center of the cube) are respectively occupied by the atoms A and B. The $1/2\langle 111 \rangle$ dislocation, so called superpartial in the B2 structure, puts the A type atom in sublattice 2 and the B type atom in sublattice 1. As a result, dissociation of the $\langle 111 \rangle$ dislocation into a pair of superpartials creates a plane of chemical disorder in between the superpartials. This fault, called anti phase boundary (APB), is possible in $\{110\}$ and $\{112\}$ planes.

According to elasticity theory, the dislocation energy is proportional to the square of the Burgers vector. The two $1/2\langle 111 \rangle$ dislocations have lower energy than the complete $\langle 111 \rangle$ (Frank's rule), therefore the $\langle 111 \rangle$ dislocation should dissociate. However, by opposing the elastic repulsive forces which tend to separate the two superpartials, the APB energy controls the equilibrium spacing between them. This equilibrium distance is obtained by differentiation of the Nabarro equation [29]:

$$APB\,(energy) = \frac{\mu}{2\pi d} \left(\vec{b}_1 \cdot \vec{\zeta}\right) \left(\vec{b}_2 \cdot \vec{\zeta}\right) + \frac{\mu}{2d\pi\,(1-\nu)} \left(\vec{b}_1 \times \vec{\zeta}\right) \cdot \left(\vec{b}_2 \times \vec{\zeta}\right) \qquad (1.1)$$

where $\mu$ is the shear modulus, $\nu$ is the Poisson's ratio, $\vec{b}_1$ and $\vec{b}_2$ are the two Burgers vectors of the superpartials, $\vec{\zeta}$ is the direction of the dislocation line and d is the distance between the superpartials. The APB energy is equal to $\frac{\mu}{2\pi d}b_1 b_2$ for pure screw superpartials and $\frac{\mu}{2\pi(1-\nu)d}b_1 b_2$ for pure edge superpartials. This relationship is very useful to compute the APB energies from the separation distances observed using electron microscopes.

### 1.3.2  APB Energies in NiAl

Atomistic simulation of planar fault energies in the B2 crystals [30] and more recently in NiAl [31, 32] have shown that the only possible stable faults are the APBs on {110} and {112} planes. However, the existence of these stable planar faults have not been observed experimentally [33, 34]. The inability to identify the dissociation of superpartials bounded with an APB suggests that the APB energies are very high in NiAl. The minimum separation distance detectable in weak beam transmission electron microscopy [34] is limited by the resolution of the technique (1-1.5nm). This separation distance would correspond to APB energies of at least 500 and 750 mJ/m$^{-2}$ in the {110} and {112} planes respectively. However, no dissociation of the $\langle 111 \rangle$ dislocation was observed in this study. These results also correlate with an indirect experimental evaluation of APB energy recently given by Ardell as 500 mJ/m$^2$ [35].

The APB energy in NiAl was obtained from first principles calculation with values approaching nearly 900 mJ/m$^{-2}$ [36, 16, 37]. However, these studies are known to overestimate APB energies because of the fact that atomic relaxations are not taken into account. Although the absolute energy values of the {112} and {110} APBs obtained in first principles calculations are overestimated, the value of their ratio is still significant. The calculations of Sluiter et al. [36] give a ratio of APB energy in the {112} to {110} planes of 1.17, and those of Yoo and Fu [16] give a ratio of 1.22.

16

Molecular static calculations in NiAl using the interactomic potentials initially developed for $Ni_3Al$ by Voter [4] computed the values of the APBs as 340 mJ/m$^{-2}$ on {110} and 410 mJ/m$^{-2}$ on {112} [38]. The APBs were also calculated at 240 for {110} and 380 mJ/m$^2$ for {112} with the same potentials using molecular dynamics simulations [39]. Since the exact value of the APBs in NiAl are still unknown, the new potentials recently developed solely for NiAl were fitted to different arbitrary values of this fault. The potentials described by Rao [40] were fitted to the APB energy values of 425 mJ/m$^2$ on {110} and 499 mJ/m$^2$ on {112}. The potentials developed by Farkas [3] were fitted to the values 286 mJ/m$^2$ on {110} and 340 mJ/m$^2$ on {112}.

### 1.3.3 Dislocation Line Energies in NiAl

Using an anisotropic elasticity theory, the line energy for dislocations in stoichiometric NiAl at room temperature has been calculated [41] and the results are summarized in Figure 1.6 (from [41]). Dislocations with the ⟨100⟩ Burgers vector have the lowest energy and the edge orientation has slightly lower energy than the screw orientation. The ⟨100⟩ dislocations close to the screw orientation are expected to be unstable on the {110} and {100} planes [33].

According to Figure 1.6, the energy of the ⟨110⟩ dislocation on {110} planes is low enough not to expect dissociation of this dislocation into ⟨100⟩ dislocations. However, on {100} planes, the energy of the edge ⟨110⟩ dislocations is high enough to predict possible dissociation into ⟨100⟩ {100} dislocations with the appropriate dislocation line direction.

It is also clear that the screw orientation of the ⟨111⟩ dislocations is the most stable orientation at room temperature. Dislocations with ⟨111⟩ Burgers vectors of near edge orientation are unstable in the {110} plane and tends to dissociate into a combination of ⟨100⟩ and ⟨110⟩ dislocations. However, near edge ⟨111⟩ dislocations on {112} planes were observed in NiAl after deformation at room temperature [34] indicating that the edge ⟨111⟩ dislocation can be stabilized on {112} planes. At elevated temperature (>700K), all ⟨111⟩ dislocations dissociate into ⟨100⟩ + ⟨110⟩ dislocations or eventually into three ⟨100⟩

dislocations [42]. This observation indicates the importance of thermal activation energy and dislocation core energy in the dissociation process of the ⟨111⟩ dislocation [42].

### 1.3.4 Peierls-Nabarro Model of Dislocation Core Structure

In the Peierls-Nabarro model [29], an edge dislocation in a single cubic crystal is first created by superposition of two semi-infinite single crystals that approach each other with a displacement of a distance b/2 as represented on Figure 1.7. The displacements, $u_x$, antisymmetric about the plane y=0, are imposed on the two half crystals which are then linked to create the edge dislocation (see Figure 1.8). According to the Peierls-Nabarro model, the atomic displacements are such that the two crystals match perfectly without distortion when x tends towards infinity ($u_x(\infty) = - u_x (-\infty) = b/4$). Under the condition that the net stress along the plane y=0 vanishes, the function $u_x$ is defined by:

$$u_x = -\frac{b}{2\pi} \arctan\left(\frac{x}{\frac{\xi}{2}}\right) \tag{1.2}$$

where $\xi = d/(1 - \nu)$.

The width of the dislocation, defined as $\xi = d/(1 - \nu)$, corresponds to the region $-\frac{\xi}{2} < x < \frac{\xi}{2}$ where $u_x$ is smaller than b/8. The value $\xi$ defines the extent of the core of the dislocation that cannot be described by linear elasticity. The shape of the function $u_x$ is represented on Figure 1.9 for the values b=3 and two different values of $\xi$. The same procedure can be followed for the screw dislocation. The displacement function, $u_z$, obtained is similar to equation 1.2 with the difference that $\xi$ is replaced by $\eta$ where $\eta = (1 - \nu)\xi$. Therefore, the core width of the screw dislocation , $\eta$, is smaller than the one of the edge dislocation.

Following this dislocation model, some valuable expressions for the intrinsic resistance to the dislocation motion and critical stress to move the dislocation have been deduced. The specific free energy obtained for a displacement $\alpha b$ of the dislocation is given as:

$$W(\alpha) = \frac{\mu b^2}{4\pi(1 - \nu)} + \frac{\mu b^2}{2\pi(1 - \nu)} \exp\frac{\pi\xi}{b} \cos 4\pi\alpha \tag{1.3}$$

18
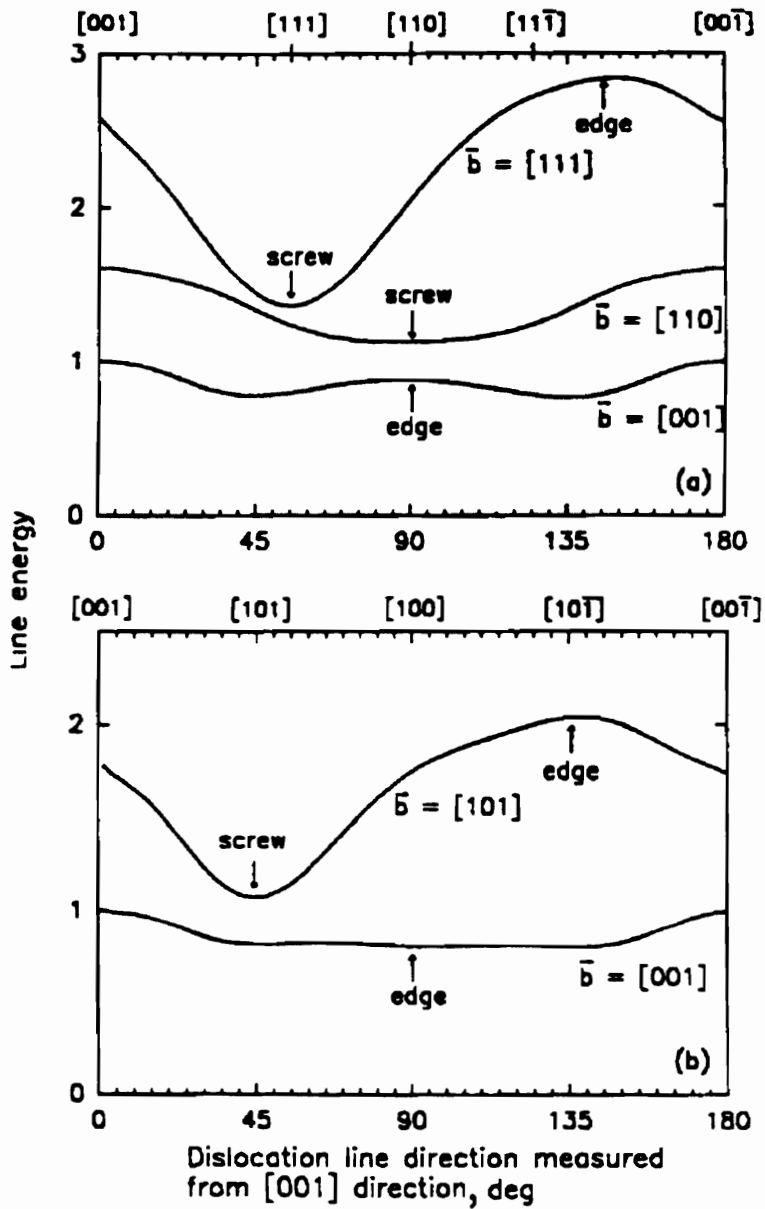
Figure 1.6: Dislocation line energies in NiAl at room temperature. (a) (110) plane, (b) (010) plane.
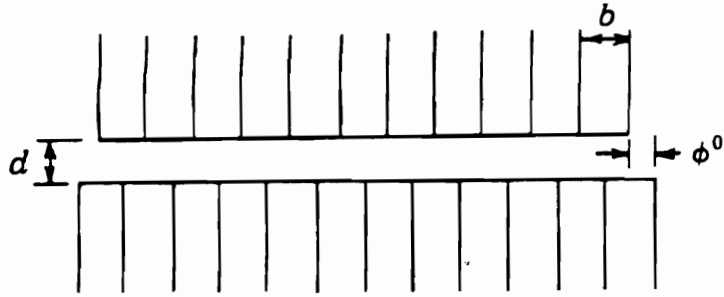
Figure 1.7: Two infinite single cubic crystals with diplacement b/2.
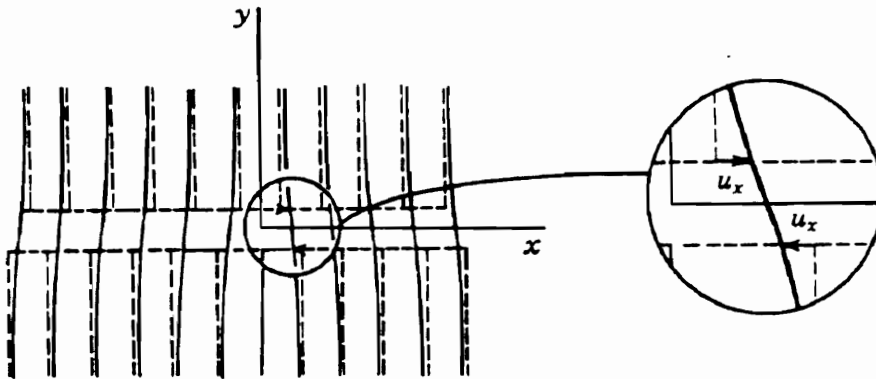


Figure 1.8: Displacement $u_x$ to create an edge dislocation along the plane Y=0.

$$W(\alpha) = \frac{\mu b^2}{4\pi(1 - \nu)} + \frac{W_p}{2} \cos 4\pi\alpha \qquad (1.4)$$

where $\mu$ is the shear modulus, $\nu$ is Poisson's ratio and $\xi$ the core width (see Figure 1.10). The maximum of this sinusoidal function ($W_p$) is called Peierls energy. The stress required to surmount this potential barrier is called the Peierls stress $\sigma_p$ given by:

$$\sigma_p = \frac{1}{b^2}\left[\frac{\delta W(\alpha)}{\delta \alpha}\right]_{max} = \frac{2\pi W_p}{b^2} = \frac{2\mu}{1 - \nu} \exp -\frac{2\pi\xi}{b} \qquad (1.5)$$

A plot of the function $\sigma(\alpha)$ is represented on Figure 1.11. According to this model, the dislocation mobility follows an exponential decrease when the core width decreases. However, this model has some limitations. First, it does not include thermal activation that would help the dislocation to surmount the Peierls barrier at temperatures higher than 0K. Second, the core of the dislocation is assumed to be planar, spreading only along one slip plane. These important assumptions limit the validity of the model in the comparison with dislocation properties in a real crystal. Nevertheless, it is the only analytical model that predicts dislocation properties based on the structure of the dislocation core and is therefore very useful to understand the results from atomistic simulation of dislocations.

### 1.3.5 Atomistic Simulation of Dislocation Cores in B.C.C. Metals

Atomistic simulation is based on the description of interatomic forces that control the crystal structure properties. In the study of metals and intermetallics, most calculations have been performed at 0K with the static lattice approach using the conjugate-gradient method. An atom array is created where forces between one atom and its close neighbors are described by a potential function. The computational procedures involve the minimization of energy of the array containing the defect. This technique was found to be the most efficient in computing the energy and structure of crystal defects and will be more precisely described in the simulation technique chapter.

Early computations were conducted to simulate dislocations in the b.c.c. crystal structure for pure metals [43]. Results of atomistic simulation brought to the conclusion that
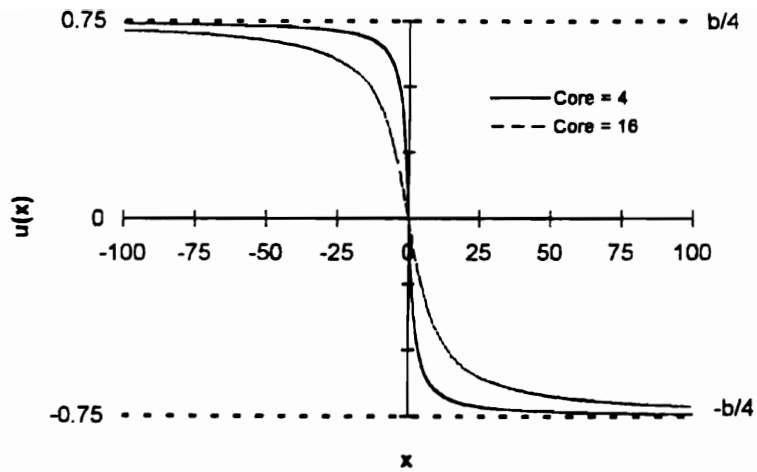
Figure 1.9: Function $u_x$ describing the core structure of an edge dislocation in Peierls-Nabarro model for b=3. The two plots were obtained for core width ($\xi$) equal to 4 and 16.
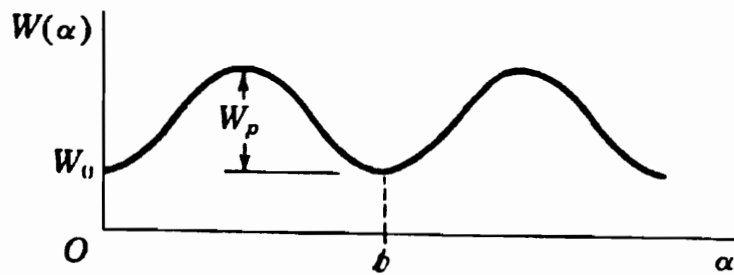


Figure 1.10: Specific free energy of the dislocation, W, as a function of its displacement, $\alpha$.

the low mobility of the $1/2\langle111\rangle$ screw dislocation in this crystal structure is attributed to the non planarity of the dislocation core structure. In comparison with the Peierls-Nabarro model, relaxation of the lattice around the simulated dislocation can occur in any favorable planes containing the dislocation line. It can be seen in Figure 1.12 [44], that the core of the $1/2\langle111\rangle$ screw dislocation in b.c.c. crystal spreads along three $\{110\}$ intersecting planes. Therefore, complex core transformations are necessary before the $1/2\langle111\rangle$ screw dislocation can begin to move, creating a strong resistance to the dislocation motion. More important, it is the consistency of the results obtained with different potentials and their agreement with experimental observations that explains the success of atomistic simulation in the b.c.c. crystal structure [45].

### 1.3.6 Dislocation Core Structures in NiAl

The first simulations of dislocation core structure in NiAl were based on interatomic forces developed for $Ni_3Al$ [46, 47]. Using the embedded atom method, these calculations indicated that $\langle100\rangle$, $\langle110\rangle$ and $\langle111\rangle$ dislocations have more complex core structures than similar dislocations in b.c.c. metals. It was also determined that the lowest energy configuration for a $\langle111\rangle$ dislocation was as an undissociated dislocation.

In the past five years, a strong effort has been devoted to develop new potentials specific to NiAl that would match more accurately the elastic constant of this intermetallic. As a result, two new sets of embedded atom potentials have been derived by Rao [40] and Farkas [3]. The results of their application to simulate dislocation core structures using molecular statics have been published recently. These results are summarized in Table 1.2.

In agreement with experimental observations, the simulated $\langle100\rangle$ and $\langle110\rangle$ dislocations do not dissociate. Separation distances between the $1/2\langle111\rangle$ superpartials are small enough to be invisible in TEM observations. In general, the core structures of the dislocations simulated are complex. The planar core structures also have some minor extension in other planes indicating that these dislocations do not follow precisely the Peierls-Nabarro model. However, it is clear that the planar configurations of the $\langle100\rangle$ and $\langle111\rangle$ dislocations present
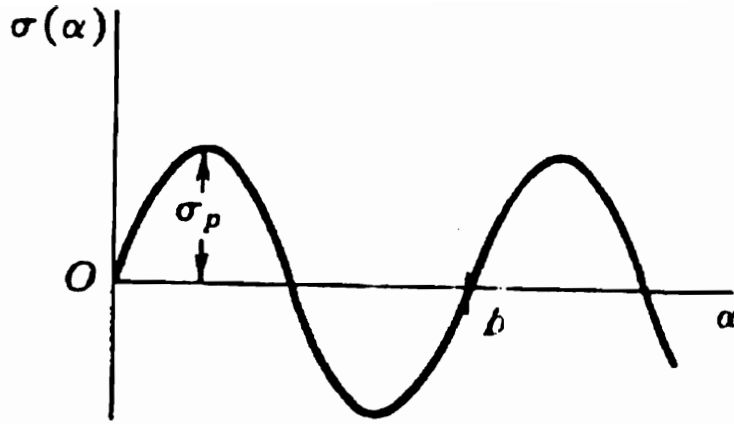
Figure 1.11: Stress required to move a Peierls-Nabarro dislocation as a function of its displacement, $\alpha$, in the lattice.

Table 1.2: Dislocation core structures and critical stress values simulated in NiAl.

| Slip System | Dislocation Type | Ref. | Core Structure | Critical Stress (MPa) | Stable Dissociation |
|---|---|---|---|---|---|
| $\langle 100 \rangle \{110\}$ | screw | [31] | planar $\{110\}$ | 220 | no |
| | | [48] | planar $\{110\}$ | 70 | no |
| | mixed 45° | [31] | non planar | 1290 | no |
| | | [48] | non planar | 1650 | no |
| | edge | [31] | planar $\{110\}$ | 320 | no |
| | | [48] | planar$\{110\}$ | 401 | no |
| $\langle 100 \rangle \{100\}$ | screw | [31] | planar $\{110\}$ | cross slip | no |
| | | [48] | planar$\{110\}$ | cross slip | no |
| | edge | [31] | non planar | 2590 | no |
| | | [48] | non planar | 2680 | no |
| $\langle 111 \rangle \{110\}$ | screw | [31] | non planar | 450 | 1.1nm |
| | edge | [31] | planar$\{110\}$ | 380 | 1.3nm |
| $\langle 111 \rangle \{112\}$ | screw | [31] | non planar | 740 | 0.9nm |
| | edge | [31] | non planar | 590 | .1nm |
| $\langle 110 \rangle \{110\}$ | screw | [31] | non planar | cross slip | no |
| | edge | [31] | non planar | cross slip | no |
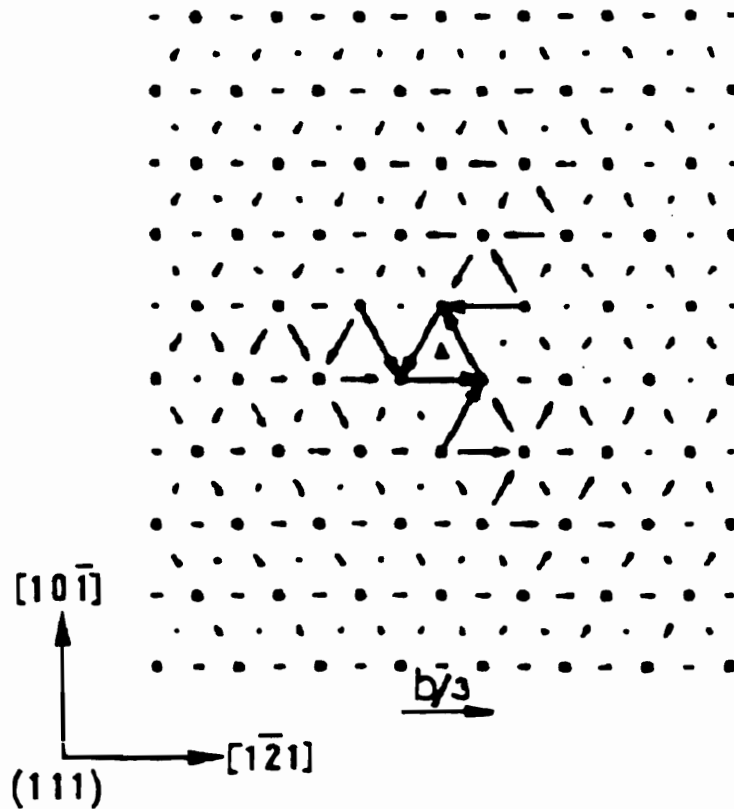
Figure 1.12: Core structure of the 1/2⟨111⟩ screw dislocation in b.c.c. metals. The arrows in between two atoms represent the relative displacement with respect to each other.

the lowest values of critical stresses to move the dislocations.

The results obtained with these two sets of potentials are in good agreement with experimental results since the $\langle 100 \rangle$ dislocations are the easiest to move, followed by $\langle 111 \rangle$ and $\langle 110 \rangle$. The most favorable slip planes also appear to be the $\{110\}$ planes. According to these simulations, the pure edge and pure screw orientations of the $\langle 100 \rangle$ Burgers vector correspond to the more mobile dislocations. However, these line orientations are unstable and the stable mixed orientation has a high critical stress value. This consideration has not been discussed and might be important to understand the behavior of the $\langle 100 \rangle$ slip. It is also important to mention that the technique used in these studies does not include the effects of non-glide stresses, kinks or thermal activation on the dislocation mobility. For example, cross-slip of the $\langle 100 \rangle$ dislocations and their motion along the $\{100\}$ planes were not observed in the simulations. It is suggested that thermal activation is important for these to occur.

# Chapter 2

# TECHNIQUE OF SIMULATION

## 2.1 ATOMISTIC SIMULATION METHOD

The simplest model of a metallic material at the atomic scale can be visualized as an array of atoms interconnected with springs. More sophisticated atomistic simulation techniques have now been developed to describe more accurately the atomic interactions in crystalline materials. The atomistic simulations presented in this study were conducted with molecular statics calculations using embedded atom potentials.

### 2.1.1 Molecular Statics Calculations

Molecular statics calculations rely on the high speed computation capabilities of modern computers. In this technique, the total energy of a crystal is obtained as the sum of the energies of each individual atoms. The energy of each atom is described by a potential function that only depends on the distance of this atom from its close neighbors. Starting from a perfectly stable crystal structure, introduction of a defect induces forces on the atoms. Through a relaxation process, these atoms are allowed to move in order to drive the system to a new equilibrium configuration corresponding to a minimum in the energy of the defect lattice. The major limitation of this technique is the absence of atomic vibration due to thermal activation. It is then considered that the results obtained characterize the material at 0K.

The computer code used in this study is based on the original DEVIL code developed by Norgett, Perin and Savino [49]. The relaxation of the lattice is an iterative process of energy minimization where the total energy is computed at each step as a function of the

$3\times N$ coordination of the N atoms. In order to find the minimum energy configuration, the atom displacements are governed by a conjugate gradient method that follows the steepest descent of the gradient of energy function. Nevertheless, in their step by step displacements, atoms are constrained to move in direction perpendicular to their previous move. The process can be stopped when the forces on each atom are below a small specified value or after a certain number of iterations. This method is known as the fast convergent technique.

## 2.1.2    Embedded Atom Method

The embedded atom method (EAM) computes the energy of an atom as the sum of its interactions with the surrounding atoms[50]. These interactions are described by two kinds of potential functions. While a classical pairwise potential V (Morse function) describes the attractive and repulsive electrostatic interactions between two atoms, an embedding function F takes into account the local electronic density that atoms experience due to the presence of their surrounding neighbors. The introduction of the embedding function is for accuracy when there is a density fluctuation in the materials. This becomes very important in the simulation of defects such as vacancy clusters and free surfaces.

The total energy of the system is written as:

$$E = \frac{1}{2} \sum_{i,j} V(r_{ij}) + \sum_i F(\overline{\rho}_i) \tag{2.1}$$

with

$$\overline{\rho}_i = \sum_{i,j} \rho(r_{ij}) \tag{2.2}$$

where V is the pair potential, F is the embedding function, $\rho$ is the electronic density function, $\overline{\rho}_i$ is the density at atom i due to all its neighbors and $r_{ij}$ is the interatomic distance between atom i and j considered. To reduce computer time without loosing the accuracy of the technique, atomic interactions are usually designed to drop to zero after the second closest neighbor distance. This constitutes the cut-off radius.

28

To describe a binary alloy AB, seven functions are required which are: $V_{A-A}$, $V_{A-B}$, $V_{B-B}$, $F_A$, $F_B$, $\rho_A$ and $\rho_B$. Pure metal functions for metal A ($V_{A-A}$, $F_A$, $\rho_A$) and metal B ($F_B$, $V_{B-B}$, $\rho_B$) are developed to fit the properties of each of the pure metals. $V_{A-B}$ is the only function fitted to the properties of the binary alloy. It is important to mention that all embedded functions F used in this study have been developed by requiring that the energy of the crystal obeys a simple universal function, Roses equation of state [51], which scales the cohesive energy of most metals. As a result of this method of determination, the potentials always gives a perfect agreement to the experimental values of cohesive energy, lattice parameter and Bulk modulus for any choice of the other functions.

### 2.1.3   Cauchy Pressure and Limitation of the EAM Technique

Description of interatomic forces in the EAM technique are limited by the lack of angular considerations in the electronic density function. EAM is therefore an inappropriate method to simulate covalent materials such as Si or Ge. More elaborate methods, based on EAM, have been proposed to simulate these materials. They include some dependence of the local electron density on the angle between the vectors joining two neighbor atoms to a central one [52]. As explained below, development of EAM potentials in b.c.c transition metals also revealed that this technique fails to describe systems in which the Cauchy pressure is negative.

Due to the symmetry of the lattice, a cubic crystal structure has only three independent elastic constants, $c_{11}$, $c_{12}$ and $c_{44}$. The Cauchy pressure is then defined as P=1/2 ($c_{12}$-$c_{44}$) in this crystal structure. For example Cr is one of these transition metals with negative Cauchy pressure and is characterized by a $c_{44}$ larger than $c_{12}$. Studies of such metals revealed the impossibility to fit properly the elastic constants using EAM. However, this problem has been solved [38] by including an angular dependent term to the EAM technique. These modifications are briefly described in the following section.

## 2.1.4 Embedded Defect Method for Non Central Interactions

Among the techniques proposed to include angular bonding in static computations [38], the embedded defect method (EDM) seemed to be the simplest approach. This method allows to fit the best possible EAM potentials and add in a second step the non-central interactions.

The embedded defect method (EDM) was introduced by Pasianot *et al.* [38] as an extension of the embedded atom method (EAM) for the purpose of treating covalent bonding in transition metals. Examples were given for its use for b.c.c. metals [38]. The same approach has also been followed to develop potentials for the TiAl system [53].

The main idea is to describe the local electronic density as a tensor in analogy to the dipole tensor introduced by a defect.

$$\rho_i^{\alpha\beta} = \sum_j \phi(r_{ij}) r_{ij}^\alpha r_{ij}^\beta / r_{ij}^2 \tag{2.3}$$

where the superscripts $\alpha$, $\beta$ refer to the components of the vector $r_{ij}$ that joins atom i with atom j. The trace of this tensor corresponds to the electronic density $\rho_i$ as used in EAM. A second invariant is defined as the norm of the deviatoric tensor (null trace).

$$Y_i = \sum_{\alpha\beta} \rho_i^{\alpha\beta^2} - 1/3\rho_i \tag{2.4}$$

This second invariant ($Y_i$) is angular-dependent.

Two functions F and G of these two invariants define the many-body terms of the potentials. The first one corresponds to the embedding function and the second is the additional non-central interaction term.

$$E = \frac{1}{2} \sum_{ij} V(r_{ij}) + \sum_i F(\rho_i) + \sum_i G(Y_i) \tag{2.5}$$

As done by Pasianot *et al.* and in previous work for TiAl [53], G is defined as a linear function through the origin. The slope of this function (G') is the only parameter to be

used in the fitting procedure in addition to the EAM parameters. The potentials obtained through this method are first order empirical expansions of the EAM. The G term is non zero for structures involving shear and is particularly appropriate to fit shear elastic properties.

## 2.2 INTERATOMIC POTENTIALS

### 2.2.1 EAM Potentials for NiAl

There are several interatomic potentials developed for Ni-Al. The potentials developed by Voter et al. [4] and those developed at Sandia Labs [54] are based on the $L1_2$ $Ni_3Al$ phase. Interatomic potentials are normally developed on the basis of one intermetallic phase in the system and this does not ensure a reasonable fit of the properties of other phases in the system. The potentials of Voter et al. [4], for example do not predict the B2 phase as the stable structure at the equiatomic composition. This was first pointed out by Clapp [39]. The $L1_0$ phase is predicted as having slightly lower energy. The elastic constants that these potentials predict for the B2 phase are 40% higher than experimental values. Nevertheless, these potentials have been used extensively in simulations in both $NiAl$ and $Ni_3Al$.

The EAM potentials used in this study have been developed by Farkas [3] to give an accurate description of the properties of $B2$ $NiAl$ and $Ni_5Al_3$ as well as 3R martensite. It describes appropriately the forces in the system for the central region of the phase diagram. In this new set of potentials, atomic interactions of pure metal type (Al-Al and Ni-Ni) are described by the interatomic potentials for Al and Ni originally developed by Voter et al. [4] for f.c.c. metals. These potentials have successfully described the Al-Al interactions in several studies of the Ni-Al and Ti-Al systems [31, 53, 3]. However, these functions have been modified in this study so that the first derivative of the embedded function ($F'$) is equal to zero for the electronic density of the perfect lattice ($\rho_0$). In this case, the potentials are said to be in their effective pair scheme. The transformation used to convert to the effective pair scheme is as follows:

$$F^{eff}(\rho) = F(\rho) - \rho F'(\rho_0) \tag{2.6}$$

$$V^{eff}(r) = V(r) + 2\rho(r)F'(\rho_0) \tag{2.7}$$

where $F$ is the embedded function, $V$ is the Morse potential function, $\rho$ is the electronic density function, $\rho_0$ is the electronic density in the perfect lattice of the pure metals and $r$ is the interatomic distance. The electron density was not normalized to the same value of $\rho_0$ for both Ni and Al in perfect lattice conditions. The values for the electron density of the perfect lattice of Ni and Al were kept to be 0.34 and 0.38, respectively, as given by Voter et al. [4]

The mixed pair interaction potential ($V_{Ni:Al}^{eff}$) was obtained by empirically fitting a combination of the pure metals effective pair interactions $V_{Ni}^{eff}$ and $V_{Al}^{eff}$. The general form is as follows:

$$V_{Ni:Al}^{eff}(a+bx) = [AxV_{Al}^{eff}(c+dx) + B(1-x)V_{Ni}^{eff}(e+fx)] \tag{2.8}$$

where $x$ takes values from zero to unity. The parameters a, b, c, d,e, f, A and B were obtained to give the best overall fit to the properties of the phases considered.

The parameters in Equation 2.8 were varied and their effects on the properties of interest were studied to determine the more suitable values to fit the entire system. The data considered consists of the set used by Voter et al. [4] for $Ni_3Al$, the set used by Rao et al. for $NiAl$ [40] and the data on 3R martensite $L1_0$ $NiAl$ and $Ni_5Al_3$ given by Khadkikar et al. [55].

Best fit values obtained for the parameters are given in Table 2.1. The effective pair function for the mixed interaction is shown in Figure 2.1, together with the effective pair functions for Al and Ni. Figure 2.2 shows the electronic densities and Figure 2.3 the embedded functions used.

These potentials predict that the B2 phase is more stable than the $L1_0$ phase, with an energy difference of 0.03 eV. Cohesive energy and elastic constants are fitted almost

Table 2.1: Parameters obtained for the mixed Ni-Al potential (from [3]). Energies are given in eV, and distances in $10^{-1}nm$.

| a | b | c | d | e | f | A | B |
|------|------|-----|-------|-----|--------|------|------|
| 0.62 | 4.96 | 1.0 | 4.555 | 1.0 | 3.7895 | 1.62 | 1.08 |
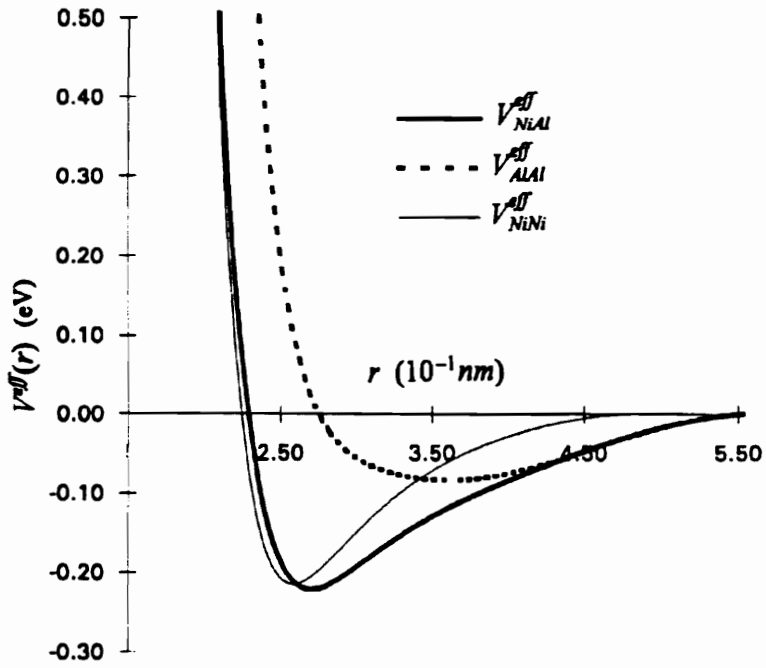


Figure 2.1: Pair potential functions in NiAl.
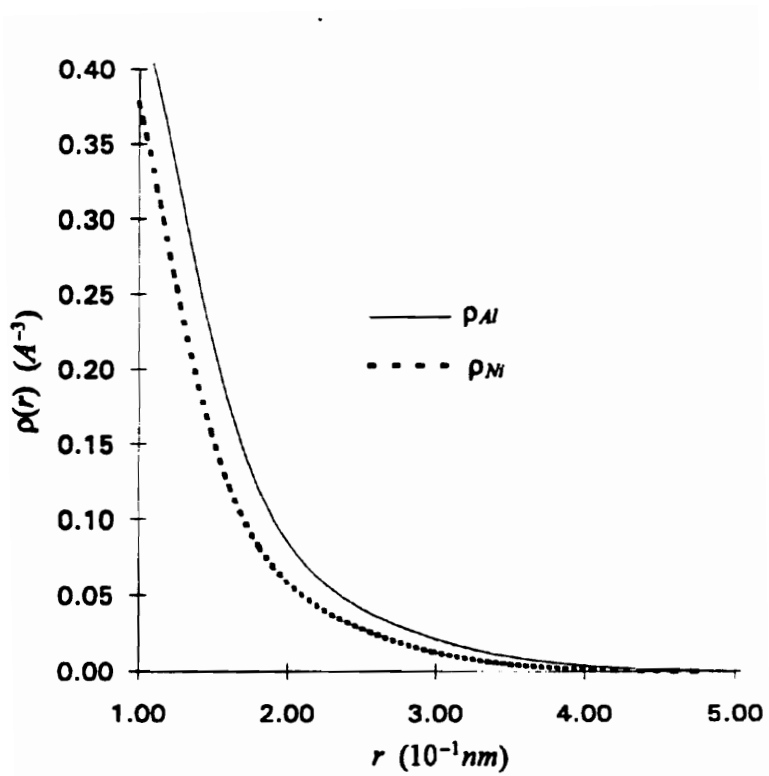
Figure 2.2: Electronic density functions for Ni and Al.
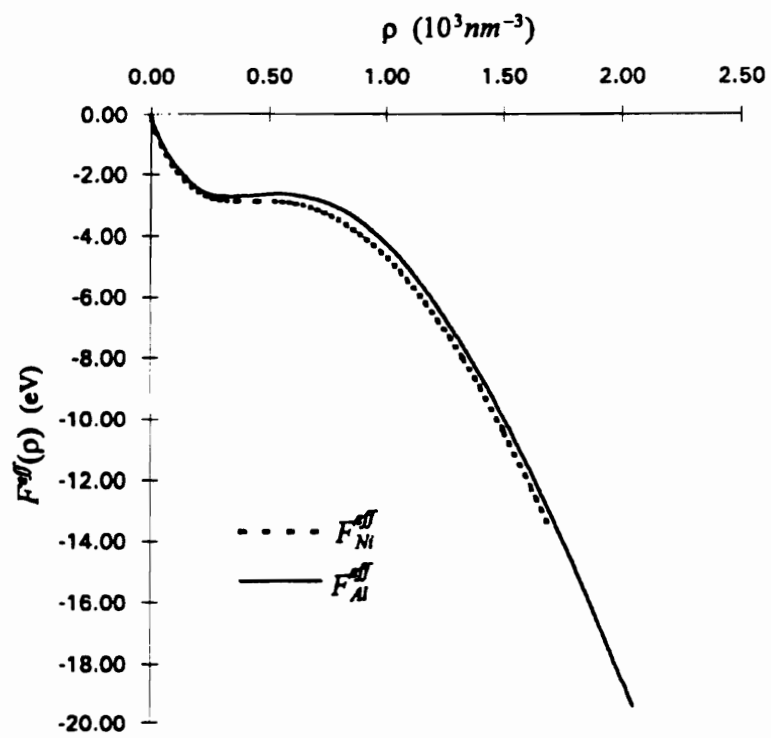
Figure 2.3: Embedded functions for Ni and Al.

perfectly to the experimental values. Table 2.2 shows the values predicted for the various properties of this phase, together with those predicted by the potentials of Voter et al. [4] and Rao et al [40].

As mentioned in section 1.3.2 the APB energies in this intermetallic are not known. They cannot be directly measured due to the fact that $\langle 111 \rangle$ dislocations experimentally observed in this system do not dissociate into superpartials bounding an APB. However, the ratio of the APB energies in the $\{112\}$ and $\{110\}$ planes has been predicted to average 1.19 through first principles calculations. The ratio of the APB values for the interatomic potentials used in this study is equal to 1.19 which is also very close to the value obtained with the potentials from Voter et al. (1.20) and the ones from Rao et al. (1.17). It is important to bear in mind the uncertainty in these APB values, since they cannot be experimentally measured.

## 2.2.2 EAM Potentials for FeAl

At the difference of NiAl, no atomistic simulations have been conducted in FeAl. The main reason for the absence of atomistic computation in this system was the lack of embedded atom potentials for the Fe-Al interactions. However, this potential has been recently developed by Farkas [56].

As for NiAl, the functions $V_{Al}$, $F_{Al}$ and $\phi_{Al}$ for the aluminum interactions, developed by Voter *et al* [4] and transformed to their effective pair scheme, were used . For the Fe-Fe interactions, three different potentials have been reported by Simonelli [57], Harrison [58] and Jhonson [59]. The functions $V_{Fe}$, $F_{Fe}$ and $\phi_{Fe}$ used in this study were taken from the embedded atom potentials developed for b.c.c. iron by Simonelli *et al* [57]. These potentials were originally constructed in effective pair scheme and a comparative study in b.c.c. iron have shown that results obtained with these potentials give intermediate values when compared with Harrison and Johnson potentials [60]. The electron density for Fe and Al in the perfect lattice condition were also normalized to the same value (0.34) which was the one used by Voter in the Al potentials.

The interatomic pair potential for Fe-Al ($V_{Fe-Al}$) was developed in order to get the best fit to lattice and thermodynamic properties of B2 FeAl. The function used in the fitting process was a cubic spline which general form was similar to the pairwise potential in Fe [57]:

$$V(r) = \sum_{i=1}^{3} a_i (r - r_i)^3 H(r_i - r) \tag{2.9}$$

where V(r) is in eV, distances are in Å and H is the Heavyside function that takes the value of unity for a positive argument and zero for a negative one. The pair potentials for Al-Al, Fe-Fe and Al-Fe are presented in Figure 2.4. The parameters obtained for equation 2.9 in the fitting procedure are indicated in Table 2.3.

The material properties obtained for FeAl and Fe$_3$Al are listed in Table 2.4 together with experimental and first principles data. The lattice parameter and cohesive energy of the B2 phase were required to agree perfectly with experimental results. The B2 phase has a lower energy than the $L1_0$ phase with an energy difference calculated as 0.05 eV.

The elastic constants were the best fit possible considering the limitation of the Embedded Atom Method to the condition $c_{12} > c_{44}$. The same problem was encountered in the development of potentials in tetragonal $L1_0$ TiAl [53] for which the Cauchy pressure ($c_{13}$-$c_{44}$) is negative. The use of the embedded defect technique in the simulation of TiAl introduced angular terms for a better fit of the elastic constants than the embedded atom method. The comparison of these two methods in TiAl revealed a 5% increase in defect energies due to the non central interactions. The approach in the case of FeAl was different. Since the experimental values of $c_{12}$ and $c_{44}$ are very close, general central interactions are expected to give a good general description of elastic properties.

The values for the {110} and {112} APBs are indicated in Table 2.4 for stoichiometric FeAl. These potentials also predict a decrease in APB energy for off stoichiometry alloys on the Fe rich side. The results indicate the APB energy is 50 % smaller in Fe-43.7Al. Such a tendency can be expected since the APB fault disappears in pure b.c.c. iron.

Table 2.2: Parameters for $B2$ $NiAl$ given by the potentials. Cohesive energies are given in eV/atom, distances in $10^{-1}nm$ and fault energies in $mJ/m^2$.

| Property | Experimental | Calculated | Calculated [4] | Calculated [40] |
|---|---|---|---|---|
| a(0.1nm) | 2.88 | 2.88 | 2.87 | 2.88 |
| $E_{coh}$(eV) | 4.50 | 4.49 | 4.38 | 4.43 |
| $C_{11}(eV/A^2)$ | 1.24 | 1.16 | 1.74 | 1.18 |
| $C_{12}(eV/A^2)$ | 0.85 | 0.77 | 1.15 | 0.79 |
| $C_{44}(eV/A^2)$ | 0.72 | 0.77 | 1.11 | 0.80 |
| APB(110) | *** | 286 | 340 | 425 |
| APB(112) | *** | 340 | 410 | 499 |
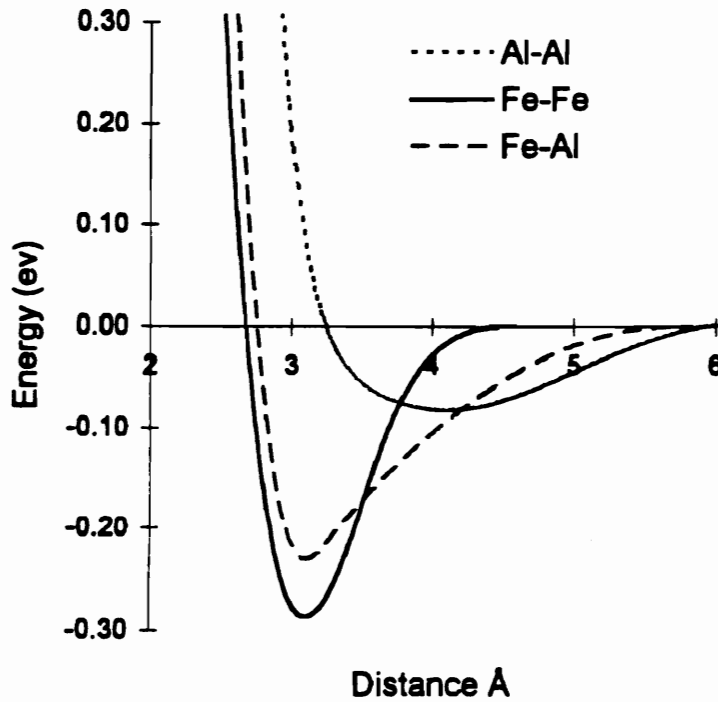


Figure 2.4: Pair potential functions in FeAl.

Table 2.3: Parameters obtained for the mixed Fe-Al potential

| $r_i$ | $r_1 = 2.786$ | $r_2 = 3.595$ | $r_3 = 4.997$ | $r_4 = 5.355$ |
|---|---|---|---|---|
| $a_i$ | $a_1 = -2.1931$ | $a_2 = 0.01776$ | $a_3 = -0.04084$ | $a_4 = 0.03743$ |

### 2.2.3 EAM and EDM Potentials for CoAl

B2 CoAl has a negative Cauchy pressure and an accurate description of the interatomic forces requires the embedded defect technique. In order to describe the Co-Co and Al-Al interactions in the CoAl system, interatomic potentials were taken from previous studies of pure metals. The interatomic potentials chosen for Al were again the ones developed by Voter *et al.* [4] transformed to their effective pair forms. Potentials for hexagonal cobalt have been derived by several authors [62, 63, 64]. These studies have shown that standard EAM can adequately describe the properties of this hexagonal lattice. Among these potentials, the ones developed by Pasianot and Savino [64] were chosen for this study since they take advantage of the inner relaxation of the hexagonal crystal. These Co-Co potentials derived by Pasianot and Savino were already developed in their effective pair scheme. The electron density was normalized to the same value for both Co and Al in the perfect lattice conditions. This approach was found to be adequate for the Ti-Al case [3].

The general form of the mixed pair interaction potential was developed by Farkas [65] as a linear combination of the effective pair interactions of Co and Al:

$$V_{CoAl}^{eff}(a + bx) = A[x V_{Al}^{eff}(c + dx) + (1 - x)V_{Co}^{eff}(e + fx)] \qquad (2.10)$$

where $x$ takes values from zero to unity.

The standard embedded atom potentials were developed first by fitting the functions to available data subject to the condition of positive Cauchy pressure. This procedure was followed in order to have the best EAM potential possible for this system for use in simulation codes without the angular term. When the EAM potentials were complete, the angular term was added to the EAM formalism as in Equation 2.5 in order to improve the fitting of the elastic constants.

The parameters obtained are given in Table 2.5. The effective pair function for the mixed interaction ($V_{CoAl}$) is shown in Figure 2.5, together with the effective pair functions for Al ($V_{Al}$) and Co ($V_{Co}$). Table 2.5 also shows the best fit values obtained for the slope

of the angular function G.

The B2 phase was obtained as stable with an energy difference of 0.15 eV from the cubic $L1_0$ CoAl phase. The parameters predicted by the potentials for the B2 phase are summarized in Table 2.6.

The values for lattice parameters are from Pearson's handbook [61]. The cohesive energies are taken from Hultgren et al. [66], the experimental elastic constants were measured by Bafuk [67] and the elastic constants computed from first principles calculations are from Mehl et al. [68].

These results clearly show that the addition of the angular term can not affect either cohesive energies or lattice parameters given by the EAM potentials. As expected, angular dependent forces have a significant effect on the energies of planar faults. The APB energies increase by approximately 30% due to non-central forces. The energy increase is actually larger than the calculated contribution of the non-central forces. For example, for the {110} APB, the calculated contribution of non-central interactions was 74 $mJ/m^2$, whereas the difference in the APB energies calculated with and without angular term was much larger. This is explained by a different relaxed structure of the APB in each cases. The APB simulated with the EAM potentials has a larger volume expansion (0.01 nm) and implies a larger local tetragonality as compared to the EDM potentials.

The effects of angular dependent forces on APB energies in CoAl as calculated with the present potential are larger than those observed in previous work in Ti-Al (5%) [69]. The observed difference in magnitude of energy is simply related to the fact that the value of G' that was used in the present work to fit the elastic constants properly is larger than that used in the Ti-Al case by a factor of 6. This correlates with the larger negative Cauchy pressure in CoAl.

Table 2.4: Parameters for *B2 FeAl* given by the potentials. $\mu$ calculated using the Voigt average.

| Phase | Property | Exp. [61] | First P. [16] | EAM |
|-------|----------|-----------|---------------|-----|
| FeAl B2 | a (0.1nm) | 2.91 | 2.83 | 2.91 |
| | $E_{coh}$ (eV) | 4.16 | — | 4.16 |
| | $c_{11}(eV/A^3)$ | 1.3 | 1.8 | 1.2 |
| | $c_{12}(eV/A^3)$ | 0.76 | 0.8 | 0.75 |
| | $c_{44}(eV/A^3)$ | 0.79 | 1.029 | 0.73 |
| | $\mu$ (GPa) | 93.2 | 131 | 84.5 |
| | (110)APB (mJ/m$^2$) | — | — | 115 |
| | (112)APB (mJ/m$^2$) | — | — | 190 |
| $L1_0$ bcc | $E_{coh}$ (eV) | — | — | 4.11 |
| $L1_2$ fcc | $E_{coh}$ (eV) | — | — | 4.33 |
| $DO_3$ B2 | $E_{coh}$ (eV) | — | — | 4.3 |
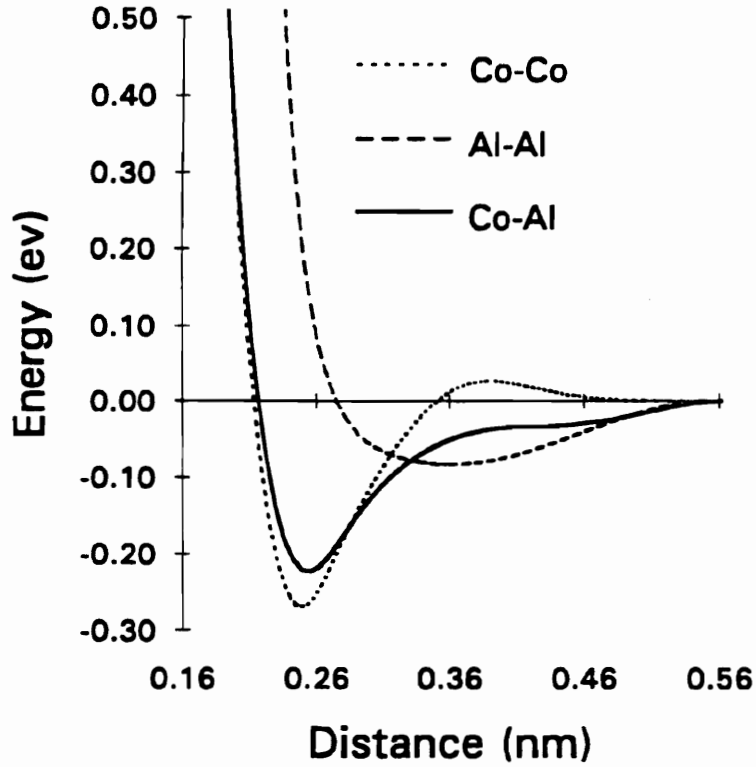


Figure 2.5: Pair potential functions in CoAl.

Table 2.5: Parameters obtained for the mixed Co-Al potential. Energies are in eV, distances in 0.1 nm

| a | b | c | d | e | f | A | G' |
|---|---|---|---|---|---|---|---|
| 1.690 | 4.0 | 1.910996 | 3.643984 | 1.75373 | 3.509799 | 1.0909091 | 100 |

Table 2.6: Parameters for $B2$ $CoAl$ given by the potentials. $\mu$ was computed using Voigt average.

| Property | Experimental | First Principle | EAM | EDM |
|---|---|---|---|---|
| a (0.1nm) | 2.86 | — | 2.86 | 2.86 |
| $E_{coh}$ (eV/atom) | 4.45 | — | 4.47 | 4.47 |
| $c_{11}$ $(eV/A^2)$ | 1.68 | 1.6 | 1.41 | 1.44 |
| $c_{12}$ $(eV/A^2)$ | 0.67 | 0.67 | 0.91 | 0.89 |
| $c_{44}$ $(eV/A^2)$ | 0.87 | 0.81 | 0.72 | 0.99 |
| APB(110) $(mJ/m^2)$ | — | — | 715 | 912 |
| APB(112) $(mJ/m^2)$ | — | — | 793 | 1062 |
| $\mu$ (GPa) | 116 | 107 | 85 | 113 |

# Chapter 3

# PLANAR FAULTS IN B2 ALUMINIDES

## 3.1 TECHNIQUE OF SIMULATIONS

### 3.1.1 Simulation of a Planar Defect

The purpose of these simulations was to compute the energy of a planar fault along a defined crystallographic plane with respect to the perfect lattice energy. The first step was then to generate the perfect crystal structure. This was accomplished in the program by defining the cubic bravais lattice with three orthogonal vectors (edges of the cube) which lengths were equal to the lattice parameter of the cubic cell. The two atoms contained in the unit cell of the B2 structure were then introduced in the lattice with respect to this coordinate system. The coordinates of sublattice 1 and 2 were respectively (0,0,0) and (1/2,1/2,1/2). The translation of the basis according to the bravais lattice generated all atom coordinates of the perfect crystal. A second orthogonal coordinate system was then defined (X,Y,Z) using Miller indices of crystallographic direction, to rotate the crystal in the orientation of interest.

The planar faults were simulated along the lines originally proposed by Vitek [70]. The method essentially computes an unstable stacking fault energy along a plane of cut (h,k,l) (see Figure 3.1). The two blocks of atoms defined on both sides of this plane were rigidly displaced according to a planar fault vector which components were in the X and Z directions. The new energy $E_1$ was computed after relaxation only in the Y direction of this new configuration. The planar fault energy, $\gamma$, was then defined as:

$$\gamma = \frac{(E_1 - E_0)}{S} \tag{3.1}$$

where S was the surface of the plane of cut and $E_0$ was the energy of the perfect crystal.

Because of the computing time limitation, the size of the block of atom had to be limited. To keep the accuracy of the results, the external limits of this block were set to recreate the behavior of the bulk material when any defect was introduced in the simulation. In these external layers, also called boundaries, atoms were not free to relax according to the minimum energy position. The boundary condition in the Y direction was defined by an external layer of atoms that were fixed in the perfect crystal positions and did not move during the relaxation process. The size of the simulated block in the Y direction was chosen to obtained the smallest simulation for which these fixed atoms did not influence the relaxation of the free atoms. Periodic boundary conditions were used in the X and Z directions since the periodicity of the atoms in these directions was not disrupted by the translation perpendicular to Y.

### 3.1.2   Representation of the Results

The $\gamma$-energies were computed for different fault vectors within the chosen plane. Since the fault vector was a linear combination of X and Z, the $\gamma$- energy was a three dimensional function $\gamma$=f(X,Z) represented as a $\gamma$-surface [70]. This method of representation was a very good visual method to determine the local minima or the directions of low energy.

The shape of the $\gamma$-surface was obtained with the computation of a minimum 100 planar fault energies corresponding to 100 fault vectors in order to scan the entire studied plane. The function $\gamma$=f(X,Z) was plotted with the software SURFER to optimize the data points and create a three dimensional surface. The graphs presented in this study are contour level plots of these surfaces. This was found to be the more efficient representation to visualize these three dimensional functions on a piece of paper. These plots can be seen as a map of the energy to overcome to shear the crystal along this plane.

The $\gamma$-surfaces computed in NiAl, FeAl, and CoAl were along the {110} and {112}planes since these planes contain the anti phase boundaries and the ⟨111⟩ direction which is the close packed direction in the B2 structure.

## 3.2 RESULTS OF PLANAR FAULT SIMULATIONS

### 3.2.1 EAM Simulations in FeAl, NiAl and CoAl

The {110} and {112} $\gamma$-surfaces were computed in FeAl, NiAl and CoAl using embedded atom method. For the case of CoAl, a good description of the interatomic forces required consideration of the angular forces. For comparison, the next section will present the result obtained in CoAl using embedded defect method that includes angular terms. The goal of these computations was to identify the possible stable planar fault as well as the maximum shear fault energies ($\gamma_{us}$ called unstable stacking fault) along specific shear directions.

For computation of the {110} $\gamma$-surface, the crystal was oriented such that X=[001], Y=[110] and Z=[$\bar{1}$10]. The stacking of the {110} planes for the B2 structure are represented in Figure 3.2. The contour levels of the simulated {110} $\gamma$-surfaces in NiAl, FeAl and CoAl are presented in Figures 3.3, 3.4 and 3.5. Darker shades correspond to lower energy.

The {110} $\gamma$-surfaces in NiAl, FeAl and CoAl had very similar characteristics with a general increase of the shear fault energies from FeAl to CoAl. The only stable faults were observed in the vicinity of the APB faults but deviated from the exact 1/2⟨111⟩ fault. Two stable minima were at two symmetric locations on both sides of the APB fault deviated of 0.05 nm in the ⟨110⟩ direction. The 1/2⟨111⟩ shear was found to be an unstable saddle point. By observation of the stacking sequence of the {110} planes, the energy maxima obtained for 1/2[001] and 1/2[$\bar{1}$10] shears were easily identified as a situation where atoms from the plane above the plane of cut were forced to be on top of the ones from the plane below. The shear in the ⟨111⟩ direction presented the lowest increase in energy. These specific slip directions (⟨100⟩, ⟨110⟩ and ⟨111⟩) were studied in order to determine the unstable stacking fault energy ,$\gamma_{us}$, which is the energetic barrier to shear along these directions. The results, presented in Table 3.1, indicate that ⟨111⟩ is the preferred slip direction along the {110} plane.

The {112} $\gamma$-surfaces were computed by orienting the crystal such that X=[1$\bar{1}$0], Y=[112] and Z=[$\bar{1}\bar{1}$1]. The stacking of the {112} planes is represented in Figure 3.6 and the contour

levels of the simulated {112}$\gamma$-surfaces are presented in Figures 3.7, 3.8 and 3.9 for FeAl. NiAl and CoAl. As observed in the {110} $\gamma$-surface, the only stable fault was in the close vicinity of the exact APB but slightly deviated in the twining direction. Values of $\gamma_{us}$ in the $\langle 111 \rangle$ and $\langle 110 \rangle$ direction along the {112} plane ($\gamma_{us}$) are indicated in Table 3.1. The $\langle 111 \rangle$ direction was the preferred slip direction along the {112} planes.

### 3.2.2  EDM Simulations in CoAl

The same $\gamma$-surfaces were computed in CoAl with the EDM potentials and the stable minimum values, 0.734 and 0.991 $J/m^2$ in the respective {110} and {112} planes, were found for the same shifts as obtained with EAM potentials. Figures 3.10 and 3.11 present a comparative study of the results of EAM and EDM potentials for two cuts along the $\langle 1\bar{1}0 \rangle$ and $\langle \bar{1}\bar{1}1 \rangle$ directions containing the APBs in the respective (110) and (112) planes. The overall shape of both $\gamma$-surfaces did not change with the use of angular forces even if the angular term increases the planar fault energy significantly. As mentioned for the APB fault, the increase in defect energy resulted not only from the addition of the angular term energy but also from a different structure relaxation.

The values of $\gamma_{us}$ were determined along the $\langle 100 \rangle$, $\langle 110 \rangle$ and $\langle 111 \rangle$ directions and are indicated in Table 3.1. The effect of the angular forces on these maxima was an increase from 5% to 30% of the defect energy. According to these results, the preferred slip system in CoAl was predicted to be $\langle 111 \rangle$ {110} with or without the use of angular terms. However, embedded defect method results emphasized the fact that shear energy in CoAl was underestimated in embedded atom method simulations.

## 3.3  DISCUSSION

### 3.3.1  Comparison and General Characteristics in the B2 Compounds

The results obtained in NiAl were very consistent with the ones from previous simulations in NiAl using different potentials [53, 31]. The direction presenting the lower maximum
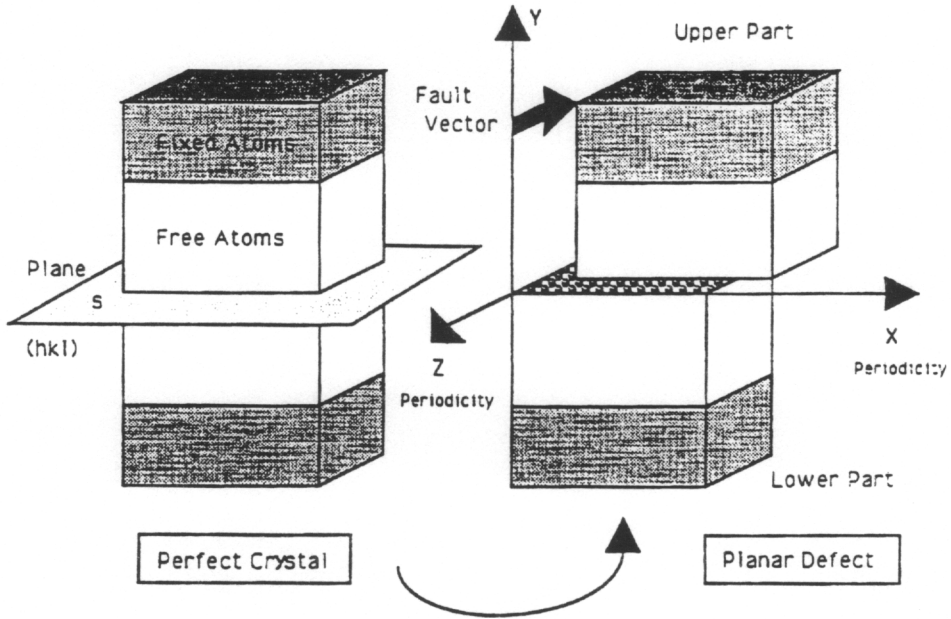
Figure 3.1: Simulation of a planar fault

Table 3.1: Maximum unstable stacking fault energies in $J/m^2$ along specific directions in the (110) and (112) planes in NiAl, FeAl and CoAl

| Potential | Slip | $\langle 111 \rangle(110)$ | $\langle \bar{1}11 \rangle(112)$ | $\langle 100 \rangle(110)$ | $\langle 110 \rangle(110)$ | $\langle \bar{1}10 \rangle(112)$ |
|-----------|------|------|------|------|------|------|
| EAM | FeAl | 0.377 | 0.528 | 0.835 | 0.956 | 1.651 |
| EAM | NiAl | 0.564 | 0.718 | 0.971 | 1.204 | 2.108 |
| EAM | CoAl | 0.888 | 1.094 | 1.197 | 1.699 | 2.122 |
| EDM | CoAl | 0.997 | 1.320 | 1.272 | 1.837 | 2.874 |
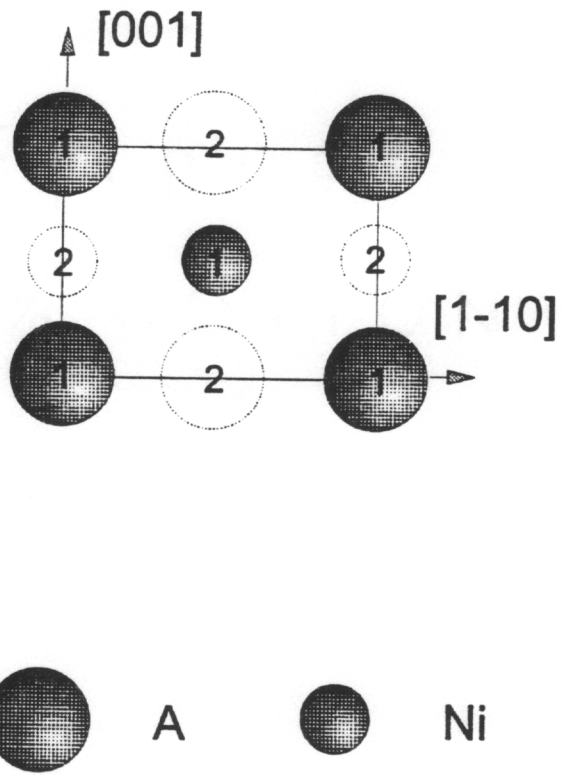
Figure 3.2: Stacking of the {110} planes in B2 A-Ni. The numbers indicate the position of the plane in the ⟨110⟩ direction.
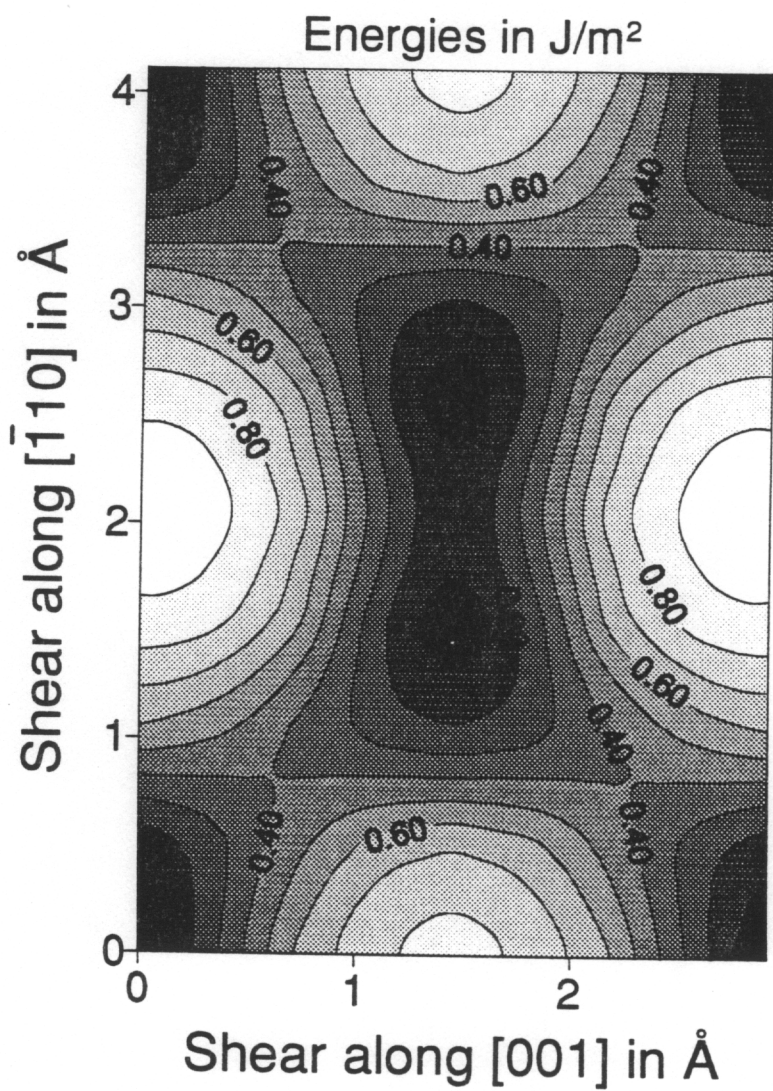
Figure 3.3: Computed {110} $\gamma$-surface in B2 FeAl

49
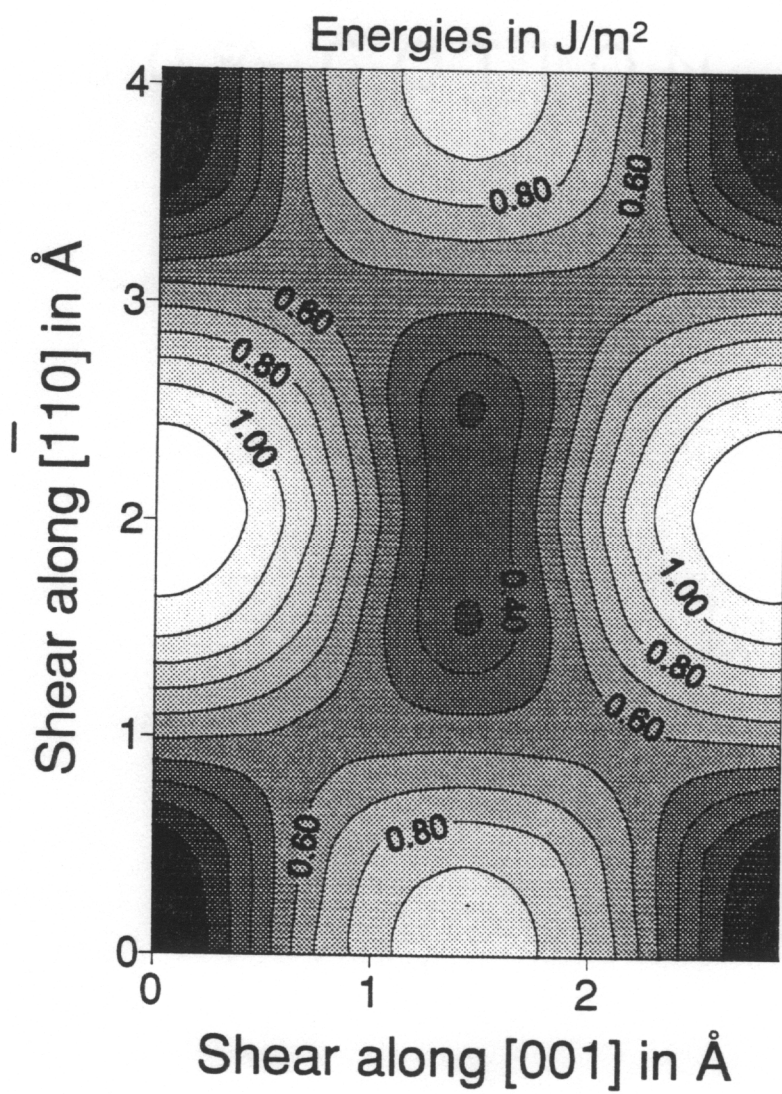
Figure 3.4: Computed {110} $\gamma$-surface in B2 NiAl
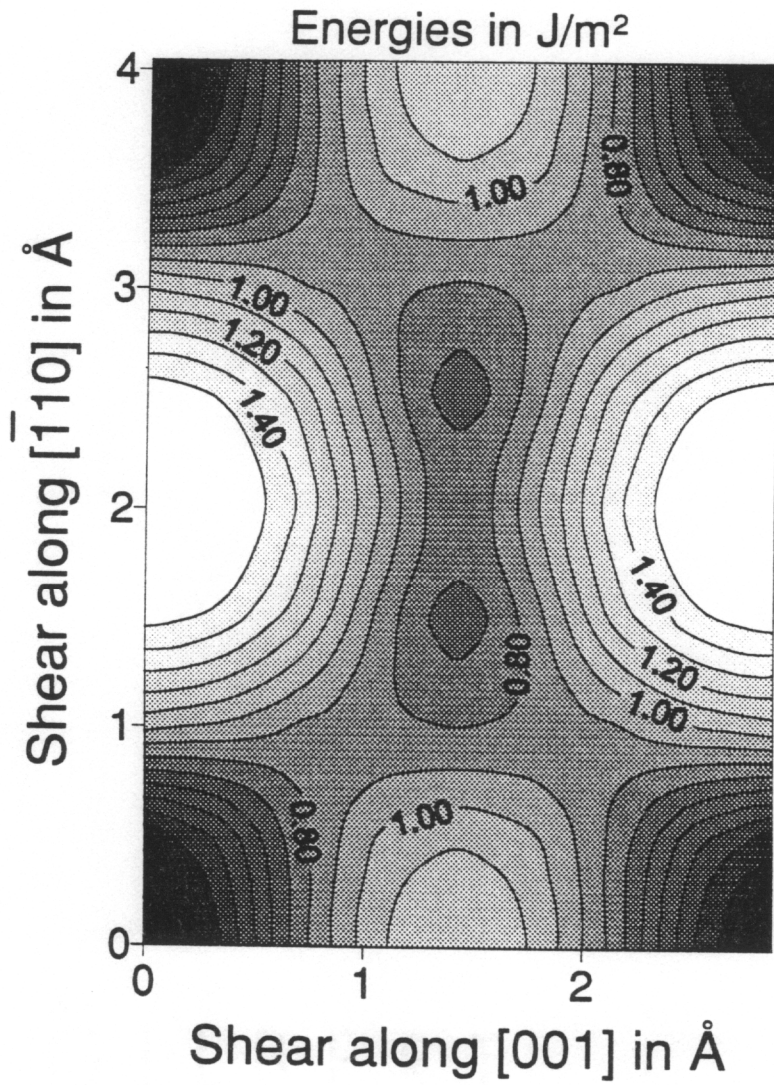
Figure 3.5: Computed {110} γ-surface in B2 CoAl
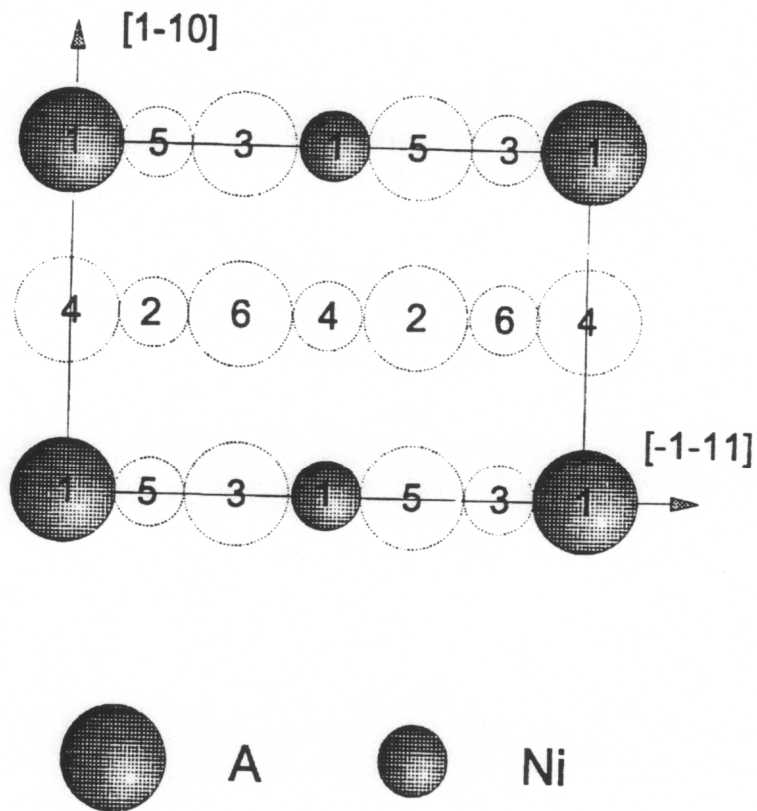
Figure 3.6: Stacking of the {112} planes in B2 compound A-Ni. The numbers indicate the position of the plane in the ⟨112⟩ direction.
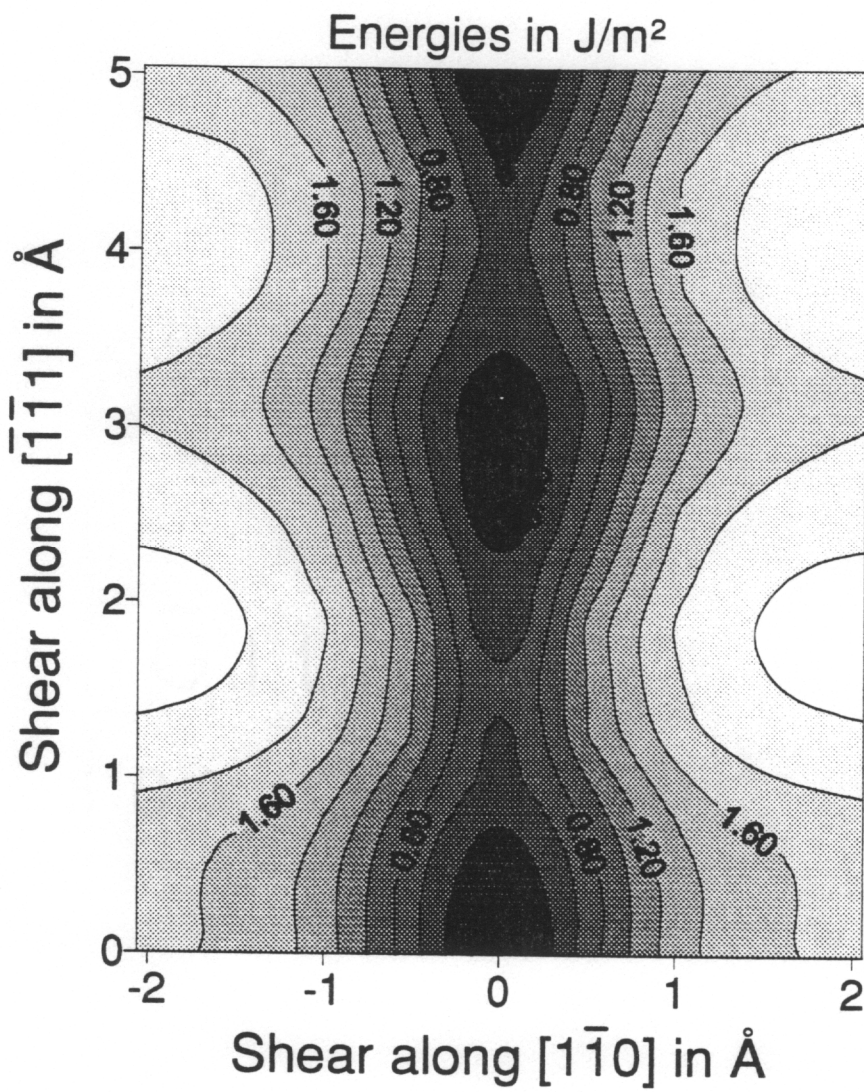
Figure 3.7: Computed {112} $\gamma$-surface in B2 FeAl
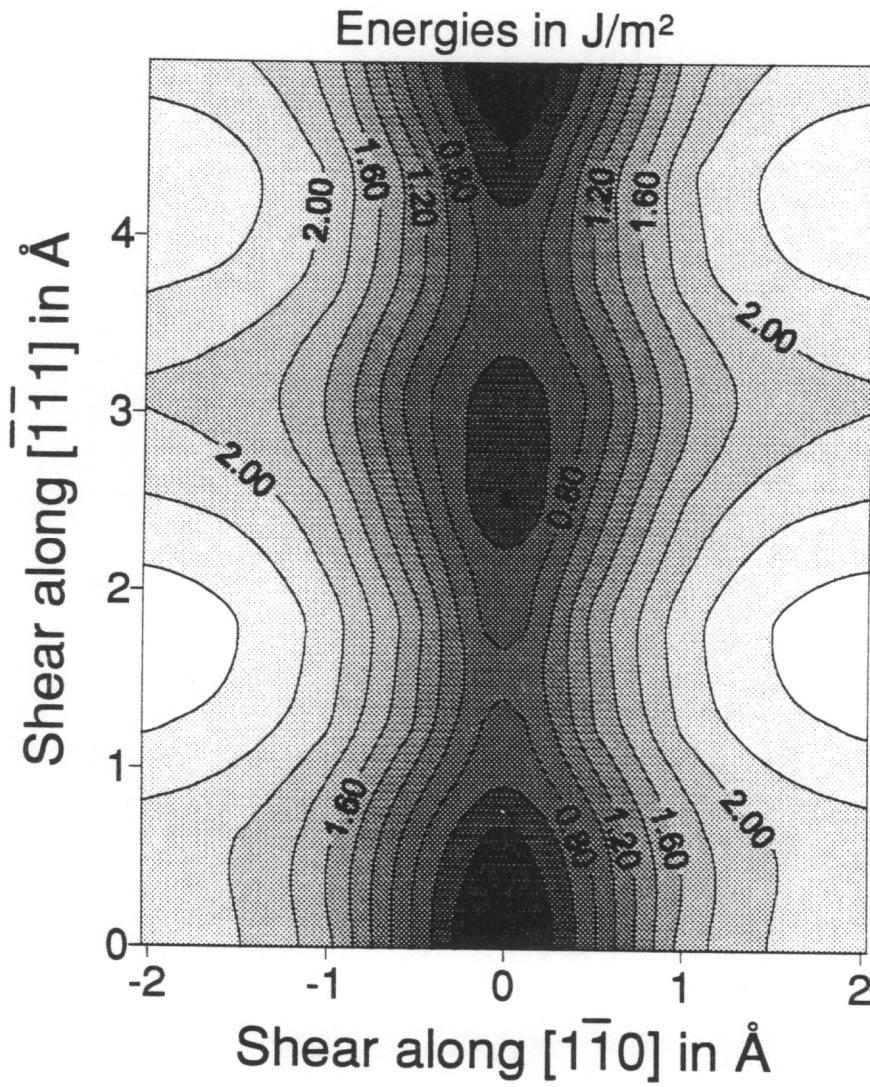
Figure 3.8: Computed {112} γ-surface in B2 NiAl
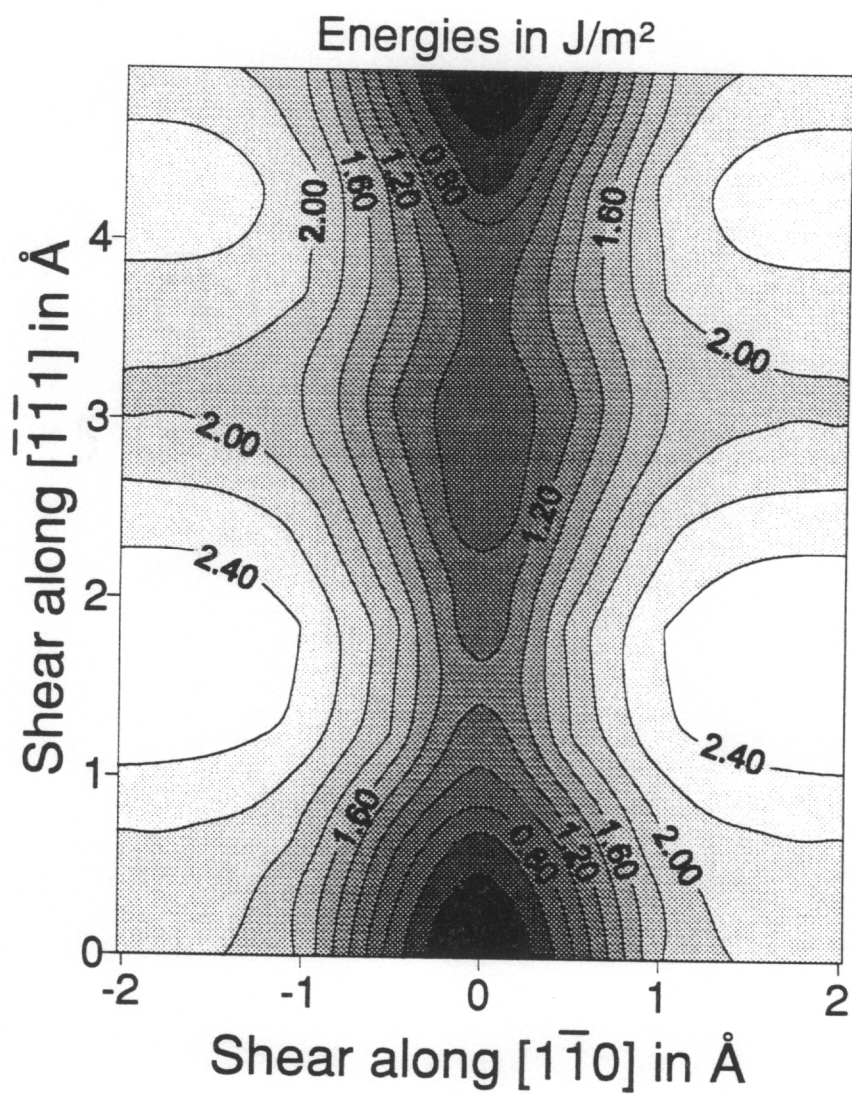
Figure 3.9: Computed {112} γ-surface in B2 CoAl
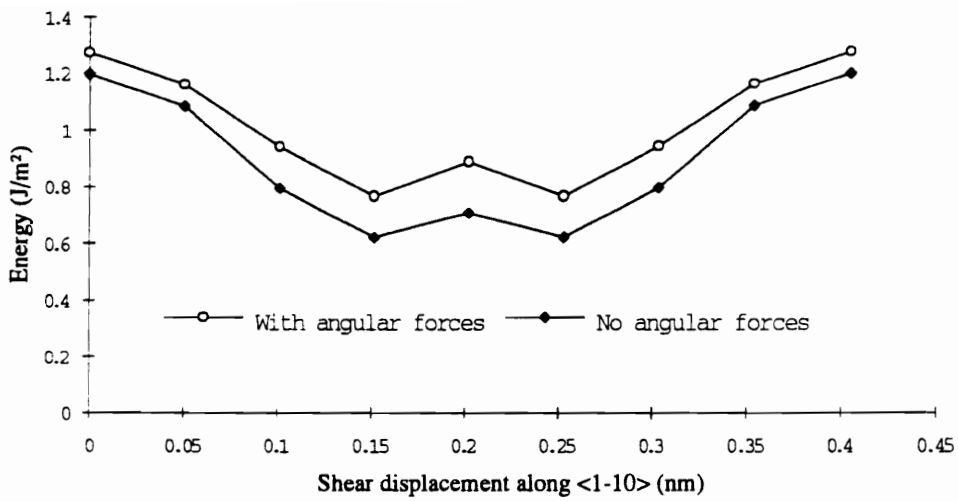
Figure 3.10: Comparison of EDM and EAM potentials in the computation of planar fault energies in CoAl. Cut along the $\langle 1\bar{1}0 \rangle$ direction containing the APB in the $\{110\}$ $\gamma$-surface.
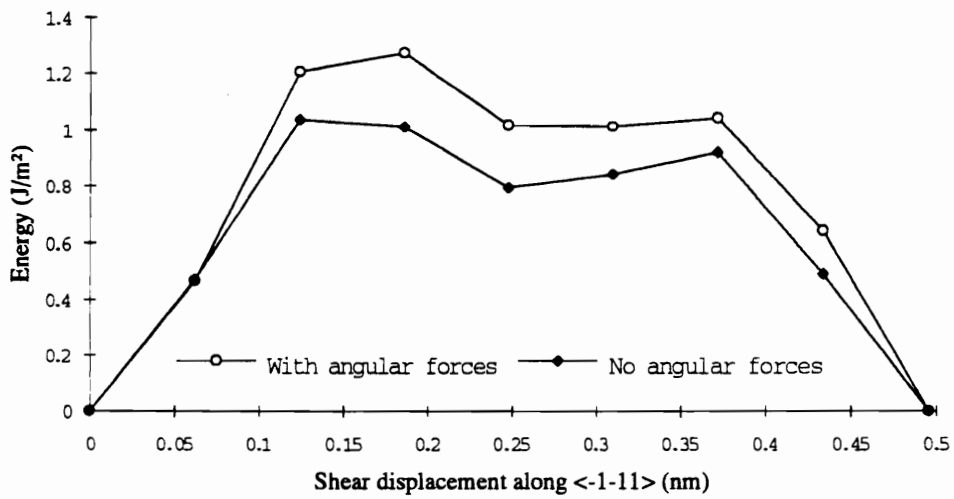
Figure 3.11: Comparison of EDM and EAM potentials in the computations of planar fault energies in CoAl. Cut along the $\langle \bar{1}\bar{1}1 \rangle$ direction containing the APB in the $\{112\}$ $\gamma$-surface.

energy was also the $\langle 111 \rangle$ direction in both $\{110\}$ and $\{112\}$ $\gamma$-surfaces. Figures 3.12 and 3.13 show a comparison of cuts of the $\{110\}$ and $\{112\}$ $\gamma$-surfaces computed with the present potentials and those of Voter et al based on $Ni_3Al$ [53]. The general features were the same and the values of the unstable fault energies were also within a few percent. The potentials developed for B2 NiAl by Rao et al. [31] gave higher values for the values of $\gamma_{us}$ along the $\langle 111 \rangle$ direction ( 600 and 750 $mJ/m^2$ in the respective $\{110\}$ and $\{112\}$ planes). Because the APB energies were also higher (Table 2.2), the general shapes of the $\gamma$-surfaces were still the same.

Besides the similarities of the results obtained in NiAl with different EAM potentials, the computation of $\gamma$-surfaces presented in the study extends this comparison to other B2 aluminides. It was observed that stable planar faults in NiAl, FeAl and CoAl were always deviated from the APB faults in both $\{110\}$ and $\{112\}$ planes. These phenomena may actually be quite general for B2 alloys and independent of the particular potential used since they were found for all the compounds studied. According to the unstable stacking fault energy values, it is predicted that the preferred slip direction was $\langle 111 \rangle$ and the preferred slip plane is $\{110\}$ in all the B2 compounds simulated. It was also observed that stable fault energies and unstable stacking fault energies follow the trend of increasing APB energies along the series FeAl-NiAl-CoAl in both $\{110\}$ (see Figure 3.14) and $\{112\}$ planes (see Figure 3.15).

A more quantitative study was conducted to predict the unstable stacking fault energy as a function of the APB energy. The values of $\gamma_{us}$ along the $\langle 111 \rangle$ direction and the stable planar fault energies were plotted as a function of the respective APB energy along the same plane (see Figure 3.16). As previously mentioned, APB energy values were part of the fitting procedure in the development of the potentials. However, the unstable stacking fault is far from equilibrium condition and the computed value was then a prediction of the potentials. It was found the both $\gamma_{us}$ and stable fault linearly increase with increasing APB energy. Using a linear regression method to fit the data points on Figure 3.16 the relationship between $\gamma_{us}$ and APB was obtained as:
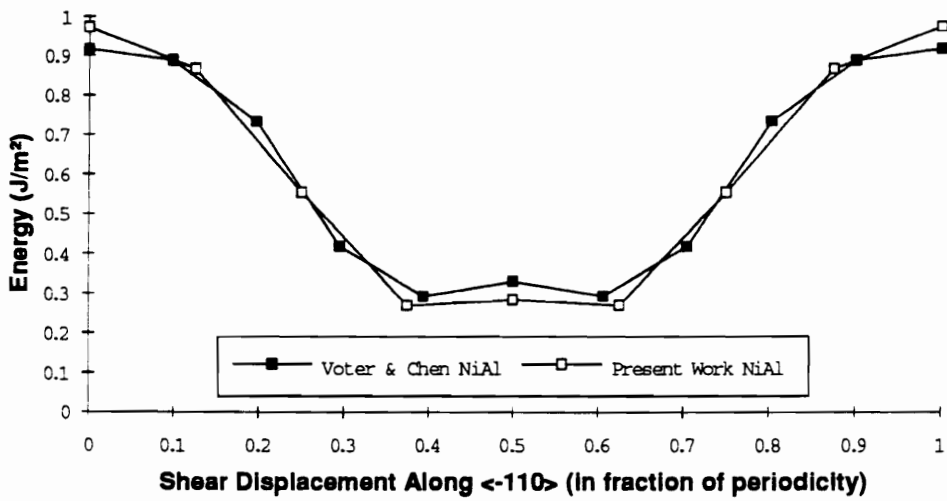
Figure 3.12: Comparison of the results obtained with Farkas [3] and Voter [4] potentials for unstable stacking fault energies and APB in NiAl. Cut along the $\langle 1\bar{1}0 \rangle$ direction containing the APB in the {110} $\gamma$-surface.
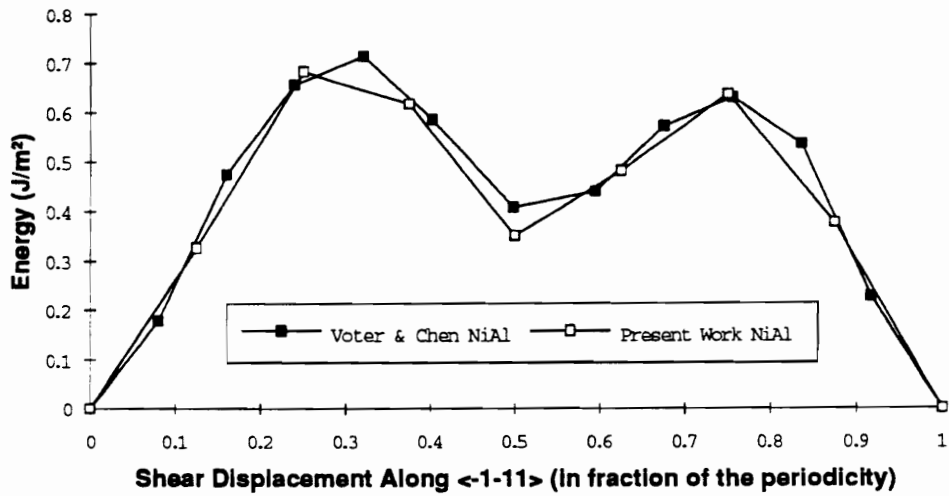
Figure 3.13: Comparison of the results obtained with Farkas [3] and Voter [4] potentials for unstable stacking fault energies and APB in NiAl. Cut along the $\langle \bar{1}\bar{1}1 \rangle$ direction containing the APB in the {112} $\gamma$-surface.
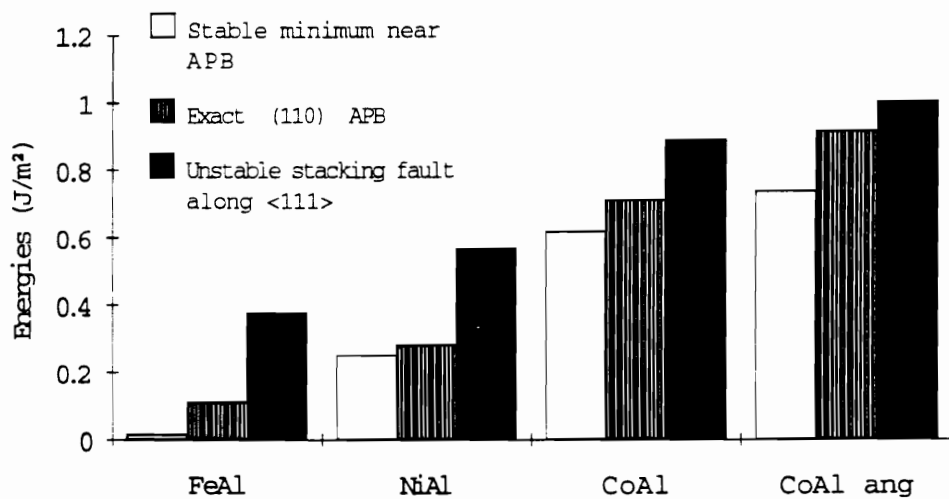
Figure 3.14: Energies of stable planar fault, APB and unstable stacking fault ($\gamma_{us}$) in the $\langle 111 \rangle$ direction for the $\{110\}$ plane in FeAl, NiAl and CoAl. CoAlang indicates the results with angular terms.
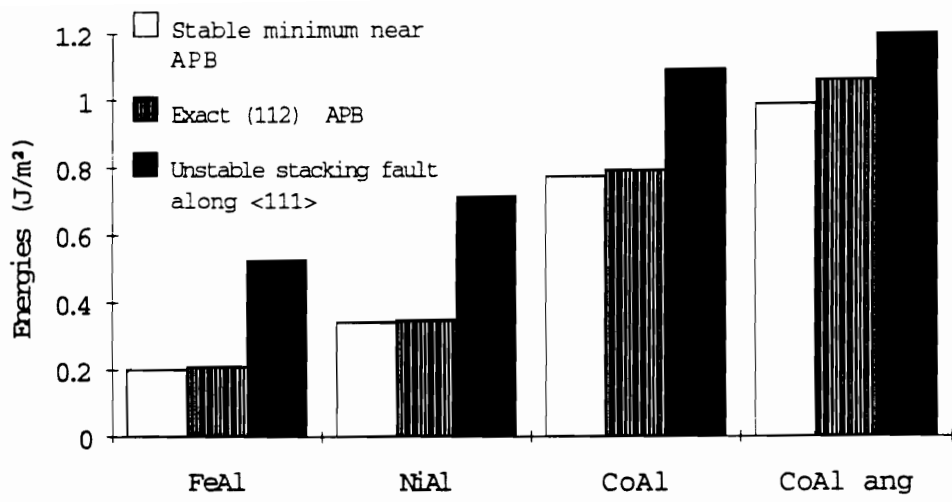
Figure 3.15: Energies of stable planar fault, APB and unstable stacking fault ($\gamma_{us}$) in the $\langle 111 \rangle$ direction for the $\{112\}$ plane in FeAl, NiAl and CoAl. CoAlang indicates the results with angular terms.

$$\gamma_{us} = 0.29 + 0.94 APB (J/m^2) \tag{3.2}$$

and the stable planar fault linearly increases with increasing APB energy such that:

$$Stable Planar Fault = APB - 0.046 (J/m^2) \tag{3.3}$$

These results indicate that the energy difference between these maxima and minima with respect to the APB energy are almost constant. They also clearly show that unstable stacking fault and stable planar fault linearly follow the trend of increasing APB energies from FeAl to CoAl. The following sections will attempt to relate these material properties to the mechanical behavior, and more especially the fracture toughness, observed in this series of B2 intermetallics.

## 3.3.2 Relationship Between $\gamma$-surface Results and Brittle versus Ductile Behavior

Materials may currently be classified as intrinsically brittle or ductile based on two recent criteria developed by Rice [71] and ZCT [72]. Both analyses obtain material properties ($\gamma_{us}$, $\gamma_s$ free surface energy) for borderline materials by equating the critical mode I loading to cleave a crack tip to the corresponding value of loading to emit a dislocation from the tip.

The Rice analysis obtains the critical loadings for emission and cleavage by equating the driving force on distributed shear and opening cores, respectively due to the crack tip stress field at the tip to the local resistance of the slip plane. The analysis assumes that a single slip plane obeying a non-linear displacement traction law emanates from the crack tip, making an angle $\theta$ with the crack plane. In addition, ledge effects which may be caused by dislocation emission are neglected.

Cleavage in mode I is favored to occur on the slip plane directly ahead of the crack, while dislocation emission occurs on a slip plane with non-zero inclination. The critical
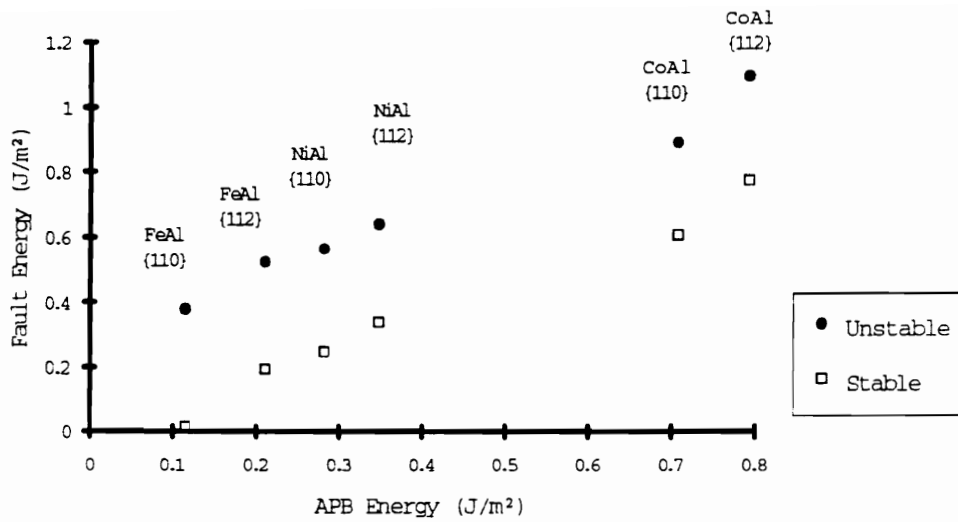
Figure 3.16: Unstable stacking fault energies and stable planar fault energies along the $\langle 111 \rangle$ direction versus APB energy in $\{110\}$ and $\{112\}$ planes

64

crack loading for cleavage is given by

$$k_{Ic} = \sqrt{\frac{4\mu\gamma_s}{1-\nu}}, \tag{3.4}$$

whereas, the corresponding loading for emission is

$$k_{Ie} = \left[\frac{2\mu\gamma_{us}}{1-\nu}\frac{8}{(1+\cos\theta)\sin^2\theta}\right]^{1/2}. \tag{3.5}$$

Here, $k_I$ denotes the mode I crack tip stress intensity factor and $\theta$, the inclination of the slip plane. $\mu$ is the shear modulus of the material. For borderline materials, cleavage and emission are equally likely, so that the corresponding critical loadings are equal. By equating the two critical loadings in Equations (3.4) and (3.5), one obtains the ductile-brittle crossover condition:

$$\frac{\gamma_{us}}{\gamma_s} = \frac{(1+\cos\theta)\sin^2\theta}{4}. \tag{3.6}$$

The Rice analysis suggests that the two properties, $\gamma_{us}$ and $\gamma_s$ at the crossover are linearly related.

ZCT use lattice statics simulations in 2D hexagonal crystals to show that ledge effects alter the crossover condition dramatically and in particular, render the crossover independent of $\gamma_s$. In the ZCT analysis, the critical loading to emit on a slip plane with inclination $\theta$ is

$$k_{Ie} \approx \left[\frac{50\mu\gamma_s\gamma_{us}}{b}\frac{8}{(1+\cos\theta)\sin^2\theta}\right]^{1/2} \tag{3.7}$$

whereas, the loading to cleave directly ahead is unchanged. By equating Equations. (3.7) and (3.4), ZCT obtain the crossover condition

$$\frac{\gamma_{us}}{\mu b} = \frac{(1+\cos\theta)\sin^2\theta}{100(1-\nu)} \tag{3.8}$$

which is independent of $\gamma_s$. The next section proposes to analyze the trend in the behavior of these two criteria ($\frac{\gamma_{us}}{\gamma_s}$ and $\frac{\gamma_{us}}{\mu b}$) for the same cleavage planes and slip systems in the series of aluminides considered.

### 3.3.3 Embedded Atom Method Predictions for Brittle Versus Ductile behavior in FeAl, NiAl and CoAl

The two criteria for brittle to ductile transition presented above are based on the values of the unstable stacking fault energies and free surface energies in the particular materials considered. There is particular interest in the application of these theories to intermetallic alloys since the main obstacle for the widespread use of intermetallics as structural materials is their poor ductility. One of the best available methods to estimate the values of these materials properties is through atomistic calculations using embedded atom potentials [50, 73]. Some calculations of this type have already been carried out by Sun and co-workers [74]but the only B2 compound considered in their study was NiAl. With the development of potentials for FeAl and CoAl, these theories can be applied to two other B2 aluminides.

The free surface energies were simulated by slicing the perfect crystal along a defined crystallographic plane and removing the upper part allowing relaxation of the atoms in all three directions. Periodic boundary conditions were used within the plane similarly to planar fault simulations. Table 3.2 shows the values of the free surface energy corresponding to {111}, {100} and {110} surfaces in FeAl, NiAl and CoAl. Surfaces along the {111} and {100} planes can have different crystallographic structures which depend on the choice of location of the plane of the cut in the crystal. In such situations, the average of the surface energies for each of these configurations was considered. The results indicate that NiAl consistently has the highest free surface energies whereas FeAl has the lowest values.

In perfectly brittle materials the fracture resistance depends solely on the surface energy of the cleavage plane. The cleavage plane in these materials is generally identified as the one with the lowest surface energy. Experimental observations of cleavage in NiAl and CoAl illustrate this point since cleavage in these materials occurs on the {110} plane which is the one with the lowest value of $\gamma_s$. However, experimentally cleavage in FeAl occurs not on the low energy {110} plane but on the {100} plane, a behavior which is similar to that of b.c.c. transition metals [18].

For a comparative study of dislocation emission from the crack tip, we choose $\{110\}$ as the crack plane. Three different slip systems were considered for dislocation emission (see Table 3.3). The Burgers vectors were $1/2\langle 111 \rangle$ for the $\langle 111 \rangle$ slip and the complete $\langle 100 \rangle$ burgers vector for the $\langle 100 \rangle$ slip. The results obtained show that generally the values of both criteria ($\gamma_{us}/\gamma_s$ and $\gamma_{us}/\mu b$) increase following the trend of B2 compounds with increasing APB energies and decreasing fracture toughness. The only case which does not follow this trend is $\gamma_{us}/\gamma_s$ in the $\langle 111 \rangle$ $\{110\}$ slip system for which the value obtained for FeAl is higher than NiAl. For the present comparison and using our EAM potentials both criteria seem to generally predict the observed experimental trend in fracture toughness and it is not possible to establish which one is more accurate.

Table 3.2: Calculated relaxed surface energies $(J/m^2)$

| Materials | {110} Surface | {111} Surface | {100} Surface |
|-----------|---------------|---------------|---------------|
| FeAl | 1.281 | 1.461 | 1.506 |
| NiAl | 1.699 | 2.041 | 1.975 |
| CoAl | 1.546 | 1.855 | 1.815 |

Table 3.3: Comparative analysis of criteria for brittle-ductile behavior

| Crack plane Slip system | {110} $\langle 111 \rangle$ {211} | | {110} $\langle 111 \rangle$ {110} | | {110} $\langle 001 \rangle$ {110} | |
|---------|---------------------|----------------------|---------------------|----------------------|---------------------|----------------------|
| Materials | $\gamma_{us}/\gamma_s$ | $\gamma_{us}/\mu b$ | $\gamma_{us}/\gamma_s$ | $\gamma_{us}/\mu b$ | $\gamma_{us}/\gamma_s$ | $\gamma_{us}/\mu b$ |
| FeAl | 0.41 | 0.033 | 0.29 | 0.023 | 0.65 | 0.044 |
| NiAl | 0.42 | 0.046 | 0.33 | 0.036 | 0.57 | 0.054 |
| CoAl | 0.70 | 0.067 | 0.57 | 0.055 | 0.77 | 0.064 |

# Chapter 4

# DISLOCATION CORE STRUCTURES IN FEAL AND COAL

## 4.1 TECHNIQUE OF SIMULATIONS

### 4.1.1 Simulation of Dislocations

The principle of dislocation simulation used in this study is presented in figure 4.1. The dislocation line was introduced along the center of a cylinder of atoms. In the initial configuration, the atoms within the free block and boundaries were positioned according to anisotropic elastic theory. After the line defect was introduced, the energy was minimized with respect to the coordinates of all the atoms in the free zone.

The boundary conditions were periodic along the dislocation line (Z) and fixed for the external layer of atoms around the cylinder. A typical radius of 9 nm was used for the results presented. No changes in the core structures were observed when this radius was increased to 15 nm. However, when stress was applied to move the dislocations, a radius of 15 nm was used to insure that the boundaries were not affecting the dislocation mobility.

The core structures of the dislocations were obtained after the relaxation process and energy minimization. In order to obtain the critical stress to move the dislocation, stress was applied to the simulated block by defining a stress tensor. The initial atom positions in the free block and boundary layers were then deviated from the stress free elasticity theory dislocation model according to Hooks law that relates stress and strain in the cylinder. During the relaxation process, the dislocation could stay at its initial position or jump to a new position. The critical stress value was identified as the lowest stress value for which the dislocation moved. This was accomplished through a binary search to identify the critical
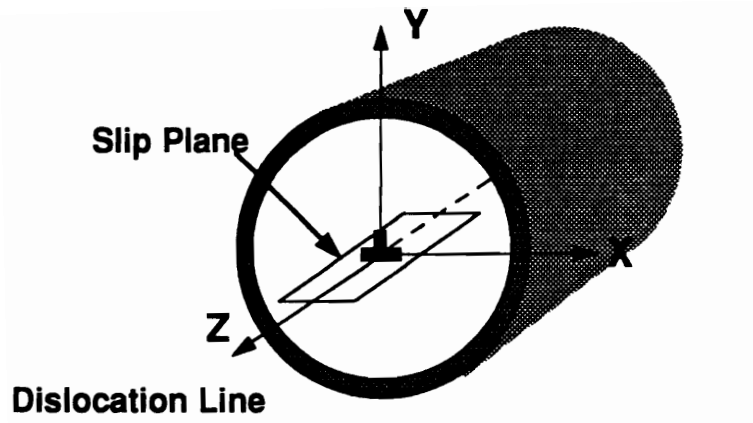
Figure 4.1: Dislocation simulation technique

stress with an accuracy of 10 to 15 %.

### 4.1.2 Representation of Dislocations Cores

The dislocation core structures were plotted using the most frequently used differential displacement scheme to show the relative atomic displacements [43]. In this representation, the viewer is looking down the dislocation line. The atom positions of the perfect lattice and atom types were indicated by circles and triangles. The size of the symbols were related to the different planes that were perpendicular to the dislocation line but located at different depth. In some cases, the relaxed structure, instead of the perfect lattice atomic positions, was represented to study the atom positions in the dislocation core.

The relative displacements of one atom with respect to its first neighbors were then represented by arrows pointing to the considered neighbor. The arrow length can be set to be proportional to the relative displacement in one of the three directions of the coordinate system used in the simulation (see Figure 4.1). This representation is somehow confusing since the arrow direction does not indicate the direction of displacement. In theory, three graphs are necessary to describe the displacement in the three directions of the coordinate system. However, for pure edge and pure screw dislocations only displacements in the direction perpendicular and parallel to the dislocation line were significant and only one graph was necessary.

## 4.2 DISLOCATIONS IN COAL

As in NiAl, $\langle 100 \rangle$ dislocations in extruded CoAl have been experimentally observed, indicating the contribution of these dislocations to the plastic deformation of the material [75, 17]. In contrast with other B2 intermetallics, considerable number of $\langle 111 \rangle$ dislocations, especially the edge $\langle 111 \rangle$ dislocations on the $\{110\}$ plane, have also been observed in CoAl [75]. These dislocations were simulated in this study with the EAM potentials using the same technique as previously used for B2 NiAl [46, 47]. The critical stress values to move

the dislocations were computed for the different slip planes as indicated in Table 4.1. The value of the shear modulus ($\mu = 85.2 GPa$) was computed with Voigt average.

## 4.2.1 The $\langle 100 \rangle$ Slip Along the $\{100\}$ and $\{110\}$ Planes

### Screw Dislocations

Different relaxed core structures were obtained for the $\langle 100 \rangle$ screw dislocation depending on the initial position of the dislocation. Testing different initial positions was part of our simulation procedure to identify possible metastable configuration close to the global energy minimum. The dislocation cores were planar along a single $\{110\}$ plane (Figure 4.2) or spread into two perpendicular $\{110\}$ planes (Figure 4.3). The planar core configuration had the lowest energy.

The first response of the cores to an applied stress on either $\{100\}$ or $\{110\}$ planes was to transform into the planar configuration along the $\{110\}$ plane. The stress required to initiate motion of this dislocation in the $\{110\}$ plane was $0.11 \times 10^{-2}\mu$ (94 MPa). The critical shear stress to induce motion in the $\{100\}$ plane could not be determined because the resolved shear stress experienced along the $\{110\}$ plane always exceeded the barrier to slip along this plane. Cross-slip from the $\{100\}$ plane to the $\{110\}$ plane was observed when the shear stress on the $\{100\}$ plane reached $0.15 \times 10^{-2}\mu$ (128 MPa). Therefore, the critical resolved stress for the $\{110\}$ plane was calculated as $0.15 \times 10^{-2}\mu/\sqrt{2} = 0.11 \times 10^{-2}\mu$.

### Mixed Dislocation

The mixed $\langle 100 \rangle$ $\{100\}$ dislocation was simulated with [120] as the line direction and [100] as the Burgers vector. Figure 4.4 (a) shows the edge components and 4.4 (b) shows the screw components of this mixed dislocation. The core structure obtained was complex and had a mulitylayer structure. The critical stress value to move the dislocation along the $\{100\}$ plane was $9 \times 10^{-4}\mu$ (80 MPa).

72

Table 4.1: Summary of the simulation results obtained for critical stress values for different slip systems in CoAl.

| Slip system | Dislocation type | Critical stress $(\times 10^{-2}\mu)$ | Critical stress (MPa) |
|---|---|---|---|
| $[100](001)$ | Screw | > 0.15 | > 128 |
| $[100](001)$ | Mixed | 0.09 | 80 |
| $[100](010)$ | Edge | 2.91 | 2480 |
| $[00\bar{1}](01\bar{1})$ | Screw | 0.11 | 94 |
| $[100](01\bar{1})$ | Edge | 0.28 | 240 |
| $[111](1\bar{1}0)$ | Screw | 1.88 | 1602 |
| $[111](1\bar{1}0)$ | Edge | 0.09 | 78 |
| $[111](11\bar{2})$ | Screw | > 2.25 | > 1917 |
| $[111](11\bar{2})$ | Edge | 3.76 | 3204 |
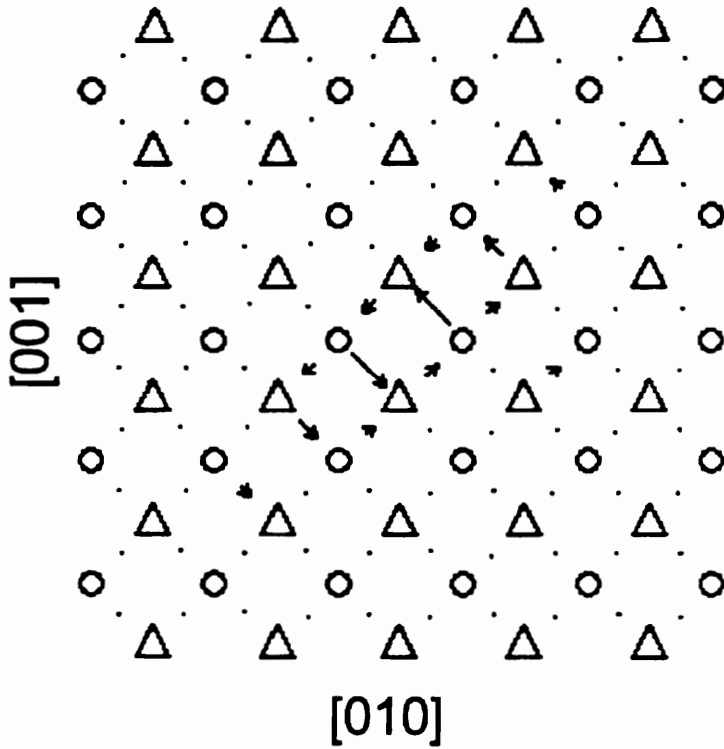


Figure 4.2: Planar core structure of the screw ⟨100⟩ dislocation; $\triangle = Co$, $\bigcirc = Al$
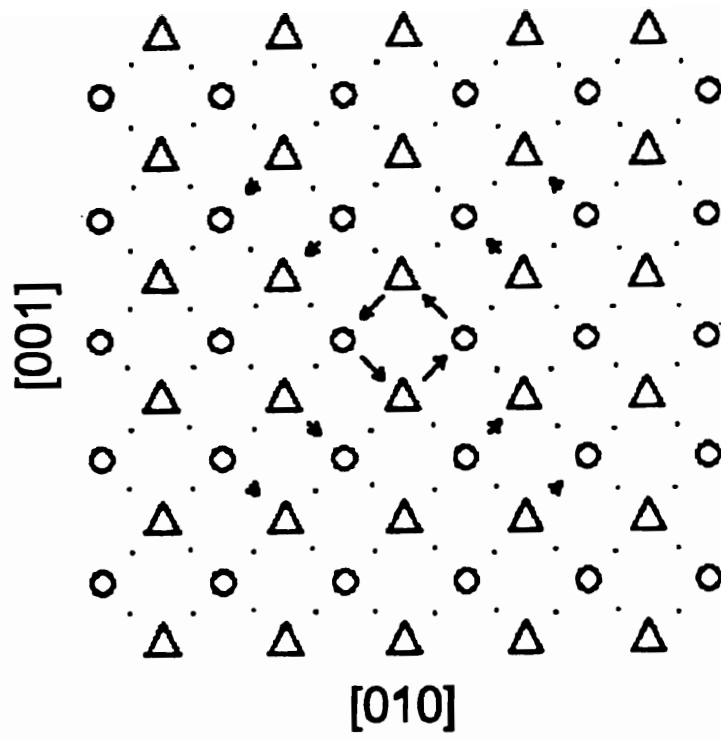
Figure 4.3: Non planar core structure of the screw $\langle 100 \rangle$ dislocation; $\triangle = Co$, $\bigcirc = Al$
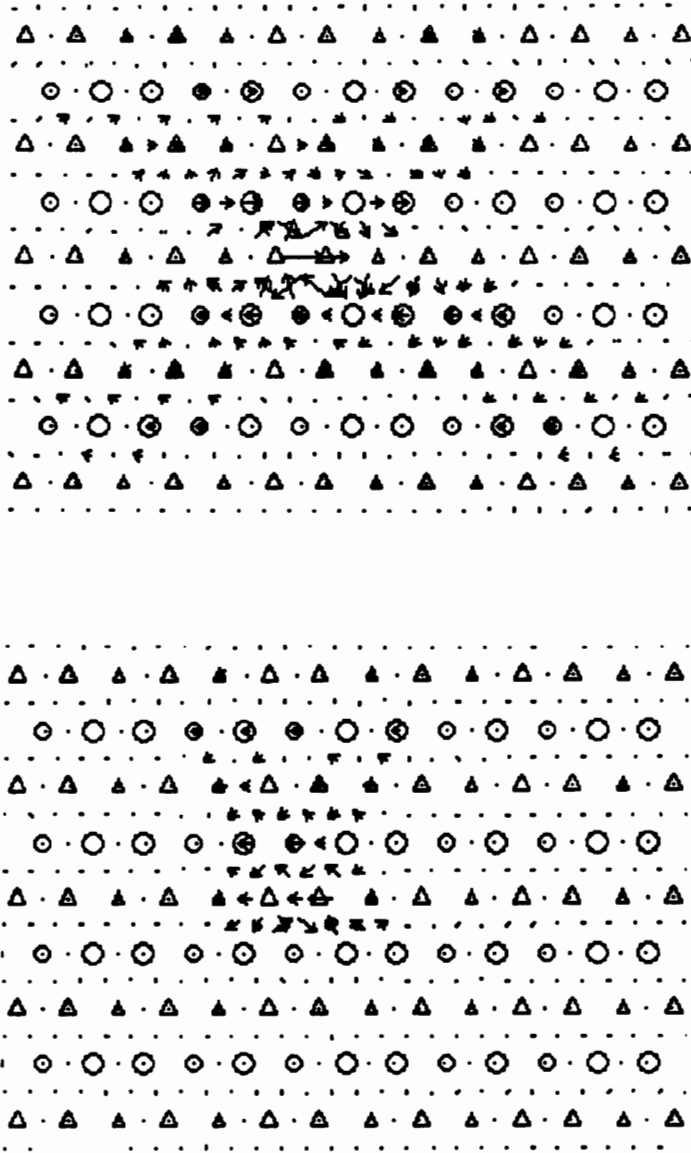
Figure 4.4: The $\langle 100 \rangle$ $\{100\}$ mixed dislocation; (a)Edge displacements;(b) Screw displacements; $\triangle = Co$, $\bigcirc = Al$

## Edge Dislocations

The relaxed core of the edge $\langle 100 \rangle$ $\{100\}$ dislocation is presented in Figure 4.5. The core spread in two perpendicular $\{110\}$ planes as well as in the $[010]$ plane. In order to emphasize the atomistic details of the core structure, Figure 4.6 shows the same dislocation with atomic positions after relaxation. This figure shows that Co $\{100\}$ planes branched out in the center of the core. A core structure with Al planes branching out (or Al rich core) could not be obtained as a local minimum for different initial configurations. This indicates that, similar to B2 NiAl [48], Al rich cores have higher energy than the Al deficient cores. The minimum stress to initiate motion of the $\langle 100 \rangle$ edge dislocation along the $\{100\}$ plane was $2.91 \times 10^{-2}\mu$ (2480 MPa).

In contrast, the edge $\langle 100 \rangle$ $\{110\}$ dislocation had a planar core structure (Figure 4.7). As expected from this core structure, the dislocation was relatively easy to move. The critical stress value obtained for this dislocation was $0.28 \times 10^{-2}\mu$ (240 MPa).

### 4.2.2   The $\langle 111 \rangle$ Slip Along the $\{110\}$ and $\{112\}$ Planes

#### Screw Dislocations

The core structures of the screw $\langle 111 \rangle$ dislocations obtained for two different initial configurations are shown in Figures 4.8 and 4.9. In both cases, the dislocation was initially introduced with a complete $\langle 111 \rangle$ Burgers vector. The complete dislocation was stable (see Figure 4.8) but had higher energy than the dissociated configuration. The core of the complete dislocation was spread into three $\{110\}$ planes showing the three fold symmetry along the $\langle 111 \rangle$ direction. For other initial configurations, the dislocation dissociated spontaneously into two $1/2\langle 111 \rangle$ superpartials which moved from their original position along two $\{110\}$ planes. The cores of the superpartials were spread along the $\{110\}$ planes and the separation distance in between the pair was about 0.8 nm in the $\{112\}$ plane.

Dissociation of the $\langle 111 \rangle$ screw dislocation in the $\{112\}$ plane has been observed in NiAl [31]. The analysis of the relative displacements for the superpartials presently simulated
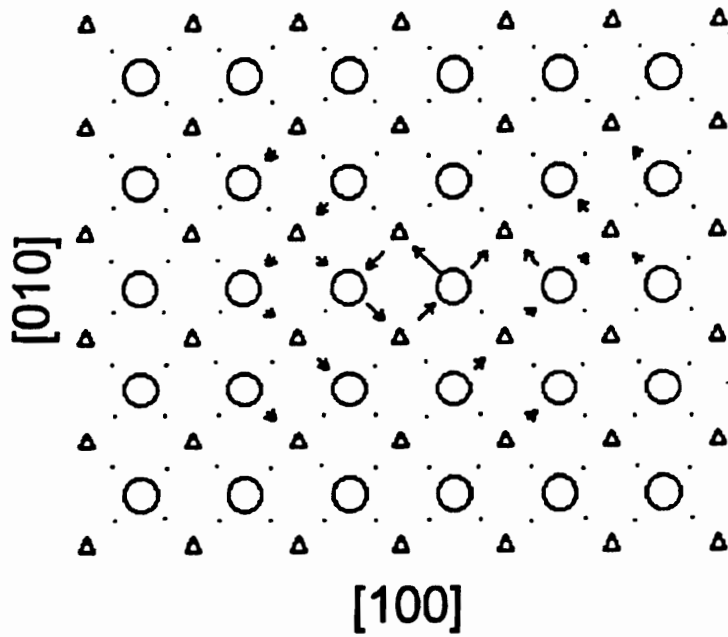
Figure 4.5: Core structure of the edge $\langle 100 \rangle$ $\{100\}$ dislocation; $\triangle = Co$, $\bigcirc = Al$
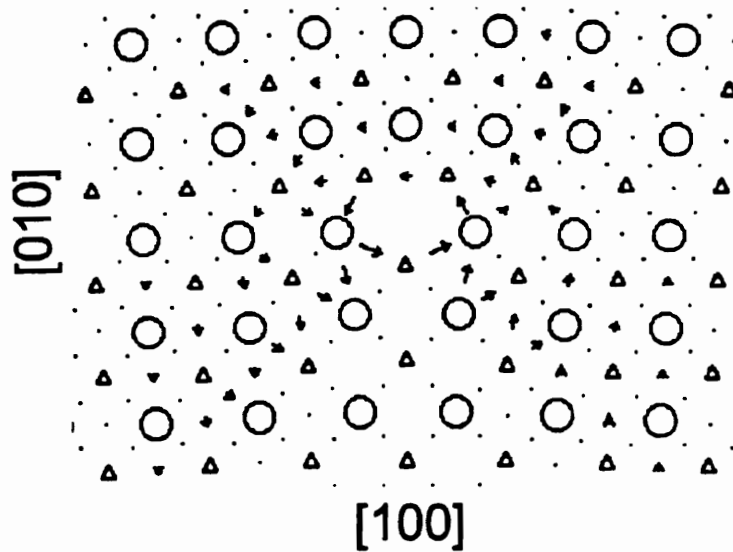


Figure 4.6: Core structure of the edge $\langle 100 \rangle$ $\{100\}$ dislocation; Atoms are in the relaxed positions; $\triangle = Co$, $\bigcirc = Al$

in CoAl did not show any fault along the {112} plane. The APB is accommodated in a zig-zag shaped planar fault along the {110} planes between the two superpartials. This zig-zag configuration is probably due to the nature of the interaction between the two cores since it is not favored by the APB energetics.

Under the influence of stress, the complete ⟨111⟩ dislocations always dissociated into two superpartials independently of the defined slip plane. When the stress was applied to move the dislocation along the {110} plane, the leading superpartial started to move in the {110} slip plane but the trailing one stayed close to its original position in a different {110} plane (Figure 4.10). The superpartials were locked in this configuration until the stress value was increased to $1.88 \times 10^{-2}\mu$ (1602 MPa), which induced the motion of both superpartials along the same {110} plane (Figure 4.11).

The stress was also applied to move the dislocation along the {112} plane. However, motion along this plane was not possible. The initial splitted configuration as seen on Figure 4.9 first changed into two superpartials separated by a {110} APB (see Figure 4.12) for a critical stress value equal to $1.13 \times 10^{-2}\mu$ (963 MPa). These superpartials moved along this {110} plane when the stress applied along the {112} plane reached $2.25 \times 10^{-2}\mu$ (1917 MPa), which implies a resolved stress along the {110} plane estimated as 1355 MPa.

**Edge Dislocations**

The edge ⟨111⟩ (1$\bar{1}$0) dislocation dissociated spontaneously in the (1$\bar{1}$0) plane as shown in Figure 4.13. The core structures of both 1/2⟨111⟩ superpartials were planar. The equilibrium distance in between the two superpartials was about 2.1 nm which agrees with elasticity theory calculations using the energy of the APB fault in the {110} plane. In accordance with the planar core structure, the critical stress was found to be as low as 78 MPa ($0.09 \times 10^{-2}\mu$). This high mobility is in agreement with experimental observations.

The edge ⟨111⟩ (11$\bar{2}$) dislocation had a very complex core structure (Figure 4.14). The dislocation spontaneously dissociated into two 1/2 ⟨111⟩ superpartials that remained close to each other. A very high critical stress value ($3.76 \times 10^{-2}\mu \sim 3200$ MPa) was riquired to

move the leading superpartial in the {112} slip plane (Figure 4.15).

### 4.2.3 Discussion

It is interesting to observe that despite large APB energies, the $\langle 111 \rangle$ dislocations in CoAl dissociated in our simulations, whereas the same dislocations in NiAl did not. This indicates that core effects is dominant in the splitting behavior when superpartials were at distances of less than 2 nm. The same conclusion can be drawn from the observation of a zig-zag APB in the dissociation of the $\langle 111 \rangle$ dislocation in CoAl. The analysis of the energy of the dissociated configuration as a function of separation distances in NiAl [46] also pointed to the same conclusion.

The lowest value of the critical stress was obtained for the edge $\langle 111 \rangle$ superpartials. The $\langle 111 \rangle$ slip at room temperature is characteristic of the b.c.c. structure as a result of the motion of the $1/2 \langle 111 \rangle$ dislocations. In the case of CoAl, the $\langle 111 \rangle$ dislocations observed by Yaney [75] were created during a high temperature deformation (1232 K). It is also important to notice that these dislocations were not purely edge since the dislocation line was $\langle 211 \rangle$ [75]. Therefore, it was not possible to compare directly the experimental observations and the simulation results of this study. However, considering the high values of the shear fault energies in CoAl, the mobility of the $\langle 111 \rangle$ edge dislocation is explained by the planarity of the core structure. This indicates that core structure effects were involved in the splitting and mobility of dislocations and can be more important than APB energies or general shear fault energies.

In agreement with the $\gamma$-surface results, the {110} plane was predominantly involved in the dislocation core structures. The deformation in the dislocation cores mainly took place along the {110} planes. The {110} APB was also preferred in the splitting of the $\langle 111 \rangle$ dislocation. This strong preference was not observed in NiAl [31, 76], for which planar faults along the {112} planes were observed in some dislocation core spreadings.

The different slip systems that have been investigated in this study can be classified in two groups. The first one contains the dislocations that present a planar core structure and

move at critical stress values below 250 MPa. This was the case for the edge dislocation in the $\langle 111 \rangle$ $\{110\}$ slip system and the screw and edge dislocations in the $\langle 100 \rangle$ $\{110\}$ slip system. The second group contains the dislocations with a non planar core structure for which the stress had to reach values greater than 1500 MPa to induce the dislocation motion. This was especially the case of the $\langle 100 \rangle$ $\{100\}$ and $\langle 111 \rangle$ $\{112\}$ slip system. These results were again expected from the $\gamma$-surface computations which predicted the $\{110\}$ planes as the preferred slip planes. This is in contrast with the simulations in NiAl [31] that show slip along the $\{110\}$ and $\{112\}$ planes in the same range of critical stress values.

The $\{100\}$ slip plane was the only one experimentally observed at 673 K in a single crystal [17]. It was also observed in addition to the $\{110\}$ slip plane in extruded CoAl at 1505 K [75]. Our simulation results predict that pure edge and pure screw $\langle 100 \rangle$ dislocations have a very low mobility along the $\{100\}$ planes. However, it was found that the mixed orientation was more mobile and could compete with the other slip systems. Unfortunately, previous studies regarding the experimental observation of the $\langle 100 \rangle$ $\{100\}$ slip do not mention the orientation of the dislocation line with respect to the Burgers vector. This information would be necessary for comparison with the simulation results. It is also not excluded that the effects of kinks or thermal activation can activate the $\langle 100 \rangle$ $\{100\}$ slip. These thermal effects were not included in the simulations presented.

The fact that the planar fault energy increases with the use of angular terms could bring to the conclusion that the critical stress values were underestimated for the dislocations simulated with EAM potentials. The splitting of the $\langle 111 \rangle$ dislocation could also be limited due to the increase in APB energies. However, it seems unlikely that the big gap observed in the mobility of the dislocations along the $\{110\}$ slip planes compared to the $\{100\}$ and $\{112\}$ slip planes could be modified by the use of angular forces since the maximum angular effect on the planar fault energies was in the order of 30%. Besides these qualitative deductions, it is also interesting to consider the ratio of APB energies and shear modulus with and without angular term (see Table 2.6). Since both APB energy and shear modulus increase with angular forces, the ratio used in elasticity theory to compute the dislocation dissociation

stability does not change. These observations lead to the conclusion that angular forces should not drastically change the core structure and behavior of the dislocations.

## 4.3 DISLOCATIONS IN FEAL

In contrast with NiAl and CoAl, the predominant slip system in FeAl is $\langle 111 \rangle$ $\{110\}$ at room temperature [23, 24, 25]. However, simulation of the $\langle 100 \rangle$ and $\langle 111 \rangle$ dislocations were carried out. The core structures of the dislocations and critical stresses to move them were determined for comparison with NiAl and CoAl. The value of the shear modulus $(\mu = 84.5 GPa)$ was computed for FeAl from the elastic constants obtained with the EAM potentials using Voigt average.

### 4.3.1 The $\langle 100 \rangle$ Slip Along the $\{100\}$ and $\{110\}$ Planes

**Screw Dislocations**

The $\langle 100 \rangle$ screw dislocation spontaneously dissociated into two mixed superpartials separated by a stable planar fault (see Figure 4.16). In accord with the $\{110\}$ $\gamma$-surface, this dissociation was described approximately by the following equation:

$$[00\bar{1}]screw = 1/8[\bar{3}\bar{3}4] + SPF\{110\} + 1/8[33\bar{4}] \tag{4.1}$$

where SPF$\{110\}$ indicate the stable planar fault in the $\{110\}$ plane.

The two superpartials had a planar core structure along the $\{110\}$ plane. The separation distance measured from the simulation results and computed from elasticity theory are indicated in Table 4.2. The equilibrium distances computed through these two techniques were in good agreement. The orientation of the Burgers vectors of the superpartials with respect to the dislocation line are also indicated in this table since superpartials and initial complete dislocation did not have the same directions.

Shear stress was applied along the $\{100\}$ and $\{110\}$ planes to induce motion of the superpartials along these planes. The critical stress to initiate motion along the $\{110\}$

was $3.8 \times 10^{-4}\mu$ (32 MPa). The critical shear stress in the $\{100\}$ plane could not be determined because the resolved shear stress along $\{110\}$ was exceeding the barrier to slip along the $\{110\}$ plane. As a result, the superpartials preferred to move along the $\{110\}$ plane containing the APB when the shear stress value was $4.7 \times 10^{-4}\mu$ (40 MPa) along the $\{100\}$ plane. This stress corresponds to a resolved stress value equal to $3.5 \times 10^{-4}\mu$ along the $\{110\}$ plane.

**Mixed Dislocation**

The mixed $\langle 100 \rangle$ $\{100\}$ dislocation was simulated with the dislocation line along $[120]$. This orientation correspond to an angle equal to $60°$ between the dislocation line ($[120]$) and the Burgers vector ($[100]$). Figure 4.17 shows the edge and screw components of this dislocation. The core structure obtained was complex and had a multi-layer structure similar to the one simulated in CoAl [77]. The critical stress value to move the dislocation along the $\{100\}$ plane was $0.53 \times 10^{-2}\mu$ (448 MPa). In this orientation, the dislocation was less mobile than the pure screw orientation.

**Edge Dislocations**

The core structure of the edge $\langle 100 \rangle$ $\{100\}$ dislocation is presented in Figure 4.18. This non planar core was very similar to the one simulated in CoAl [77] and NiAl [3]. The core spread in two perpendicular $\{110\}$ planes as well as in the $\{010\}$ plane. The minimum stress to initiate motion of this dislocation along the $\{100\}$ plane was $1.58 \times 10^{-2}\mu$ (1399 MPa). No change in the core structure was observed when the dislocation was stressed.

The edge $\langle 100 \rangle$ $\{110\}$ dislocation spontaneously dissociated into two superpartials according to the equation:

$$[100]edge = 1/8[433] + SPF\{110\} + 1/8[4\bar{3}\bar{3}] \qquad (4.2)$$

The Burgers vectors of the superpartials had a mixed orientation indicated in Table 4.2. The distance in between the two superpartials was measured as 1.8nm which is in agreement

with elasticity theory. The core structures were mainly planar along the {110} plane (see Figure 4.19). However, small extensions of the cores were also observed in the {100} plane perpendicular to {110}. These superpartials moved when the stress value was set to $3.8 \times 10^{-3}\mu$ (320 MPa). The critical stress was higher than the one obtained for the screw superpartials that had perfectly planar core structures.

## 4.3.2 The $\langle 111 \rangle$ Slip Along the {110} Planes

### Edge Dislocation

The [111] $(1\bar{1}0)$ edge dislocation also dissociated spontaneously into two superpartials separated by an 8 nm long $(1\bar{1}0)$ APB. Elasticity theory computation of the equilibrium distance between these superpartials was in agreement with this simulation with a value computed as 10 nm. A more detailed analysis of these dislocation cores revealed a small screw component as part of a very delocalized core structure (Figure 4.20). By plotting the screw and edge relative displacements of one of the superpartials, the segment from A to C of the core appeared to be mainly screw while the segment C to D was mixed.

This mixed segment was explained as a result of the deviation of the minimum energy in the {110} $\gamma$ surface (Figure 4.21). Since the APB was not the energy minimum, the relaxation of the core followed exactly the path dictated by the $\gamma$ surface. The letters on Figure 4.21 indicate the different steps observed in the core spreading and shows that a mixed orientation should appear along the segment CD. The dissociation is then more accurately described by the equation following, where SPF{110} indicates the stable planar fault in the {110} plane:

$$[111]edge = 1/8[334] + SPF\{110\} + 1/4[110] + SPF\{110\} + 1/8[334] \qquad (4.3)$$

Such core structures have not been observed in NiAl and CoAl probably due to the proximity of the superpartials [3, 77]. The critical stress value for these planar cores was very low $(10^{-4}\mu$ - 8 MPa), following the prediction of the Peierls Nabarro model for a large delocalization of the strain along the slip plane.
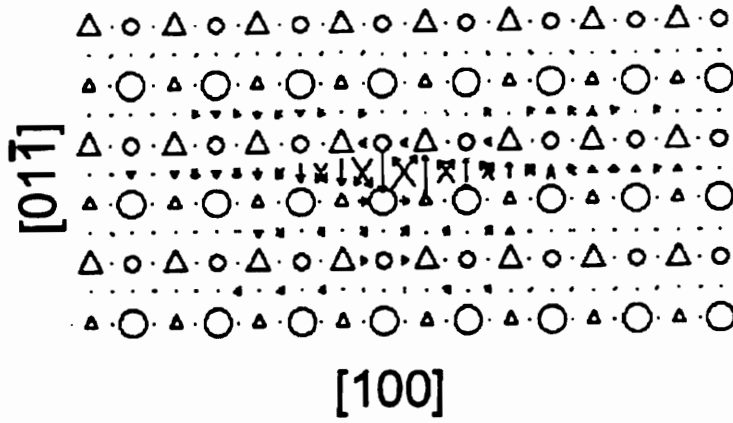
Figure 4.7: Core structure of the edge $\langle 100 \rangle$ $\{110\}$ dislocation; $\triangle = Co$, $\bigcirc = Al$

Table 4.2: Summary of the results of the simulations of $\langle 100 \rangle$ and $\langle 111 \rangle$ dislocations in FeAl. S, M and E indicate the screw, mixed and edge character of the initial dislocations. D indicates if the dislocation is dissociated and $\theta$ is the angle in degree between the superpartials and the dislocation line. The separation distances in parenthesis were computed according to elasticity theory.

| Slip System | Feature | Separation Distance (nm) | Critical Stress | |
|---|---|---|---|---|
| | | | MPa | $\times 10^{-2}\mu$ |
| $\langle 100 \rangle\{100\}$ Screw | D $1/2\langle 111 \rangle$ $\theta=54.7$ | 3.8 (4.2) | >40 | >0.047 |
| $\langle 100 \rangle\{100\}$ Mixed | $\langle 100 \rangle$ $\theta=60$ | N/A | 448 | 0.53 |
| $\langle 100 \rangle\{100\}$ Edge | $\langle 100 \rangle$ $\theta=90$ | N/A | 1399 | 1.58 |
| $\langle 100 \rangle\{110\}$ Screw | D $1/2\langle 111 \rangle$ $\theta=54.7$ | 3.8 (4.2) | 32 | 0.038 |
| $\langle 100 \rangle\{110\}$ Edge | D $1/2\langle 111 \rangle$ $\theta=34.3$ | 1.8 (1.7) | 320 | 0.38 |
| $\langle 111 \rangle\{110\}$ Screw | D $1/2\langle 111 \rangle$ $\theta=0$ | 6 (7.6) | 216 | 0.25 |
| $\langle 111 \rangle\{110\}$ Edge | D $1/2\langle 111 \rangle$ $\theta=90$ | 8 (10.2) | 8 | 0.01 |
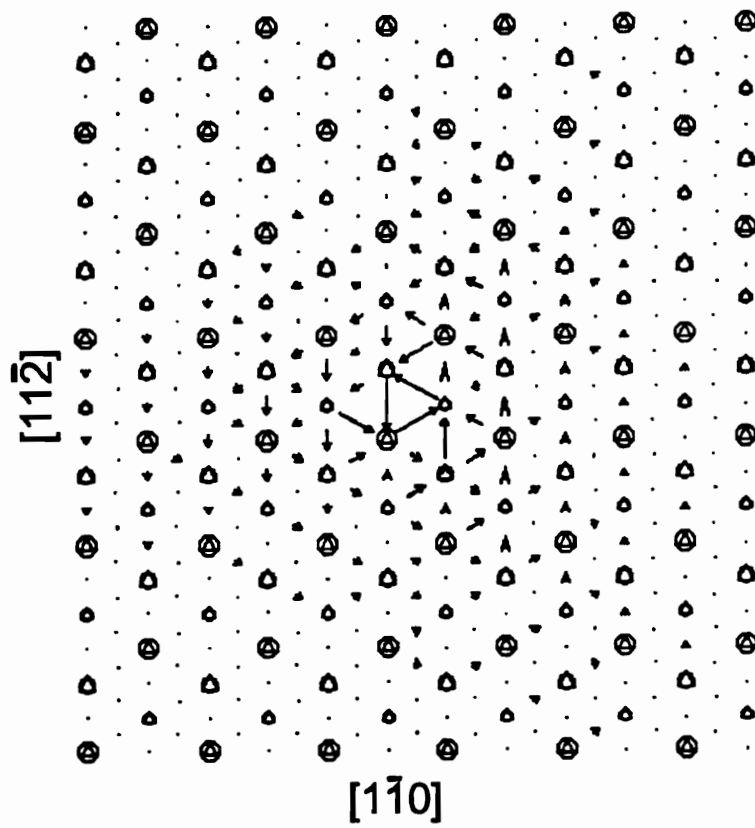
Figure 4.8: Core structure of the complete ⟨111⟩ screw dislocation; $\triangle = Co$, $\bigcirc = Al$
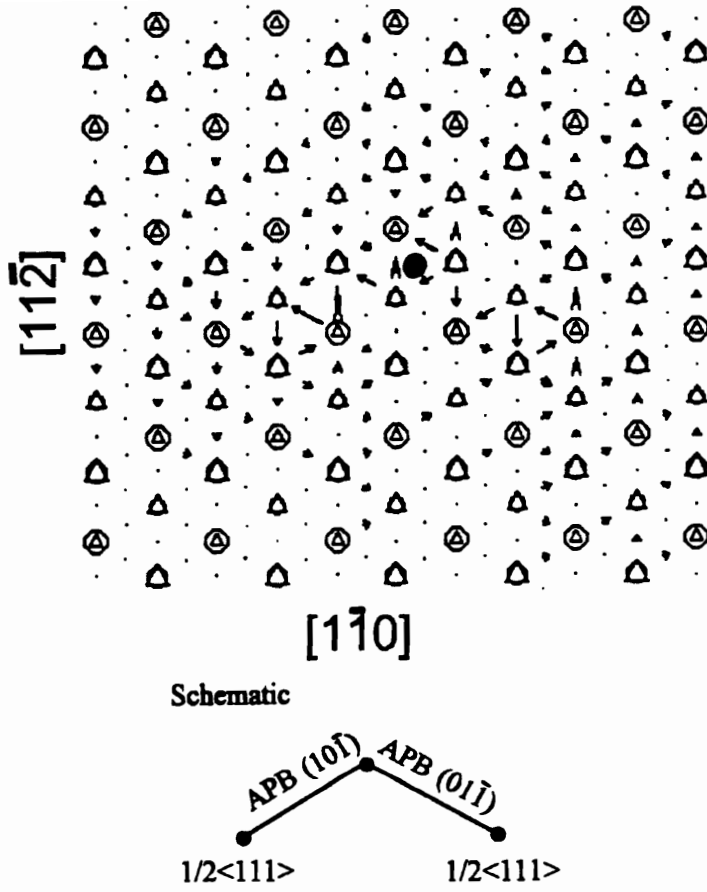
Figure 4.9: Core structure of the $1/2 \langle 111 \rangle$ screw superpartials; $\triangle = Co$, $\bigcirc = Al$
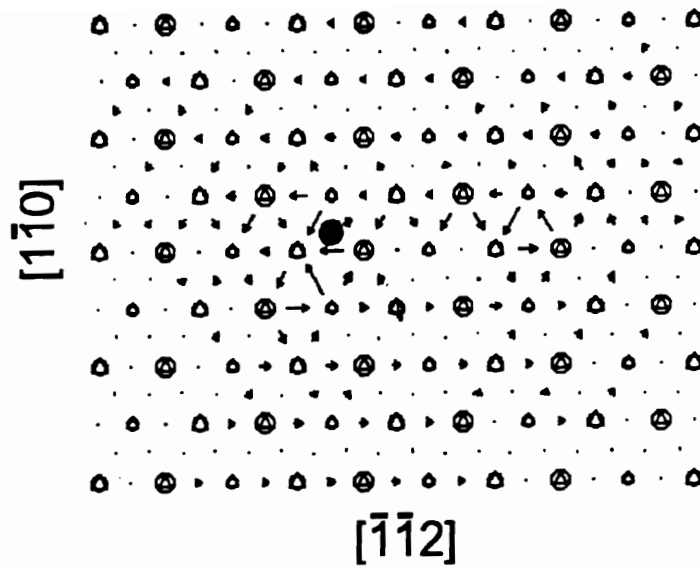
Figure 4.10: Core structures of the $1/2\langle 111 \rangle$ $\{110\}$ screw superpartials with an applied stress below $1.88 \times 10^{-2}\mu$; $\triangle = Co$, $\bigcirc = Al$, $\bullet$ = Initial position
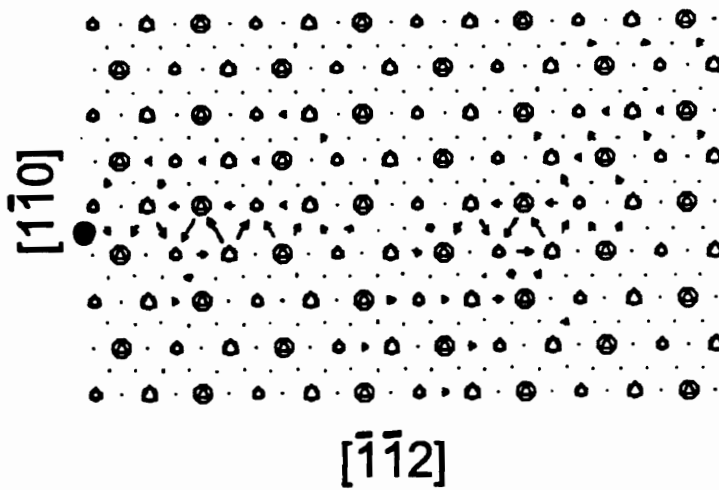


Figure 4.11: Core structures of the $1/2\langle 111 \rangle$ $\{110\}$ screw superpartials with an applied stress above $1.88 \times 10^{-2}\mu$; $\triangle = Co$, $\bigcirc = Al$, $\bullet$ = Initial position
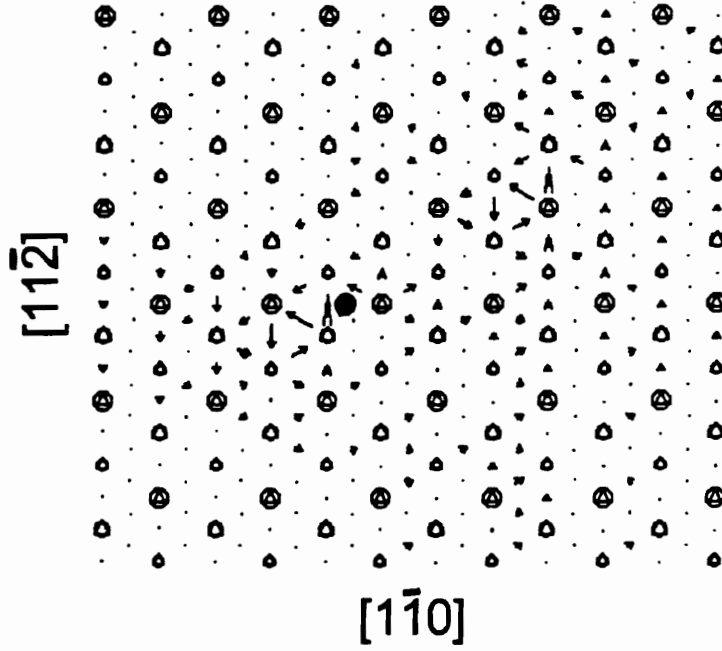
Figure 4.12:  Core structures of the $1/2\langle111\rangle$ $\{112\}$ screw superpartials with an applied stress below $1.13 \times 10^{-2}\mu$; $\triangle = Co$, $\bigcirc = Al$, $\bullet$ = Initial position
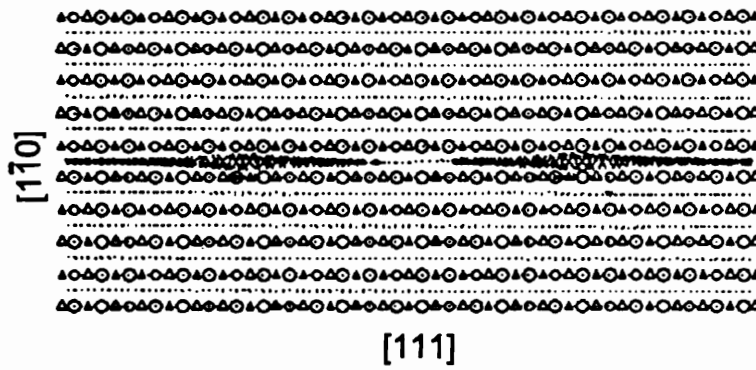


Figure 4.13: Core structures of the $1/2\langle111\rangle$ $\{110\}$ edge superpartials; $\triangle = Co$, $\bigcirc = Al$
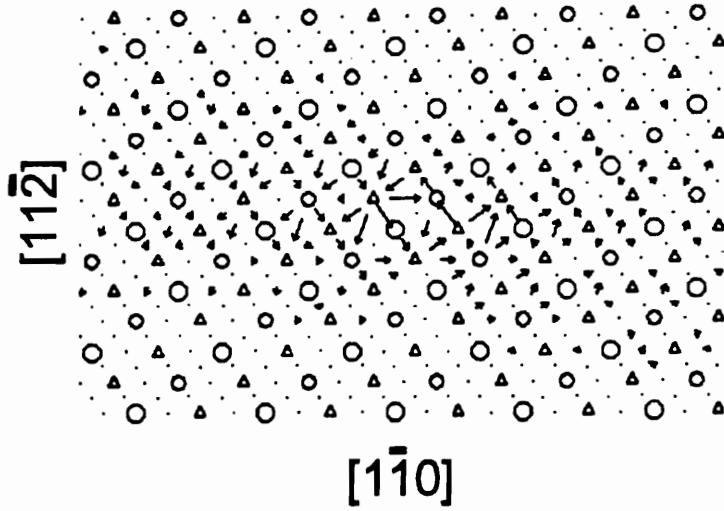
Figure 4.14: Core structures of the $1/2\langle 111 \rangle$ $\{112\}$ edge superpartials; $\triangle = Co$, $\bigcirc = Al$
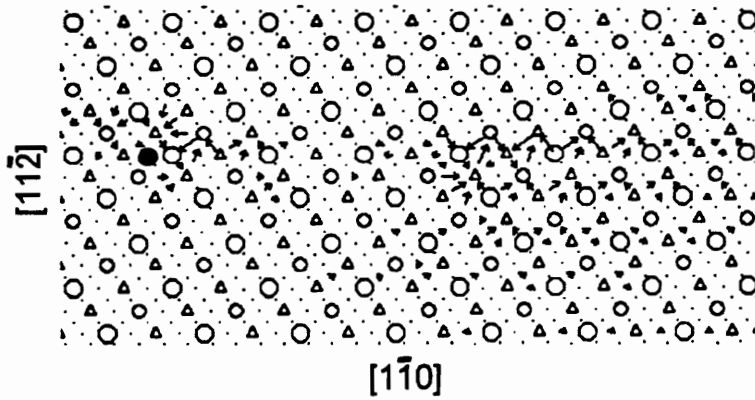


Figure 4.15: Core structures of the $1/2\langle 111 \rangle$ $\{112\}$ edge superpartials; The applied stress $(3.76 \times 10^{-2}\mu)$ along the $\{112\}$ slip plane induce motion of the leading superpartial on the right; $\triangle = Co$, $\bigcirc = Al$, $\bullet =$ Initial position

89

## Screw Dislocations

The complete $\langle 111 \rangle$ screw dislocation was found to be meta-stable in our simulation (see Figure 4.22). The dislocation core spread in three $\{110\}$ planes as would predict the three fold symmetry along the $\langle 111 \rangle$ direction. In order to find the global energy minimum, different elastic centers were used as initial configurations. This procedure insured that the final core structure was not a local minimum. The use of different elastic centers revealed that spontaneous dissociation of the complete dislocation was energetically favored (Figure 4.23). The dissociation was also observed as a first response to an applied stress for all initial positions. The spontaneous dissociation created two superpartials, oriented close to $1/2\langle 111 \rangle$, in two different $\{110\}$ planes. The overall equilibrium distance was around 0.9 nm in between the superpartials. This observed separation was smaller than the equilibrium distance predicted by elasticity theory (7.6 nm) and was a result of the cross slip of the superpartials that could not move further in this sessile configuration. With increasing stress values, the leading superpartial moved along the $\{110\}$ slip plane, while the trailing superpartial, spread in another $\{110\}$ plane, was locked at the initial position (Figure 4.24). The superpartials were still locked in this configuration at stress values as high as $0.25 \times 10^{-2} \mu$ (216 MPa).

In a second set of simulations, the two superparials separated by a $\{110\}$ APB were initially introduced in the simulation block. The equilibrium distance between the two superpartials was found to be 6 nm in accord with elasticity theory. The result of this simulation is presented in Figure 4.25. For clarity, this figure represents only one side of the all picture since the two superpartials were symmetric with respect to the $\{112\}$ plane. Three dislocations were found along the APB plane according to the dissociation equation:

$$[111]screw = 1/8[334] + SPF\{110\} + 1/4[110] + SPF\{110\} + 1/8[334] \qquad (4.4)$$

where SPF stands for stable planar fault in the $\{110\}$ plane. In Figure 4.25 the 1/8[334] superpartial is on the right and half of the 1/4[110] dislocation is on the left. This dissociation was similar to the one observed for the edge $\langle 111 \rangle$ dislocation.

In contrast with the edge orientation, the core of the 1/8[334] screw superpartials did not spread in the {110}APB plane. The spreading was observed in other equivalent {110} plane that do not contain the APB. This feature was already observed in simulated B2 intermetallics [45]. Stress was applied to move these superpartials along the {110} APB plane. The behavior of the superpartials was similar to the one obtained from the initial complete dislocation. As shown in Figure 4.26, the leading superpartial cross slipped in a {110} plane other than the APB plane and was locked in this configuration at stress values as high as $0.25 \times 10^{-2}\mu$ (216 MPa).

### 4.3.3 Discussion

The $\langle 111 \rangle$ and $\langle 100 \rangle$ dislocations were our principal interests in this study. As a main result, it was found that the $\langle 100 \rangle$ dislocations that did not dissociate into two superpartials close to $1/2\langle 111 \rangle$ were difficult to move. Because molecular statics does not consider thermal activation, our results are pertinent to low temperature behavior. Based on the critical stress values simulated, $\langle 111 \rangle$ was the preferred slip direction at low temperatures. This prediction is in agreement with the experimental observations of the $\langle 111 \rangle$ slip at temperatures below $0.4\ T_m$. However, as can be seen from the dissociation of the $\langle 100 \rangle$ dislocation, the interaction of two $1/8\langle 334 \rangle$ superpartials can also explain an overall $\langle 100 \rangle$ slip.

Transmission electron microscopy studies of the $\langle 111 \rangle$ dislocation from samples deformed below the transition temperature [23] do not show any preferential orientation for the dislocation lines. The dislocations experimentally observed are not straight which implies that the angle between the dislocation line and the Burgers vector is not fixed. Therefore, The mobility of the dislocation is probably limited to the less mobile part of the dislocation. In this case, the lowest value of the critical stress simulated for the pure edge $\langle 111 \rangle$ dislocation overestimates the mobility of the dislocation.

The dissociation of the $\langle 100 \rangle$ dislocations into two $1/2\langle 111 \rangle$ superpartials has been suggested in previous experimental studies [78, 79] but they cannot be explained with elasticity theory (violation of Frank's rule). The criteria of dislocation dissociation assumes

91

that the dislocation energies are proportional to $b^2$. However, if the dislocation dissociates into two $1/8\langle 334\rangle$ dislocations, the energy of the complete dislocation is almost equal to the sum of the energies of the two superpartials. For this configuration, the atomistic simulation results indicate that the dissociation is possible.

The critical stress values to move the dislocations were obtained for four different orientations of the $1/2\langle 111\rangle$ superpartials with respect to the dislocation line. The mobility of the superpartials along the $\{110\}$ plane containing the APB was seen to decrease when the burgers vector was oriented toward the screw orientation. The motion of the pure screw superpartials could not be achieved along the APB plane because of the cross slip of one of the superpartials. As opposed to the behavior of the same $1/2\langle 111\rangle$ dislocations in a b.c.c. metal, superpartials in FeAl have to move in pairs along the same slip plane due to the existence of the APB fault in between. When cross slip occurs, the two superpartials are locked in a sessile configuration that requires higher stress values to overcome, resulting in a decrease of the mobility of the dislocations. The motion of the superpartials is then expected to alternate from one $\{110\}$ slip plane to an other when the dislocations glide through the material in a deviated motion.

Experimental observations of the $\langle 100\rangle$ dislocation in samples deformed above the transition temperature show dislocations that are mostly of edge or mixed character [23]. It was also conclude that $\langle 100\rangle$ dislocations observed did not cross slip in contrast with the $\langle 111\rangle$ dislocations. The simulation results presented in this study agree perfectly with these experimental observations. Therefore, it can be predicted that the mobility of the $1/2\langle 111\rangle$ superpartials decreases with increasing temperatures as a result of cross slip activation. At higher temperatures, $\langle 100\rangle$ slip is activated with the motion of the complete $\langle 100\rangle$ dislocation that do not involve the APB fault. A pair of $1/2\langle 111\rangle$ superpartials as indicated in Equation 4.3 and 4.4 could also be responsible for slip at high temperature since these superpartials did not cross slip in the simulations.

92
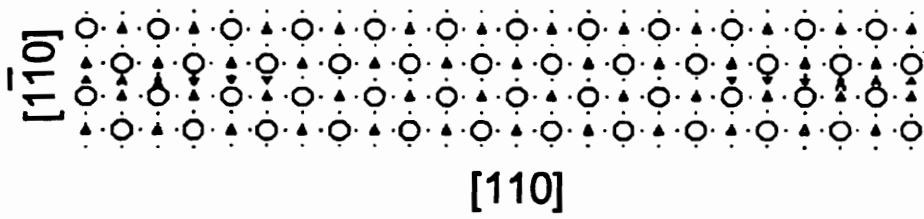
Figure 4.16: The $[00\bar{1}](1\bar{1}0)$ screw dislocation spontaneously dissociated into two $1/2 \langle 111 \rangle$ mixed superpartials separated by a 3.8nm long $\{110\}$ APB; $\triangle = Fe$, $\bigcirc = Al$
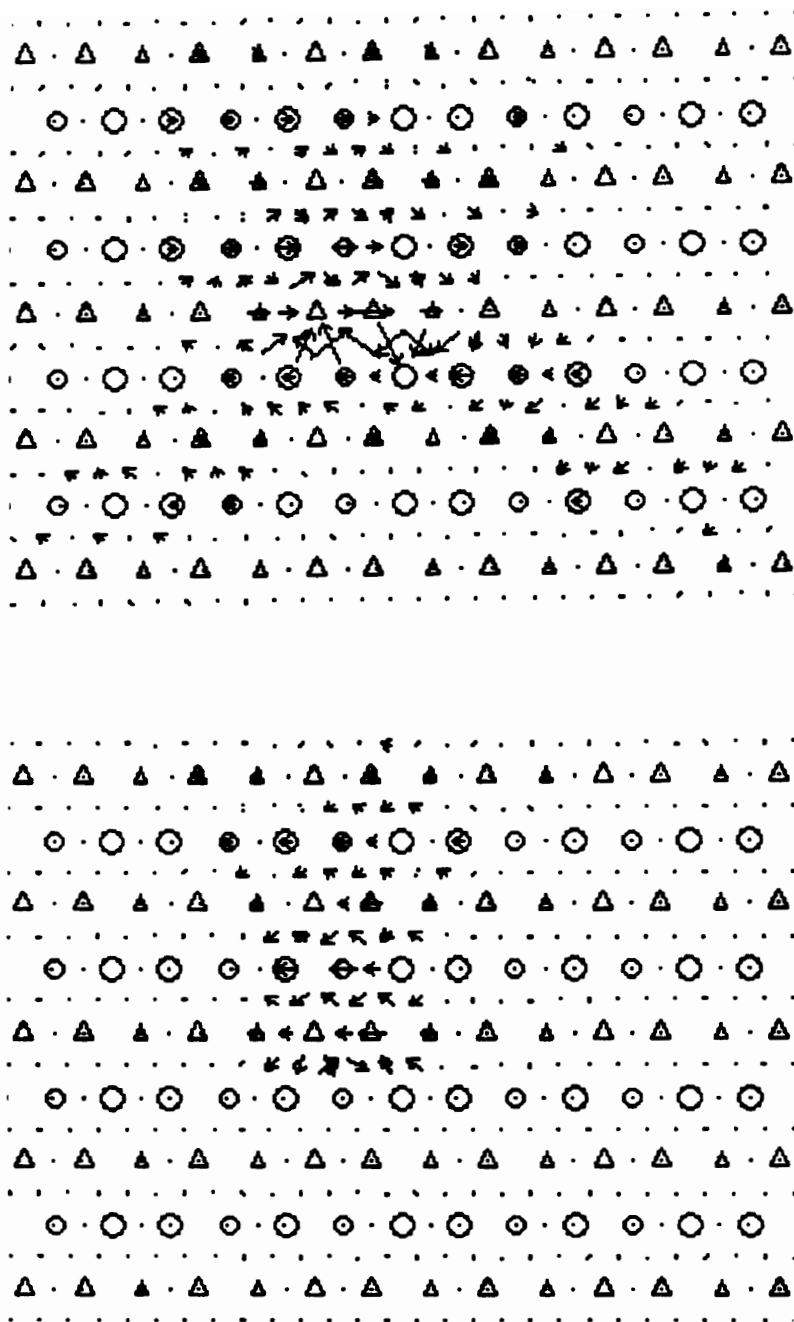
Figure 4.17: The ⟨100⟩ {001} mixed dislocation; Top) Edge displacements; Bottom) Screw displacements; △ = Fe, ○ = Al
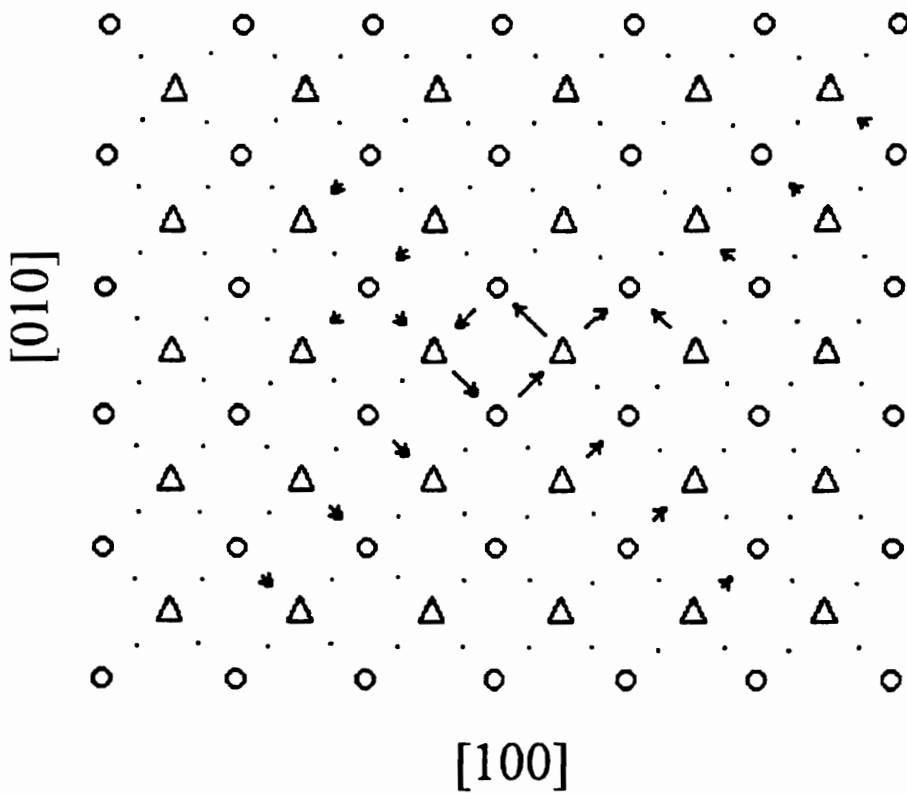
Figure 4.18: The [100](010) edge dislocation; $\triangle = Fe$, $\bigcirc = Al$
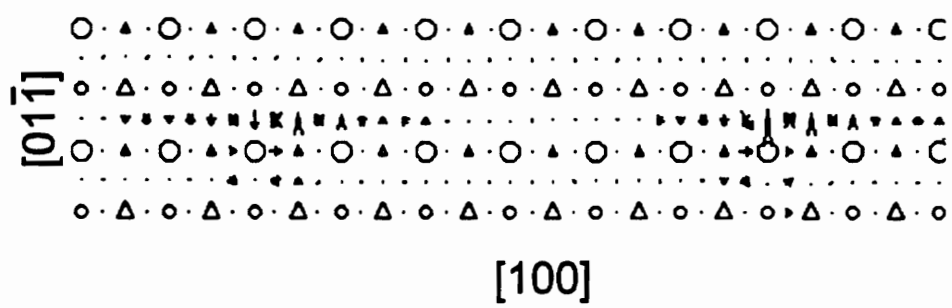


Figure 4.19: The [100](01$\bar{1}$) edge dislocation spontaneously dissociated into two 1/2 $\langle 111 \rangle$ mixed superpartials separated by a 1.8nm long {110} APB; $\triangle = Fe$, $\bigcirc = Al$
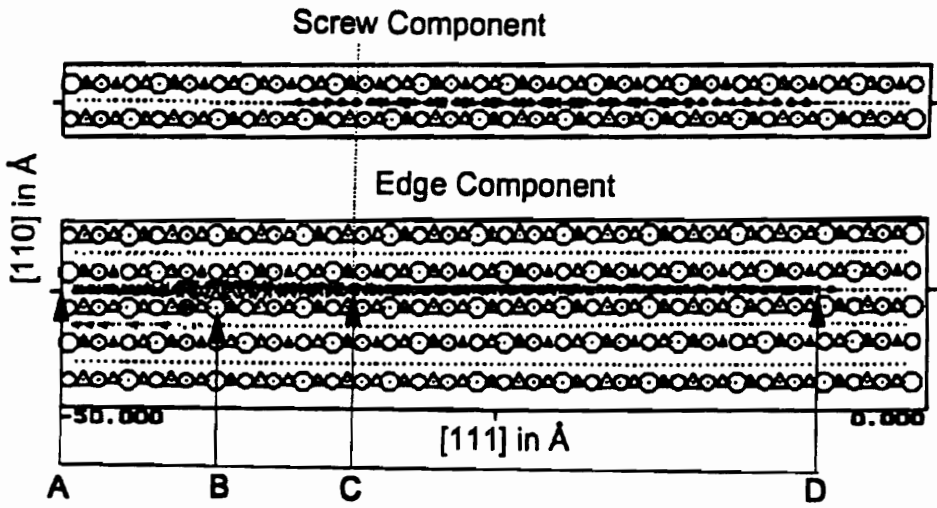
Figure 4.20: Core structures of the $1/2\langle 111 \rangle$ $\{110\}$ edge superpartials; $\triangle = Fe$, $\bigcirc = Al$
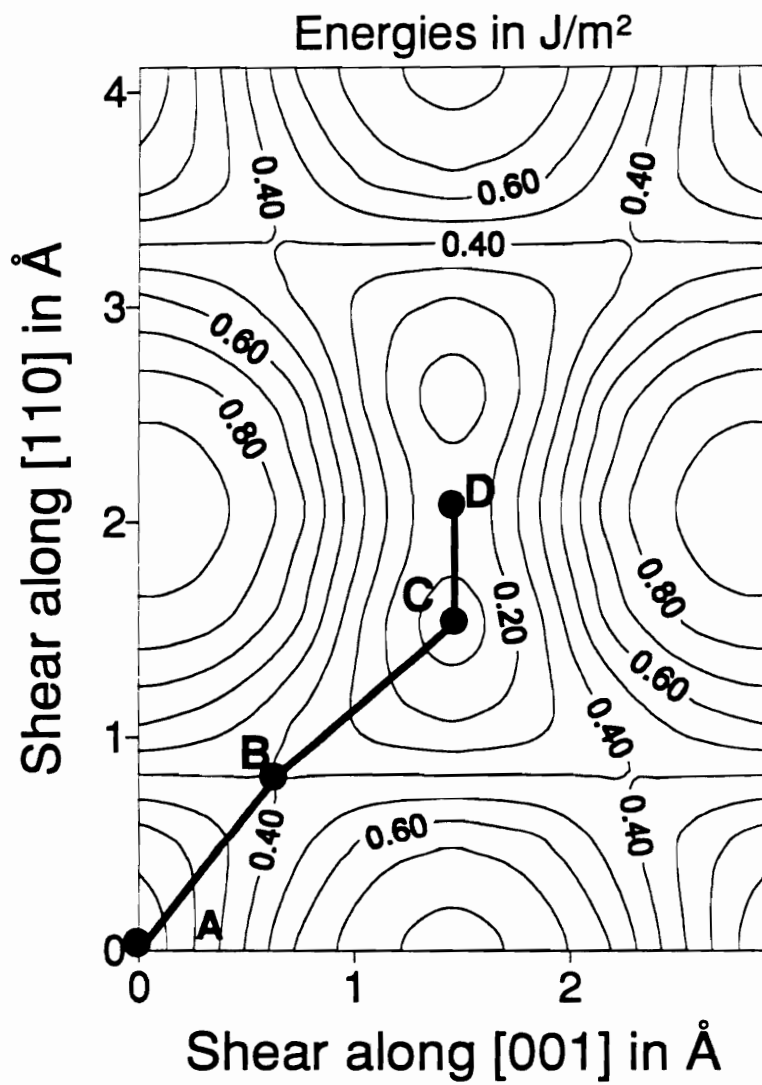
Figure 4.21: Dissociation of the ⟨111⟩ edge dislocation according to the {110} γ-surface in FeAl.
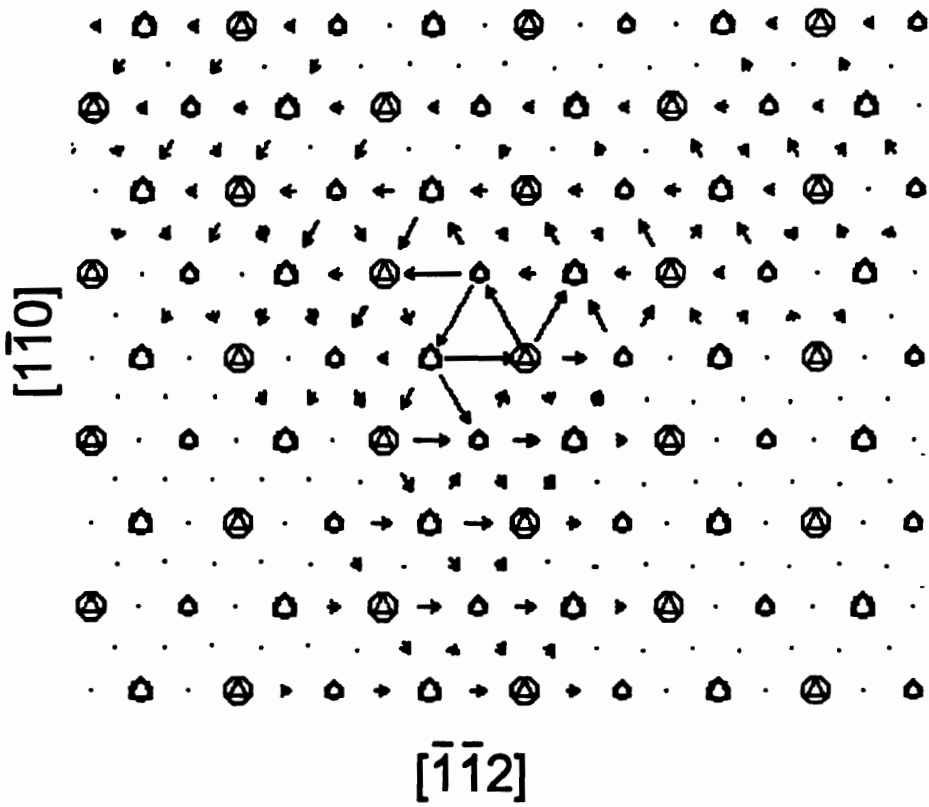
Figure 4.22: Core structure of the complete $\langle 111 \rangle$ screw dislocation; $\triangle = Fe$, $\bigcirc = Al$

98
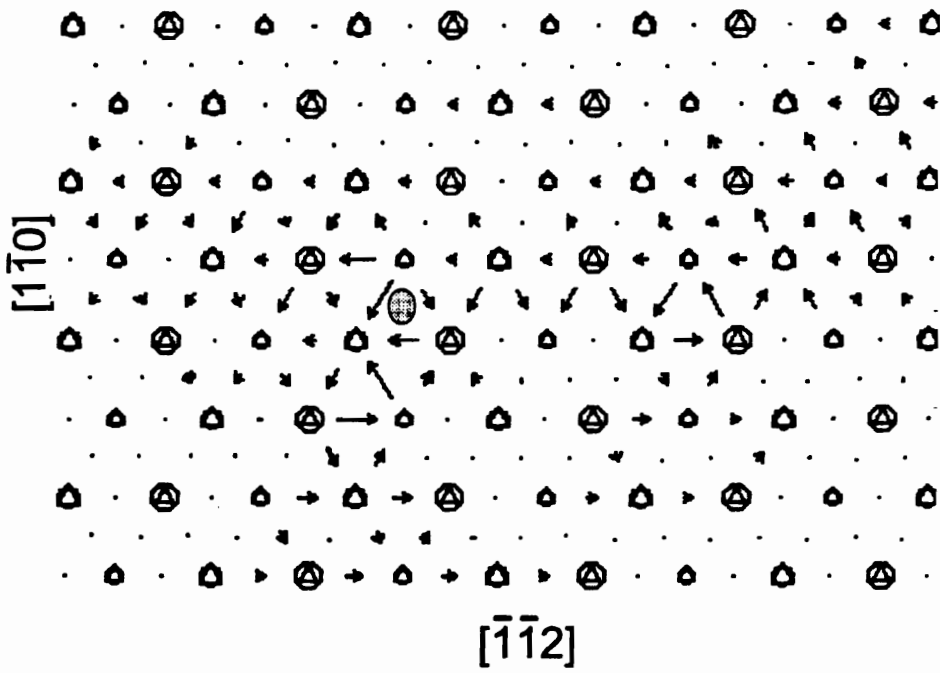
Figure 4.23: Core structures of the 1/2 ⟨111⟩ screw superpartials; $\triangle = Fe$, $\bigcirc = Al$, • = Initial position
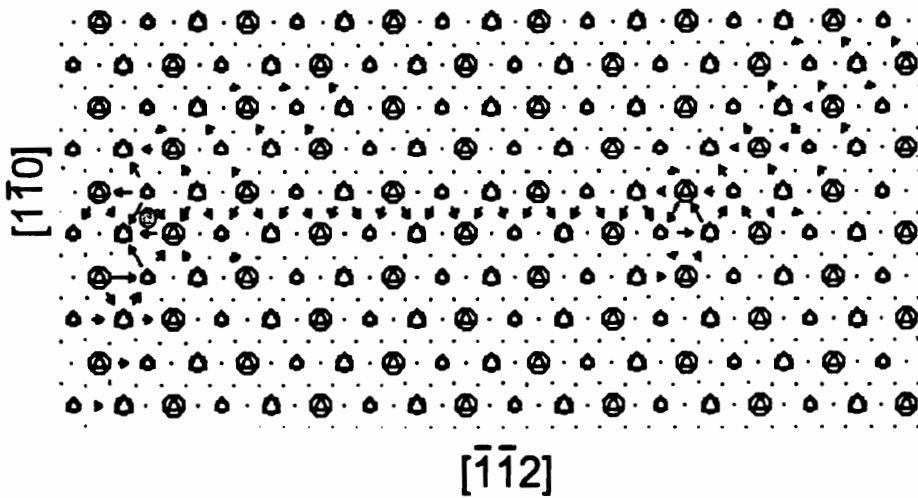


Figure 4.24: Core structures of the 1/2 ⟨111⟩ screw superpartials with an applied stress equal to $0.25 \times 10^{-2}\mu$; $\triangle = Fe$, $\bigcirc = Al$, • = Initial position
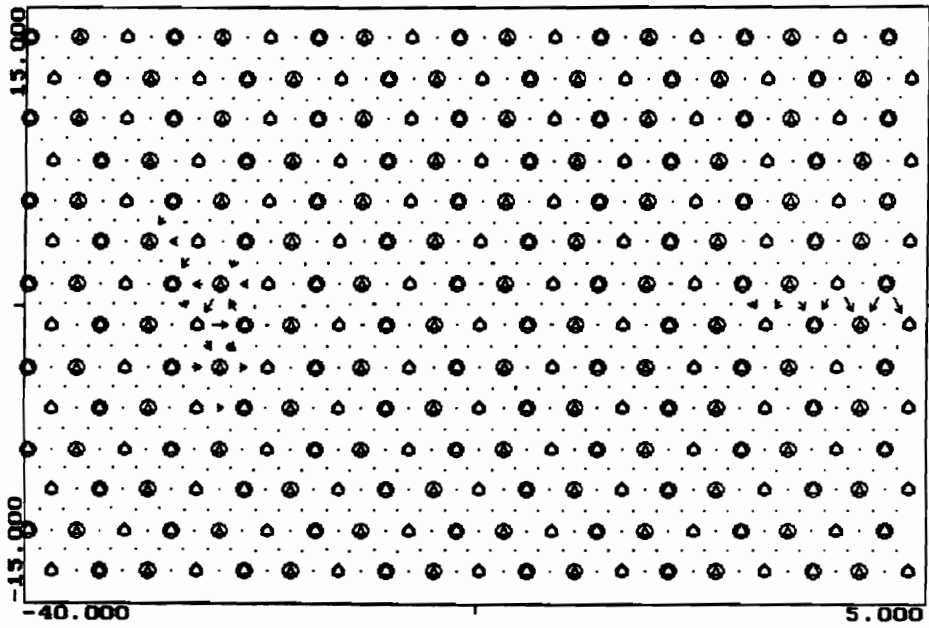
Figure 4.25: Core structures of the 1/2 ⟨111⟩ screw superpartial. The second superpartial is out of the picture, on the right, in the {110} plane containing the APB; △ = Fe, ○ = Al; Units in Å
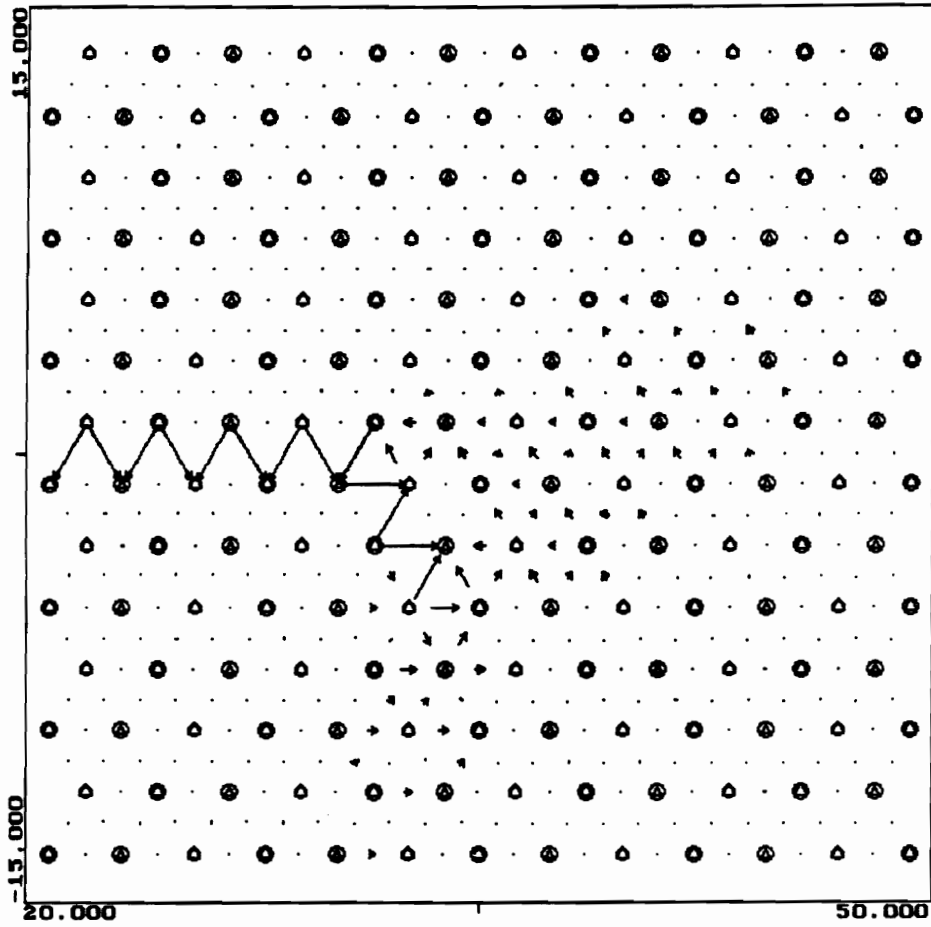
Figure 4.26: Core structures of the 1/2 ⟨111⟩ screw superpartial. The second superpartial is out of the picture on the left; Shear stress along {110} equal to $0.25 \times 10^{-2} \mu$; Long arrows indicate the APB fault; $\triangle = Fe$, $\bigcirc = Al$; Units in Å

101

# Chapter 5

# IN-SITU EXPERIMENTAL OBSERVATIONS
# OF DISLOCATIONS IN B2 NiAl

## 5.1 INTRODUCTION

The macroscopic study of strain as a function of stress and temperature permits to characterize the mechanical properties of a material. On the other hand, microscopic observations in a relaxed sample reveal the structure of the dislocations but the link between their existence and the macroscopic deformation is a difficult exercise. The in-situ observation of a sample while it is deformed in a transmission electron microscope (TEM) is a link between macroscopic and microscopic properties. This technique is not exclusive but is complementary to the understanding of the materials plasticity through the analysis of the dynamic behavior of dislocations.

The first in-situ experiments were conducted on aluminum alloys by Wilsdorf in 1950. The technique has been further developed in Japan, during the seventies and later in France. A more accurate analysis of the results is now possible due to progress in video equipment, conception of specific sample holder as well as accumulated knowledge. The Laboratory of Electronic Optic in Toulouse made significant contributions to in-situ observations. The technique has evolved to a level where it can provide a better qualitative description of the dislocation motion and some quantitative information on the deformation speed and activation energy of the dislocation.

The ability to follow the movement and behavior of the dislocations as they are propagating through the crystal permits the identification of the dislocations participating in the deformation process [80]. It also allows to identification of different glide mechanisms

(simple slip, deviated slip,...), and the nature of the obstacles that control the deformation. More quantitative information can also be deduced such as speed of displacement of the dislocations and the amount of deformation. For some materials, the local stress can also be determined from the curvature of the dislocation lines. Therefore, the dislocation velocity can be related to the value of the local stress.

In-situ observations have already been applied to intermetallics such as $Ni_3Al$ and $Ti_3Al$ with a considerable among of success [81, 82, 83]. These studies have identified different mechanisms of motion such as locking-unlocking, cross slip, or nucleation and propagation of kinks that the dislocation undergoes during displacement. The atomistic simulation of the stable dislocation core structure and its behavior when the dislocation glides through the crystal are complementary to the in situ analysis of the dislocation motion. This chapter reports the results of the in situ observation at room temperature of dislocations in NiAl. These experiments were conducted at the Laboratory of CNRS ,Toulouse, France, which is a leading laboratory for in-situ transmission electron microscopy (TEM) observations. The results were also analyzed according to the core structures and critical stress values obtained for the simulated dislocations.

## 5.2   IN-SITU TEM OBSERVATIONS IN NiAl

### 5.2.1   Experimental Procedure

**Sample Preparation**

The micro-sample used in this study was sliced from a single crystal of stoichiometric NiAl. The single crystal was oriented before being cut such that the loading applied on the sample would be close to the $\langle 100 \rangle$ direction ($10°$ from the exact $\langle 100 \rangle$). Orienting the crystal close to the hard orientation was chosen to try to activate the $\langle 111 \rangle$ slip. In this orientation, the Schmid factor on all cubic planes is close to zero and makes all $\langle 100 \rangle$ slips difficult.

The observation of the dislocation under different contrast conditions was necessary to

determine the orientation of the Burgers vector in the sample. It was also important, for the in situ observations, to be able to follow the dislocations continuously without tilting the sample. While dislocation were gliding through the crystal, tilting the sample would have interrupted the dynamic sequence. For these reasons, the plane of cut was chosen in order to avoid the {100}, {110} or {111} planes. In this condition, the possibility to access different interesting diffraction vectors by tilting the sample was maximized. The exact orientation of the sample studied and specific directions and planes were represented in a stereographic projection (Figure 5.1).

The sample was first cut from the bulk material using electro-abrasion. This sample was cut out in a rectangular shape (5 mm × 2 mm) which a thickness approximately equal to 350 $\mu$m. The sample was then mechanically polished to reduce the thickness to 70 $\mu$m and treated by electro-chemical abrasion. As a result, a small hole (0.1mm) was created in the center of the thin foil. The edge of this hole was thin enough to be transparent to the electron beam. This sample was then glued to a copper grid adapted to transfer the load from the straining device to the thin foil (see Figure 5.2).

**Straining Device**

The primary function of the straining device is to deform the sample inside the microscope. It also controls the temperature of the sample and the angle of tilt between the electron beam and the thin foil. A single tilt straining device was used for this study. The experiments were conducted at room temperature and did not necessitate any temperature control. However, the sample holder has the ability to operate from 50K to 700K. An electric resistance and the circulation of liquid helium or liquid nitrogen through micro-pipes permits the temperature variation of the samples while in the electron microscope (see Figure 5.3).

The traction on the sample was applied with an electric motor. The maximum traction possible with this device was 10 kg. The role of the electric motor was to displace a mobile jaw with respect to a fixed jaw. The speed of the mobile jaw was constant and determined
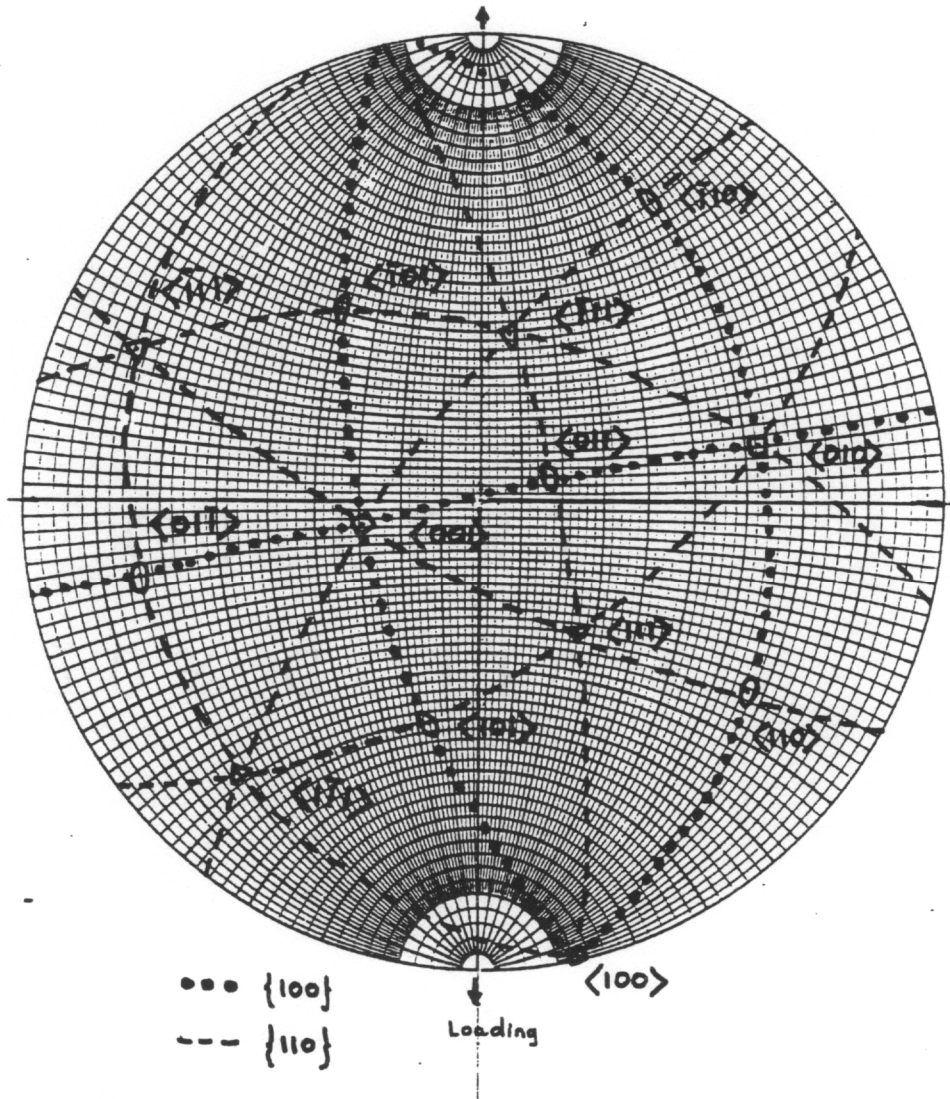
Figure 5.1: Stereographic projection of the orientation of the sample
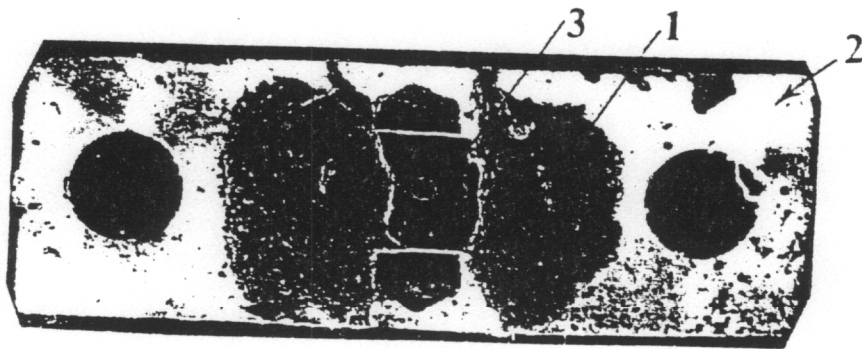
Figure 5.2: Sample glued on the copper grid. 1.Glue 2.Copper grid 3.Sample
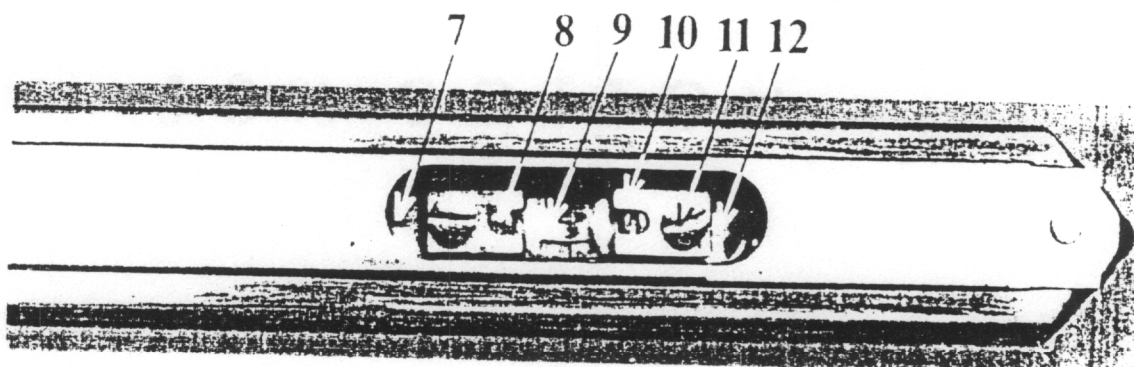
Figure 5.3: Shaft of the straining device introduced in the electron microscope. 7.Fix jaw 8.Fixation of the copper grid 9.Sample 10.Fixation of the copper grid 12.Mobile jaw

by the tension applied to the electric motor. Therefore, the deformation of the sample was at a constant strain rate. The rate of displacement of the jaw was $2.3 \times 10^{-4}$ mm/sec for an applied tension of 5V. However, this rate does not correspond to the real strain rate of the sample. As a matter of fact, only the region around the hole deformed plastically. Since this region is approximately 100 $\mu$m long, the strain rate would be approximately $2 \times 10^{-3} s^{-1}$ which is very high. However, the observations were not conducted at constant strain rate. The traction was applied until the dislocation motion was initiated. Then the displacement of the jaw was stopped to record the motion of the dislocations while the sample was relaxing. The average strain rate was therefore smaller than the value estimated from the constant strain rate.

## Electron Microscopy

In transition electron microscopy, dislocation lines are visible due to the strain field surrounding the dislocation. The angle of the crystallographic planes with the incident electron beam are locally modified due to the strain in the dislocation core. For certain tilt angle between the sample and the initial electron beam, the electrons can travel through a region of perfect crystal structure without being diffracted. However, if some electrons travel in the proximity of the dislocation core, the deviation of the planes from the perfect crystal structure can satisfy Braggs's law for the electron diffraction. On the image formed by the transferred electrons, dislocations appears then as black lines (bright field). If the image is obtained from the diffracted electrons, dislocations appears as white lines on a black background.

The Jeol 200CX transmission electron microscope was used for this study. A tension of 200 kV to accelerate the electrons was used in previous studies of intermetallics and no radiation damage was observed during the exposure time [81, 82, 83]. Therefore the same tension was used in this study. The magnifications were typically between 20,000 and 59,000 with a maximum resolution close to 50Å. This resolution does not allow the identification of dislocation dissociations in NiAl. Observation in a weak beam condition, which would

improve the resolution, was difficult in this material and images in this mode were not very clear. The pictures presented in this study were obtained in bright field or dark field conditions.

The Burgers vectors were always identified using two diffraction vectors that verified the extinction rule, g.b=0. Consequently, the orientation of the Burgers vector was certain. As mentioned previously, there was no time to identify the Burgers vector while following the dislocation motion. To overcome this problem, an initial strain was applied to the sample in order to initiate the dislocation motion. The traction on the sample was then stopped in order to analyze the dislocations involved in this deformation. This procedure allowed the general behavior of the dislocations to be identified and permitted the selection of specific dislocations that were significant to the overall mechanism of deformation. The motion of these dislocations was then followed while the traction on the sample was increased.

The index of the slip planes was easily determined in this study due to the traces left behind the dislocations as they glide through the crystal. These traces were created when the dislocation line encountered the top and bottom surface of the sample. Since these traces had a tendency to disappear with time, the contrast obtained on both surfaces was probably related to fact that the deformation on the surfaces was perturbed by the presence of impurities or an oxidation layer.

The displacement of the dislocations was followed by a video camera. The technique used to capture the image was based on a fluorescent screen. This technique was the same as the one used to take pictures in TEM. The dynamic sequences were observed directly on a video monitor during the observation and were recorded on video tape. The movie could be viewed frame by frame at 25 images per second. The VCR used to view the movie was equipped with a video printer to obtain pictures of the monitor screen. Specific sequences were also transformed to MPEG movies using the equipment of the Multimedia Center at Virginia Tech, so that the movies could be viewed on a computer using the network.

### 5.2.2 Results

Figure 5.4 shows a typical image of the dislocations gliding through the crystal. The Burgers vectors of all dislocations observed were oriented in the $\langle 100 \rangle$ direction. No $\langle 111 \rangle$ dislocations were found even if the orientation of the sample was close to the hard orientation. The density of dislocation was significant and homogeneous, indicative of a ductile behavior.

The most frequently observed slip plane was $\{110\}$ (see Figure 5.4). However, slip along the $\{100\}$ planes was also observed (see Figure 5.5). The $\langle 100 \rangle$ dislocations were zig- zag shaped and were classified by two types namely $\langle 100 \rangle \{010\}$ (see Figure 5.5) and $\langle 100 \rangle \{011\}$ (see Figure 5.6). In Figure 5.5, the trace along the slip plane shows that the dislocation has moved from the $\{101\}$ slip plane to the $\{001\}$ slip plane. Cross slip was very intense as can be seen from the deviation observed along the traces. The dislocation line was composed of segments that were oriented at $45^\circ$ from the Burgers vector. The average orientation of the dislocation line was a screw orientation, parallel to the Burgers vector. A large number of other zig-zag shaped dislocations are also visible on this picture as well as dislocation fragments and loops. On Figure 5.6, the slip plane of the $\langle 100 \rangle$ dislocation was $\{101\}$. The average orientation of the dislocation line was also a screw orientation but the segments were 30-38$^\circ$ from the orientation of the Burgers vector.

The motion of the dislocation was composed of slow and very fast motion. These zig-zag shaped dislocations were associated with the slow displacement. The pure screw orientations of the dislocation line (small region at the angle of the dislocation line) appeared to pin the dislocation. When the strain was increased, the average orientation of the dislocation line moved toward an edge orientation and the dislocation suddenly overcame the pinning and started a very fast motion along a $\{110\}$ slip plane.

Figure 5.7 shows three stages of this dislocation motion. The top picture represents the initial zig-zag dislocation. The picture in the center shows the traces left behind the dislocation during the change of dislocation line orientation. The traces on the top of this
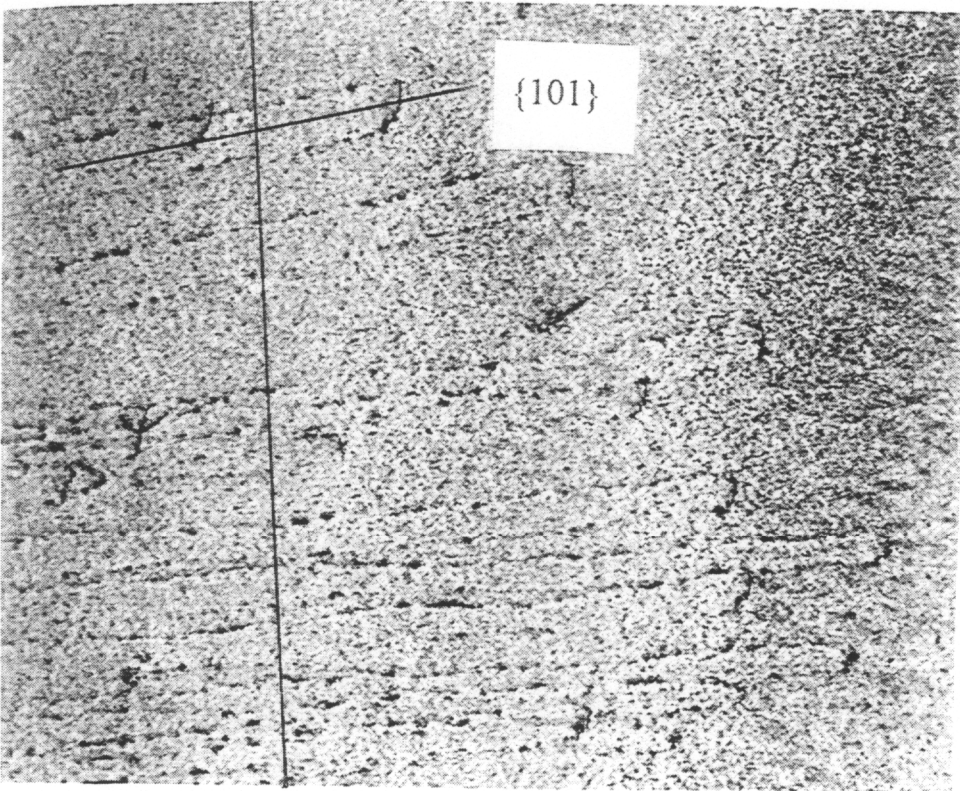
Figure 5.4: ⟨100⟩ dislocations gliding along {110} planes
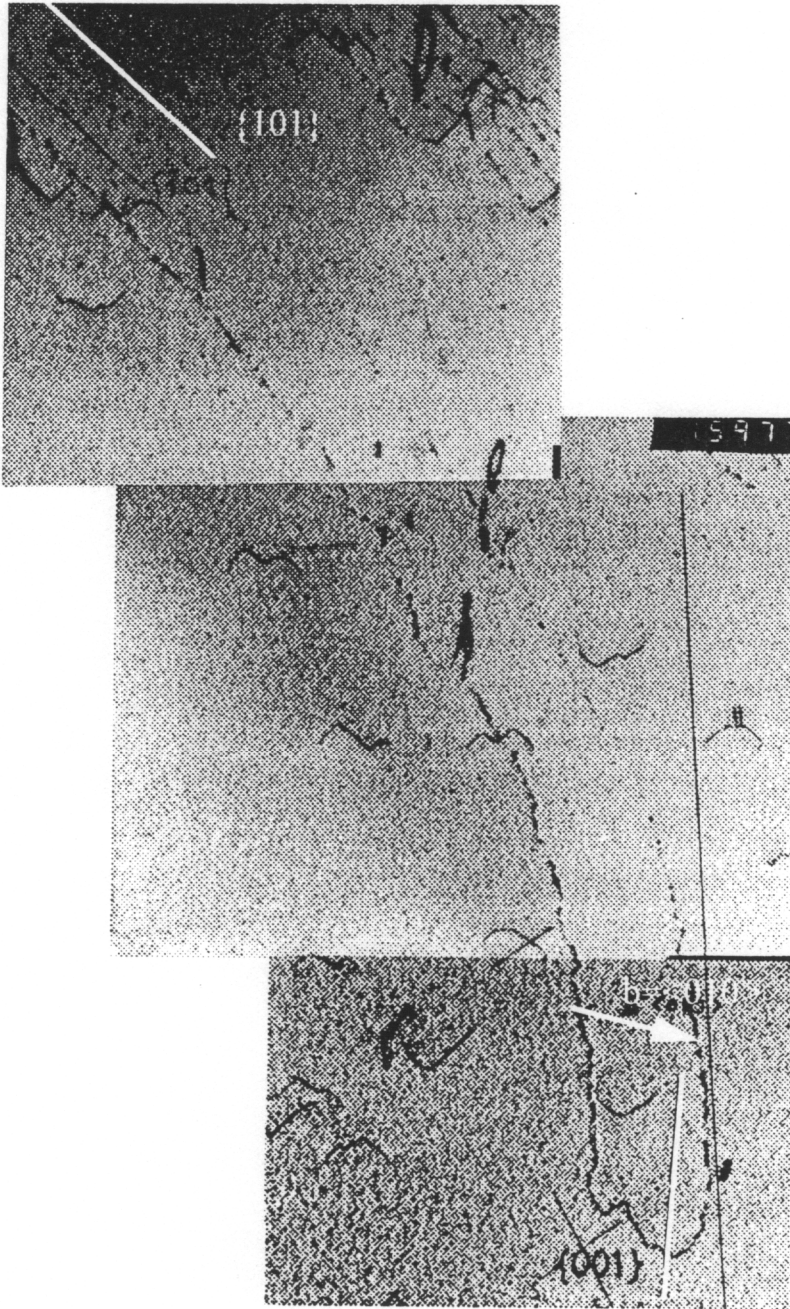
Figure 5.5: $\langle 100 \rangle$ dislocation gliding along a $\{100\}$ plane
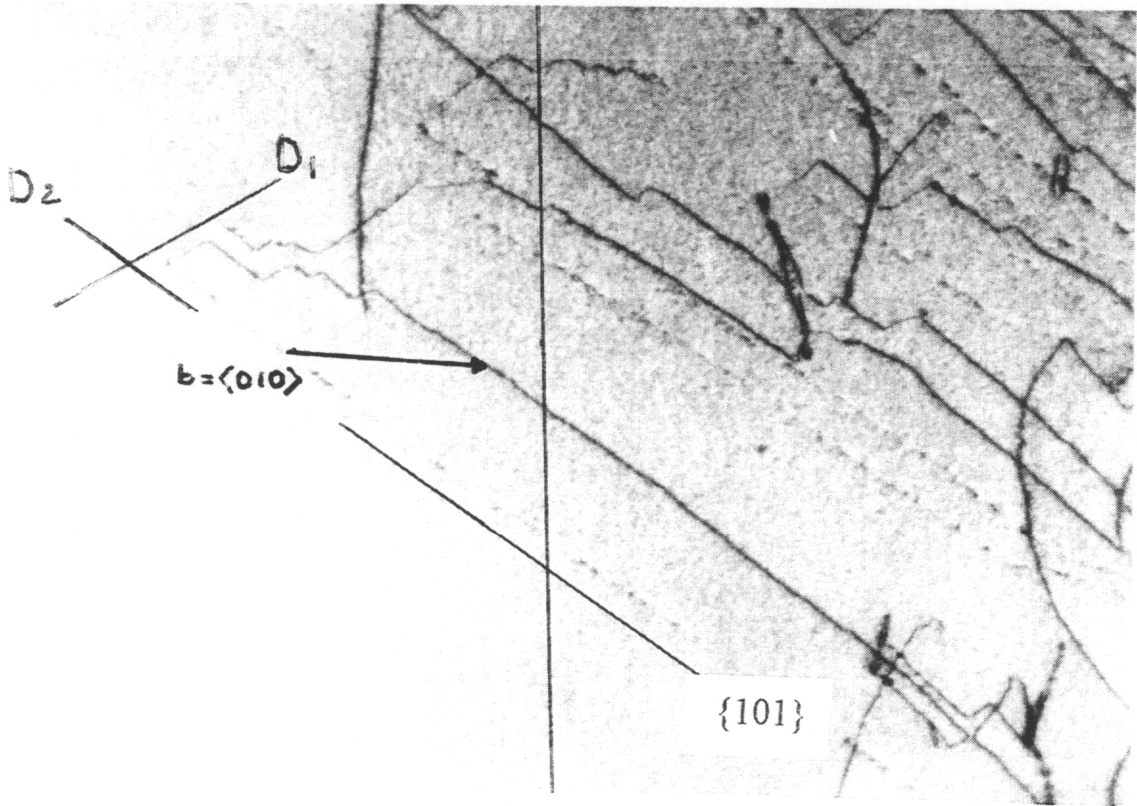
Figure 5.6: ⟨100⟩ dislocation gliding along {110} plane

picture are related to the slow displacement of the zig-zag dislocation. The traces on the bottom of this picture were left by the edge dislocation. This edge dislocation (bottom picture) was found by following its traces toward a region of the crystal where the strain was probably low enough to slow down the dislocation motion. In contrast with the screw dislocation, the edge dislocation did not cross slip during its displacement.

With increasing strain, cracks started to propagate from the region of the edge of the hole where the stress was maximum. An large plastic relaxation was observed around the crack tips. Dislocations were emitted from the crack tips in a continuous flow. This phenomena was clearly observed in the movie but pictures related to this observation were not significant. The flow of dislocations can be seen on the -world wide web- at http://www.mse.vt.edu:80/ ~ chris/. Because of the high strain field around the crack tip, it was not possible to identify the dislocations in the close vicinity of the crack. The dislocation emitted were then followed towards regions of the crystal where their observation was possible. All dislocations emitted were $\langle 100 \rangle$ dislocations.

## 5.3 SIMULATION OF THE $\langle 100 \rangle$ $\{110\}$ SCREW DISLOCATION IN NiAl

### 5.3.1 Simulation of an Other Dimension

The simulated core structure of the screw $\langle 100 \rangle$ dislocation was previously simulated [3]. However, in this simulation of core structure, the orientation of the dislocation line was fixed due to the small size of the simulated block along the dislocation line. The size of the simulation in the direction of the dislocation line was usually equal to the periodicity of the lattice. Periodic boundary conditions were used along this direction. The results were then relevant for a straight dislocation.

After the observation of the zig-zag shaped $\langle 100 \rangle$ dislocation in NiAl, simulation of this dislocation in three dimensions was particularly interesting. The size of the simulation program was significantly increased to enlarge in the direction of the dislocation line. The

114
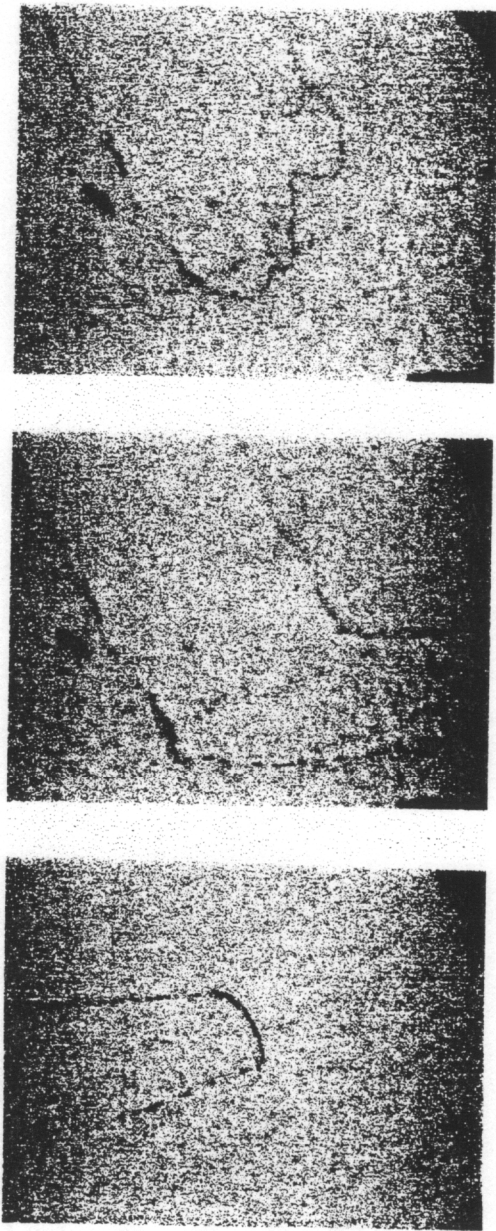
Figure 5.7: Motion of the zig-zag dislocation.

number of atoms used for a simple core structure analysis was around 6,000. The block of atoms was a disk with a thickness of 3 Å and a radius close to 90 Å. To increase the thickness of the block to 60 Å, without changing the radius of the disk, the number of atoms had to be multiplied by 20 (120,000 atoms). The shape of the block was then a cylinder rather than a disk. With such a large number of atoms the computing time increased from a few hours to a few days. As a result, the dislocation line was free for a distance of 60 Å, to relax according to the energy minimization process. Periodic boundary conditions were still applied at the limit of the block in the direction of the dislocation line. Fixed boundary conditions were used around the cylinder.

### 5.3.2 Simulation Results

The dislocation simulated was the $\langle 100 \rangle$ $\{110\}$ screw dislocation. The dislocation line (Z in Figure 4.1) was along the $\langle 100 \rangle$ direction. As expected, the dislocation spontaneously changed to the zig-zag shape as predicted by the experimental observations. Since the deviation of the dislocation line was observed in the $\{110\}$ plane, a plot of the relative displacements in this plane was used to visualize the zig-zag shape of the dislocation (see Figure 5.8).

Two different configurations were obtained as a result of different initial positions of the dislocation. These two configurations are presented on Figures 5.9 and 5.10. In both cases, the angle between the straight segments of dislocation and the $\langle 100 \rangle$ Burgers vector was around $30^O$. This is in good agreement with experimental observations. Due to the size of the simulation and the periodic boundary condition, the length of the segments was around 3 nm in the simulated dislocations in contrast with 1-2 $\mu$m for the dislocations observed in transmission electron microscopy.

Stress was applied to the block of atoms to induce the motion of this dislocation in the $\{110\}$ plane. However, the dislocation line always deviated in the $\{1\bar{1}0\}$ plane perpendicular to the plane of shear. In this position, the dislocation experienced the maximum resistance to motion. When the stress was increased, the angle between the straight seg-

116
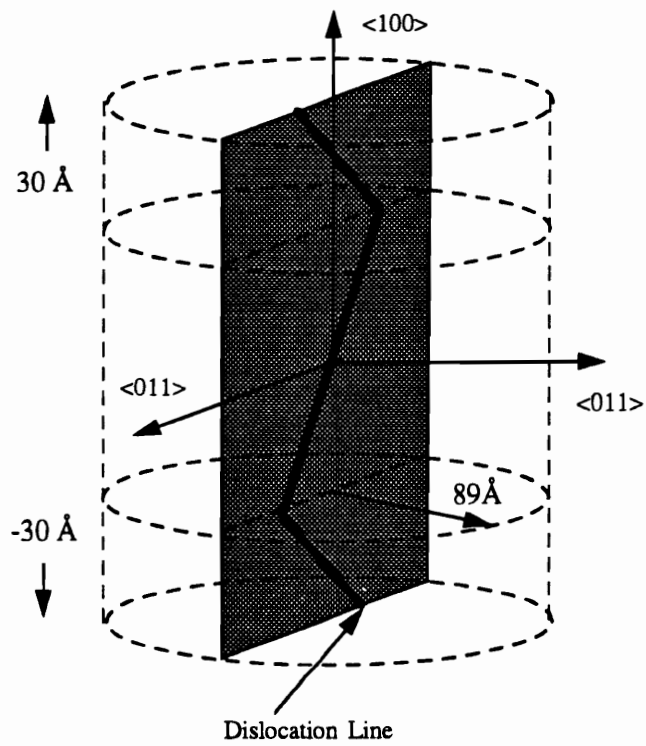
Figure 5.8: Schematic of the zig-zag dislocation simulated in NiAl
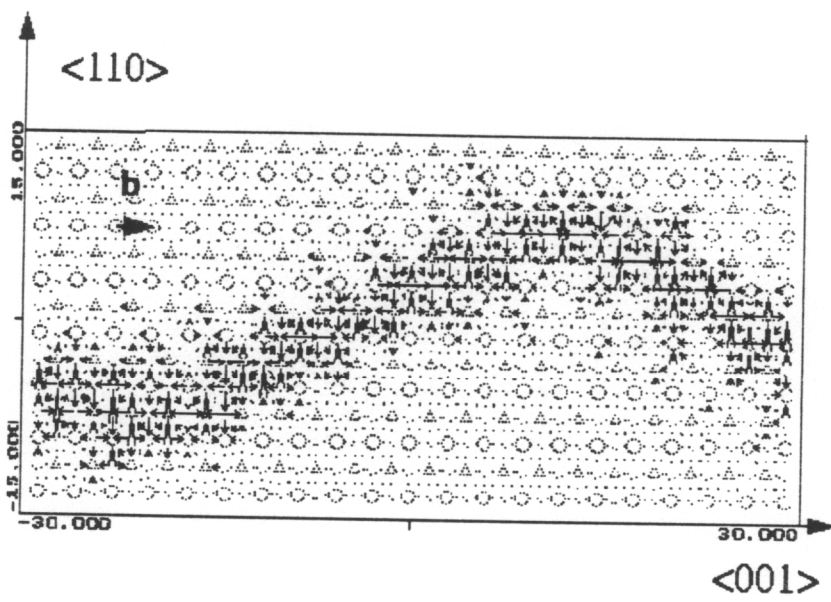
Figure 5.9: Simulated ⟨100⟩ screw dislocation
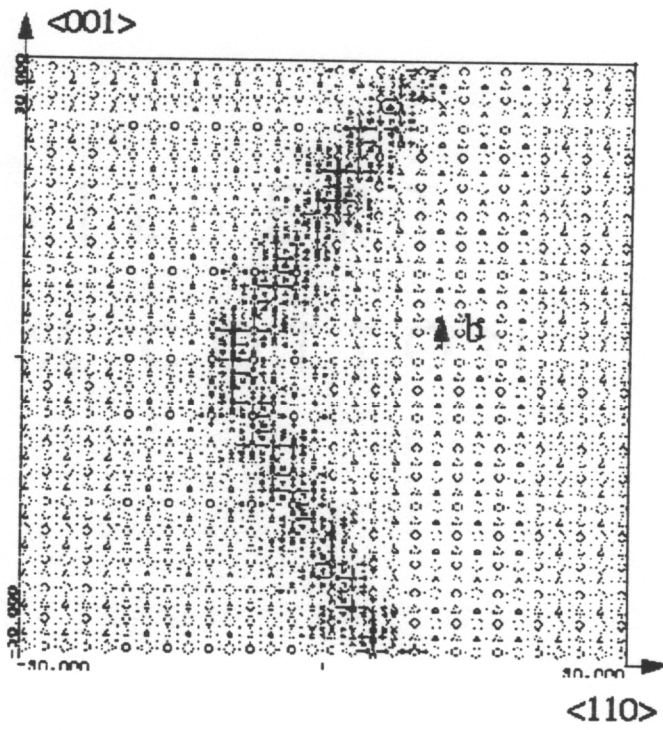
Figure 5.10: Other configuration of the simulated ⟨100⟩ screw dislocation

ments of dislocation line and the Burgers vector were reduced. At stress values close to 400 MPa, the dislocation line was almost straight, but dislocation motion was not achieved (see Figure 5.11). This stress value corresponded to four times the critical stress obtained for the perfectly straight $\langle 100 \rangle$ screw dislocation [3]. The predicted mobility for straight dislocation lines is then more representative of the activation of a kink along a dislocation line with an arbitrary shape.

## 5.4 DISCUSSION

The structures of the dislocations observed in the thin foil were very similar to the ones observed by Morris in a study of NiAl deformed in compression at room temperature [84]. The Burgers vectors and slip planes observed were also in good agreement with all other studies of mechanisms of deformation in NiAl [33]. It is then reasonable to consider that the results reported in this study were not influenced by the small thickness of the thin foil. In accord with our experimental observations of dislocation emission at the tip of the cracks and the general behavior of the dislocations, the sample of NiAl observed in this study presented a ductile behavior.

The screw orientation of the $\langle 100 \rangle$ dislocation was unstable. This is in agreement with the computation of the dislocation energy as a function of the dislocation line orientation. According to the simulation results, the zig-zag configuration lowers the dislocation energy. The exact same configuration as the one experimentally observed was obtained through atomistic simulation. The simulations also suggest that this segmentation of the dislocation line would disappear when shear stress is applied perpendicular to the plane in which the segmentation occurs.

The intense cross slip observed for this average screw dislocation has to be attributed to the pure screw parts of the dislocation. However the pure screw orientation in the zig-zag configuration only happens at the point of intersection of two segments of a dislocation line. This part of the dislocation can be called a tip. These tips must cross slip very easily to
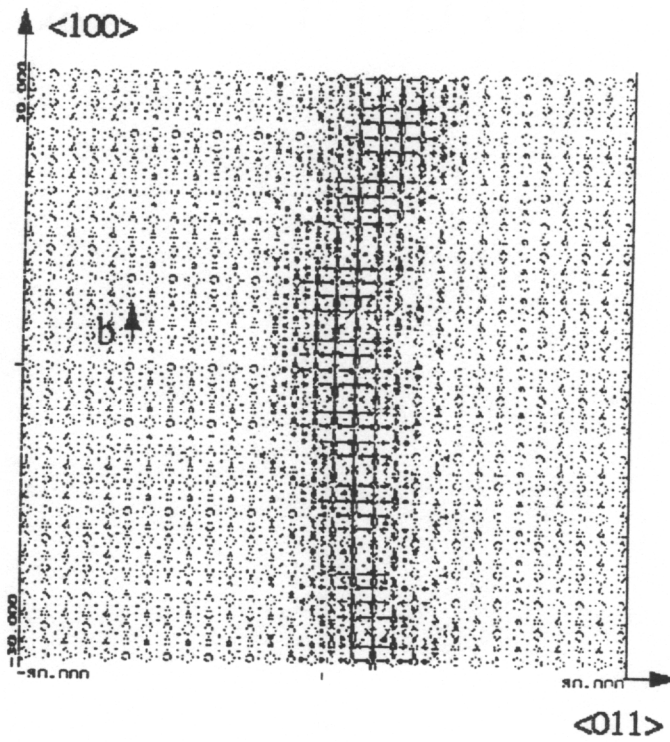
Figure 5.11: ⟨100⟩ screw dislocation under stress

control the cross slip of the dislocation. The core structure simulated for the pure screw dislocation agrees with this theory [48]. This dislocation had a planar core structure along the {110} plane. However, the extension of the core can easily switch from one {110} plane to another, depending on the orientation of the applied stress. This behavior implies that the dislocation can cross slip without resistance from the core structure configuration.

The pinning of the zig-zag dislocation can be explained based on the cross slip of the tips along the dislocation line. A schematic of the mechanism proposed is presented in Figure 5.12. While the dislocation propagates through the crystal, cross slip can occur at one tip of the dislocation line, tip 1 in Figure 5.12. However, this cross slip might not be followed by the other tips. For example, tip 2 can continue to slip along the same plane or cross slip in a plane different than tip 1. As a result, the dislocation splits into two segments moving along different slip planes. While the dislocation continues to propagate in this configuration, an edge dipole is generated at the intersection of the two slip planes. To overcome the pinning, the dislocation has to generate an edge loop. Such loops were observed in the sample as can be seen in Figure 5.5. The other possibility to overcome the pinning is to orient the dislocation to an edge orientation. This mechanism would also agree with the sudden change of line orientation observed after the pinning. Such mechanisms were not observed in the simulated dislocation because the stress applied was not large enough to initiate the dislocation motion. It is also predicted that the thermal energy activation is important in the cross slip mechanism. It is then possible that this mechanism cannot be reproduced with the simulation technique used in this study.

The motion of the edge dislocation was smooth and continuous. Such behavior suggests that the dislocation core was glissile at room temperature. The motion of a sesslile core would be characterized by jumps corresponding to an unstable transformations into a glissile configuration under the applied stress. The non planar core structure simulated for the edge ⟨100⟩ dislocation in NiAl, does not predict a glissile behavior. For this reason, it is believed that thermal activation is important in the mobility of this dislocation. Nevertheless, in-situ observations at lower temperature would be necessary to confirm this hypothesis.
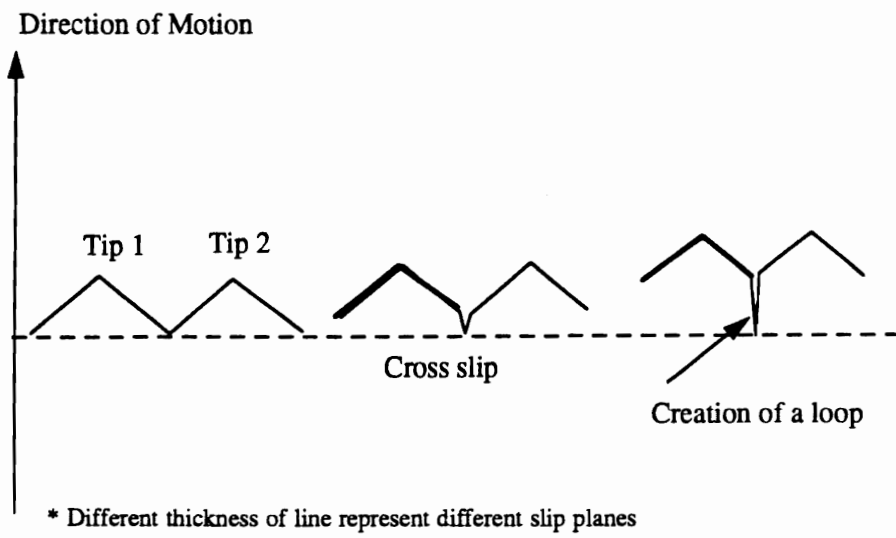
Figure 5.12: Schematic of the pinning mechanism

# Chapter 6

# CONTINUOUS TRANSITION FROM DISLOCATION CORE SPREADING TO DISLOCATION DISSOCIATION IN A SERIES OF B2 COMPOUNDS

## 6.1 ABSTRACT

A comparative study of dislocation core structures was conducted in a series of B2 compounds. The dislocation cores were studied using atomistic computer simulation with embedded atom method potentials. The results show a strong dependence of the core structures on the values of the APB energies of the compounds in the series. The $\langle 100 \rangle$ screw dislocations were found with planar cores in $\{110\}$ planes. For very high APB values, the cores were very compact, as predicted by the Peierls-Nabarro model. As the APB energies decrease, increasingly two dimensional spreading of the cores was observed and ultimately dislocation dissociation into partials. The partials are not exact $1/2\langle 111 \rangle$ but deviate to the point corresponding to the actual minima of the $\gamma$-surfaces for these compounds. The application of the Peierls-Nabarro model and the generalizations of this model to the dislocation cores of B2 alloys is discussed.

## 6.2 INTRODUCTION

Aluminides with the B2 crystal structure present excellent properties for high temperature applications. They have high melting points, resist corrosion at high temperatures and have relatively low density. However, they are too brittle at room temperature to compete with conventional superalloys [2, 18]. In the search for new high temperature structural

materials, a considerable amount of research has been devoted to NiAl. Beside the experimental studies of the mechanisms of deformation, atomistic simulations using embedded atom potentials [4, 40, 3] have been used to investigate shear fault energies, dislocation core structures and slip systems in this intermetallic.

NiAl is part of a series of B2 aluminides (FeAl, NiAl and CoAl) with the same crystal structure and very close lattice parameters but different mechanical behaviors. The room temperature fracture toughness is progressively lower along the series FeAl, NiAl, CoAl [18]. While the primary deformation mode in FeAl at room temperature is the $\langle 111 \rangle$ slip [23, 24, 25], $\langle 100 \rangle$ slip is preferred to the $\langle 111 \rangle$ slip in NiAl [2]. In contrast with FeAl and NiAl, observations of dislocations in CoAl have been limited [17, 75]. Dislocations with $\langle 100 \rangle$ and $\langle 111 \rangle$ Burgers vectors have been observed after deformation at high temperature, but their role in the plastic deformation at room temperature is still unclear.

In order to understand the mechanisms responsible for the brittle behavior of these intermetallics, atomistic simulations of dislocation core structures in FeAl [56], NiAl [3] and CoAl [65] have been conducted in our group using embedded atom method. The interatomic potentials used to simulate the dislocations were developed to reproduce increasing cohesive energy and antiphase boundary (APB) energies from FeAl to CoAl. The unstable stacking fault energies ($\gamma_{us}$) computed along the {110} and {112} planes also followed the trend of increasing APB energies [60]. Because the core structures of the same dislocations simulated in different aluminides had similar shapes, further comparison of the dislocation core required an accurate representation of the strain in the dislocation cores.

The relative displacement map has been used in most studies to represent the atomic displacements in the dislocation cores [85]. Developed in the seventies for the representation of dislocations in b.c.c. metals, the relative displacement map is appropriate for simple dislocation core structures. The cores simulated in intermetallics are more complex than the ones obtained in pure metals. The relative displacement map is still very useful to obtain the magnitude of the Burgers vectors or possible planar faults involved in dislocation dissociations. It is then the first tool to visualize the results of the simulations. However,

only large relative displacements appear on these plots so that the general shape of the core is easily recognized. The low levels of deformations, plotted at the same scale, would generate arrows that are too small to be significant. In order to access the complete information on the strain distribution in the core of the dislocation, two other representation techniques, based respectively on the invariants of the strain tensor and shear in the dislocation core, were used in this study.

A detailed analysis of the core spreadings in the various compounds showed that it was strictly determined by the $\gamma$-surfaces. The $\gamma$-surfaces for these compounds, using the same EAM potentials of the present work, have been determined previously [60]. It was observed that stable planar faults in NiAl, FeAl and CoAl were always deviated from the APB faults in both $\{110\}$ and $\{112\}$ planes. This phenomena may actually be quite general for B2 alloys and independent of the particular potential used since they were found for all the compounds studied. According to the unstable stacking fault energy values, it was predicted that the preferred slip direction was $\langle 111 \rangle$ and the preferred slip plane was $\{110\}$ in all the B2 compounds simulated. It was also observed that stable fault energies and unstable stacking fault energies follow the trend of increasing APB energies along the series FeAl-NiAl-CoAl in both $\{110\}$ and $\{112\}$ planes.

In sections 6.3, the strain invariant representation was used to compare the core structures of the $\langle 100 \rangle$ dislocations in FeAl, NiAl and CoAl. This effort was directed toward a better understanding of the effect of the core structures on the dislocation mobility in the B2 structure. A quantitative analysis of the shear created in the planar core structures is presented in sections 6.4. In FeAl, dissociation of the $\langle 100 \rangle$ dislocation was observed with apparent violation of Frank's rule. This dissociation is discussed in detail in section 6.4 and is related to the core spreadings observed in the other B2 compounds. The application of Peierls-Nabarro models to these dislocations is discussed in section 6.5.

## 6.3 THE $\langle 100 \rangle$ DISLOCATION IN B2 ALUMINIDES

### 6.3.1 Strain Invariants Representation

In continuum mechanic, the state of deformation of a continuous material is characterized by the strain tensor. For small deformation, the strain tensor is defined as:

$$\epsilon_{ij} = \frac{1}{2}(\frac{\partial u_i}{\partial x_j} + \frac{\partial u_j}{\partial x_i})$$

(6.1)

where $u_i$ and $u_j$ are the components of the displacement vector that links the deformed state with the initial state, and $x_i$ and $x_j$ are the cartesian coordinates.

The method to compute the strain tensors as a function of the atomic displacements was developed by Pasianot et al [46]. A strain tensor is obtained for each atom from its displacement with respect to the positions of its close neighbors. The quantities plotted were two invariants of these strain tensors defined as:

$$Y_1 = 2(\epsilon_{xz}^2 + \epsilon_{yz}^2)$$

(6.2)

$$Y_2 = \epsilon_{xx}^2 + \epsilon_{yy}^2 + 2\epsilon_{xy}^2$$

(6.3)

where the dislocation line is along the Z axis in an orthogonal coordinate system. $Y_1$ is the square of the magnitude of the vector $(\epsilon_{xz}, \epsilon_{yz})$ and is an invariant for rotations about Z. This invariant is therefore representative of the screw component of the dislocation and becomes null for a pure edge dislocation. $Y_2$, the norm of the strain matrix, represents the edge component of the dislocation.

The strain invariants were obtained as a function of the initial atom coordinates in the perfect crystal. Since the atomic displacements are periodic in the direction of the dislocation line, the values of the strain invariants only change along the plane perpendicular to the dislocation line. The core structures of the dislocations were then visualized by plotting the strain invariant values as a function of the initial atom coordinates in the plane perpendicular to the dislocation line ($Y_{1 or 2} = f(x,y)$). A continuous surface containing these

127

data points was obtained by interpolation. Contour levels of this surface indicated the region of the core in the same range of strain.

This representation of the dislocation core structures has the advantage to show the low levels of deformation. However, inherent to the definition of the strain invariants, this method do not permit to separate the edge and screw component of a mixed dislocation. The representation of the edge invariant contains strain related to the screw component of the dislocation and reciprocally.

### 6.3.2 Comparative Analysis of the core structures of the $\langle 100 \rangle$ Dislocation

The $\langle 100 \rangle$ dislocations have been simulated in FeAl, NiAl and CoAl. Pure screw, pure edge and mixed orientations of the dislocation line with respect to the Burgers vector were simulated. For the pure edge dislocations, the slip plane defined in the simulation were $\{110\}$ and $\{100\}$. Therefore, the core structures of four different $\langle 100 \rangle$ dislocations have been obtained through atomistic computations. The comparative analysis conducted in this study considers these four different configurations. The strain invariant for the same dislocation simulated in FeAl, NiAl and CoAl are represented on the same figures to allow a simple comparison of the core structures. The critical stress values to initiate the motion of these dislocations are also indicated on the figures. It is important to mention that no significant changes in the shape of the dislocation cores were observed prior to the motion.

The cores of the pure screw dislocations were planar, spread in the $[1\bar{1}0]$ slip plane for all three compounds (see Figure 6.1). The core spreading was more extended in NiAl than in CoAl in accordance with the decreasing shear fault energy computed from CoAl to NiAl. Since FeAl had the lowest APB energy of the series, the dislocation spontaneously dissociated in the $\{110\}$ plane into two superpartials. The critical stress values obtained to move these dislocations along the $\{110\}$ slip plane followed the trend described by the Peierls-Nabarro model for a planar core structure [86]. The critical stress increased for more constricted core structures. This result can also be considered as a consequence of the increasing unstable stacking fault energy along the $\{110\}$ slip plane from FeAl to

128

CoAl. With increasing shear fault energies, the stress opposed to the dislocation spreading increases as well as the energetic barrier to move the dislocation.

The edge $\langle 100 \rangle$ $\{110\}$ dislocation simulated in FeAl (Figure 6.2), also dissociated spontaneously in the $\{110\}$ plane. The core structure of the same dislocation obtained for CoAl was again more constricted than in NiAl. As a general feature, the core structures were less planar and the critical stress values were higher in comparison with the screw dislocations. It was also observed that the critical stresses did not follow the trend of increasing unstable stacking fault from FeAl to CoAl. The dislocation mobility appeared to be very sensitive to the extend of the low level of strain out of the slip plane.

The $\langle 100 \rangle$ $\{010\}$ dislocation is represented on Figure 6.3. The dislocation line was oriented in order to define a slip plane along $\{010\}$. The three aluminides had non-planar core structures spread along two perpendicular $\{110\}$ planes. As suggested by the spreading of the cores, the critical stresses to induce motion of these dislocations were very high. In order to explain these results, the values of $\gamma_{us}$ for the $\langle 100 \rangle$ $\{010\}$ slip system and the geometry of the dislocation core structures should be considered. The maximum shear fault energies, along the $\{010\}$ slip plane and in the $\langle 100 \rangle$ direction, were computed as 0.944 $J/m^2$ in FeAl, 1.239 $J/m^2$ in NiAl and 1.528 $J/m^2$ in CoAl. For FeAl and NiAl, the core structures were very similar and widely extended (2 nm). The effect of the dislocation core structures on the dislocation mobility is then predicted to be the same. The higher value of $\gamma_{us}$ for NiAl was then responsible for the higher critical stress value in comparison with FeAl. Since shear along the $\{010\}$ plane in CoAl was the highest of the series, the critical stress was also expected to be the highest. However, the critical stress simulated in CoAl was lower than in NiAl. These results indicate that the magnitude of the spreading of the core in the $\{110\}$ planes in NiAl and FeAl decreased the mobility of the dislocation.

A mixed orientation of the $\langle 100 \rangle$ dislocation was also considered. The $\langle 100 \rangle$ Burgers vector was at $60°$ from the $\langle 120 \rangle$ direction in the $\{001\}$ plane. The dislocation core structures are represented on Figure 6.4 using the edge invariants. The cores were non-planar and very similar for all three aluminides. However, the spreading of the high and low levels

129
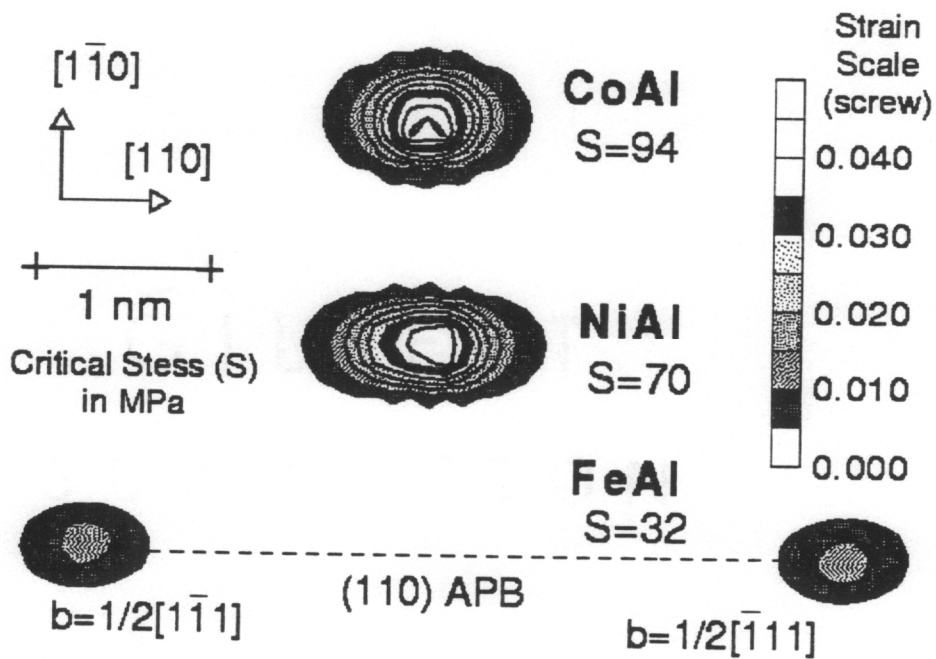
Figure 6.1: Core structure of the ⟨100⟩ {110} screw dislocations and critical stress values for CoAl, NiAl and FeAl
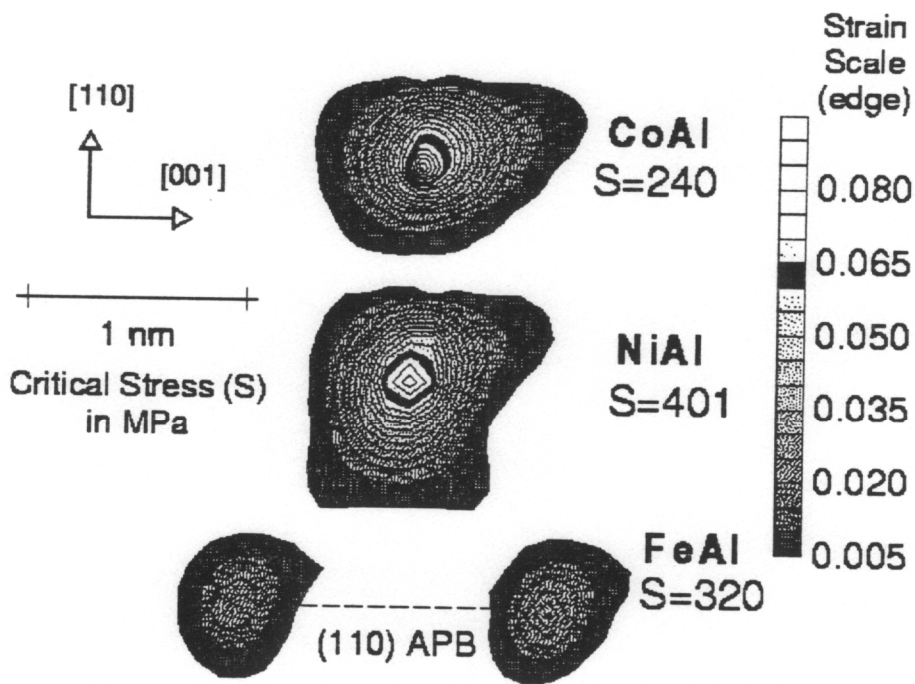
Figure 6.2: Core structure of the ⟨100⟩ {110} edge dislocations and critical stress values for CoAl, NiAl and FeAl
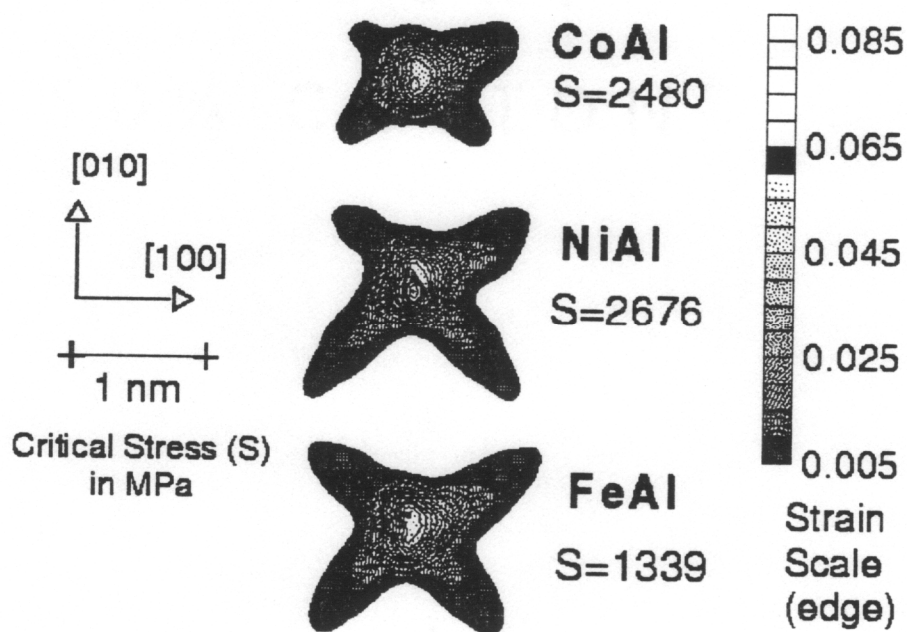
Figure 6.3: Core structure of the $\langle 100 \rangle$ $\{010\}$ edge dislocations and critical stress values for CoAl, NiAl and FeAl

of deformation out of the slip plane increased from CoAl to FeAl. The critical stress values followed the trend of increasing elongation of core spreadings in opposition with decreasing unstable stacking fault energies along the slip plane. Therefore, the mobility of these dislocations appears to be dominated by the dislocation core structure.

As a general result, the relationship between shear fault energy, dislocation core structure and critical stress value was not straightforward. Dislocations with planar core structures, also called glissile configurations, were the easiest to move under an applied shear stress. The mobility of the planar $\langle 100 \rangle$ $\{001\}$ screw dislocations followed the trend of the unstable stacking fault energies along the slip plane. In contrast, the motion of the dislocations with a non-planar core structures was more difficult to activate. For these dislocations, the formation of legs or spreadings in crystallographic planes different from the slip plane reduced the dislocation mobility. The trends observed for the dislocation mobilities in FeAl, NiAl and CoAl were explained in terms of shear fault energies and dislocation core structures. For dislocations with a planar core structure, the mobility of the dislocations was found to increase with the increasing elongation of the core along the slip plane. These results confirm Peierls-Nabarro predictions. For dislocations with a non-planar core structure, our results clearly show that the mobility of the dislocations increases for more constricted core. The dissociation observed in FeAl merits further consideration since the dissociation of $\langle 100 \rangle$ dislocations into two $1/2\langle 111 \rangle$ superpartials is in violation of Frank's rule.

## 6.4  SHEAR ANALYSIS IN THE PLANAR CORE STRUCTURES

### 6.4.1  Shear Displacements in the Planar Cores of the $\langle 001 \rangle$ screw dislocations

The strain in a dislocation with a planar core structure is only localized along the slip plane (see Figure 6.1). The shear created along this plane has been analytically described in the dislocation model proposed by Peierls and Nabarro [86]. In order to compare the simulation results with Peierls-Nabarro model, the shear induced by the dislocation in between
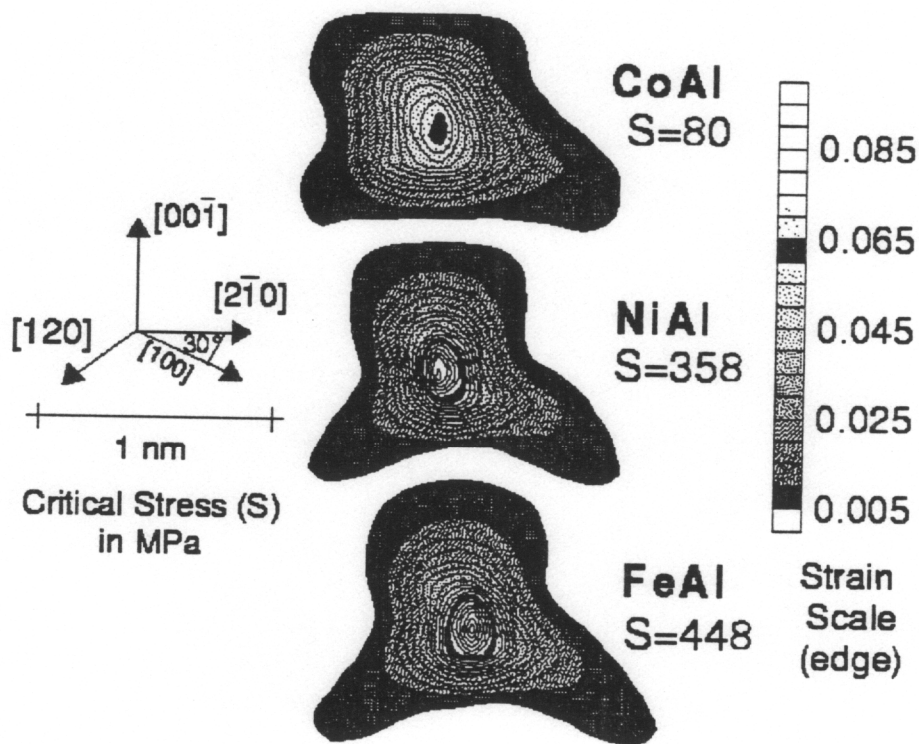
Figure 6.4: Core structure of the ⟨100⟩ {001} screw dislocations and critical stress values for CoAl, NiAl and FeAl

two $[1\bar{1}0]$ planes was computed for the screw $\langle 001 \rangle$ dislocation in the three aluminides.

The two $[1\bar{1}0]$ planes considered for the shear computation were above and below the dislocation. The shear was computed by subtracting the displacement of the atom from the plane above to the displacement of the equivalent atoms from the plane below. The orthogonal reference system used to orient the block of atoms was such that $X=[110]$, $Y=[1\bar{1}0]$ and $Z=[001]$ such that the shear computed from the displacements in the Z direction corresponded to a screw orientation. Similarly, the shear computed from the displacements in the X direction corresponded to an edge orientation. The shear values were always plotted as a function of the initial atom position in the X direction.

Since the Burgers vector was oriented in the Z direction, shear in Z was first considered. The results obtained are presented on Figure 6.5. Going from the negative to positive values of X, the shear in Z varied from zero to the length of the Burgers vectors. The two stages observed in FeAl clearly shows the dissociation of the $\langle 100 \rangle$ dislocation. The slope of these curves at the center of the dislocations (shearZ $= b/2$ for NiAl and CoAl , shearZ $= b/4$ and $3b/4$ for FeAl) increased with decreasing core width.

Shear in the X direction was also plotted as a function of the X coordinates of the atoms in the core structures (see Figure 6.6). This component of the shear, which corresponds to the edge component of the dislocation, tends to zero far away from the dislocation cores since the Burgers vector is parallel to the dislocation line. However, significant values were reached in the center of the dislocation for FeAl and NiAl. This feature indicates that the Burgers vector was deviated from its pure screw orientation in the center of the dislocation. This was expected in FeAl if the dissociation occurs into two $1/2\langle 111 \rangle$ superpartials. The edge components found for the dislocation in NiAl indicates a two dimensional core spreading path, different from the assumptions of the Peierls-Nabarro model.

The distance between the edge and screw components of the two partials in FeAl were measured from the graphs 6.5 and 6.6. The distance measured between the screw component (34Å) was found to be smaller than the distance between the edge component (38Å). This observation agrees with elasticity theory which predicts that the attracting force between

135
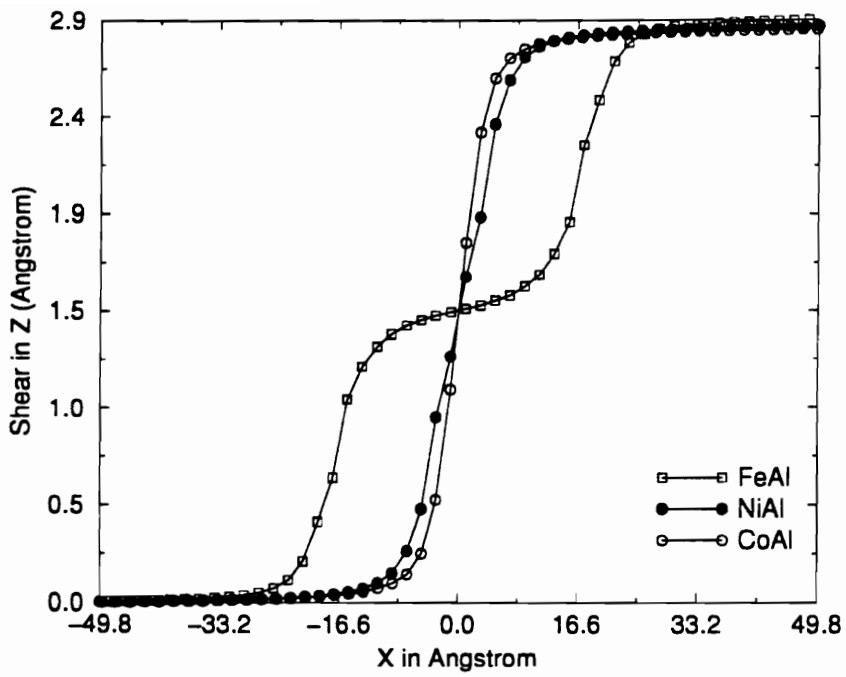
Figure 6.5: Shear in Z as a function of the atom coordinates in X in the $\langle 100 \rangle$ $\{011\}$ screw dislocation in FeAl, NiAl and CoAl

two screw partials is higher than in between two edge partials. The same behavior was found in simulation of Ni₃Al.

### 6.4.2 The γ-b Plots

In order to identify the exact deviation of the Burgers vector in the {110} plane, the shear in Z ([001] direction) was plotted as a function of the shear in X ([110] direction). Since the plane of shear was the {110} plane, this plot has been superposed on top of the {110} γ-surface using the same scale and equivalent axis. In this representation, each circle is representative of an atom and its position is defined by the magnitude of the shear in X and Z at this atom location. These plots were created to understand the relationship between the strain created by the Burgers vector and the profile of the γ surface. In these plots we define the core spreading path. For this reason we named these graphs γ-b plots.

The Burgers vector of the screw dislocation in CoAl was not deviated from the ⟨001⟩ direction(Figure 6.7). The shear in the dislocation core overcomes the unstable stacking fault energy along the ⟨001⟩ direction. This result should be considered as a normal behavior for a planar core structure. In contrast, shear in the core of the same dislocation in NiAl does not follow the direction of the Burgers vector (Figure 6.8). The path followed by the atoms corresponds to lower shear fault energies by avoiding the high energy of the 1/2 ⟨001⟩ unstable stacking fault. The maximum shear energy experienced by the core is then related to the unstable stacking fault along the ⟨111⟩ direction.

The γ-b plot for FeAl clearly shows the dissociation of the ⟨001⟩ Burgers vector into two dislocations close to 1/2⟨111⟩ (see Figure 6.9). The closest equation possible for this dissociation is as follows:

$$\langle 001 \rangle screw = 1/8\langle 334 \rangle + SPF\{110\} + 1/8\langle \bar{3}\bar{3}4 \rangle \tag{6.4}$$

where SPF {110} stands for stable planar fault in the {110} plane which is observed to be deviated from the APB in the B2 compounds.

This dissociation of the ⟨100⟩ dislocation into two 1/2⟨111⟩ superpartials has been sug-
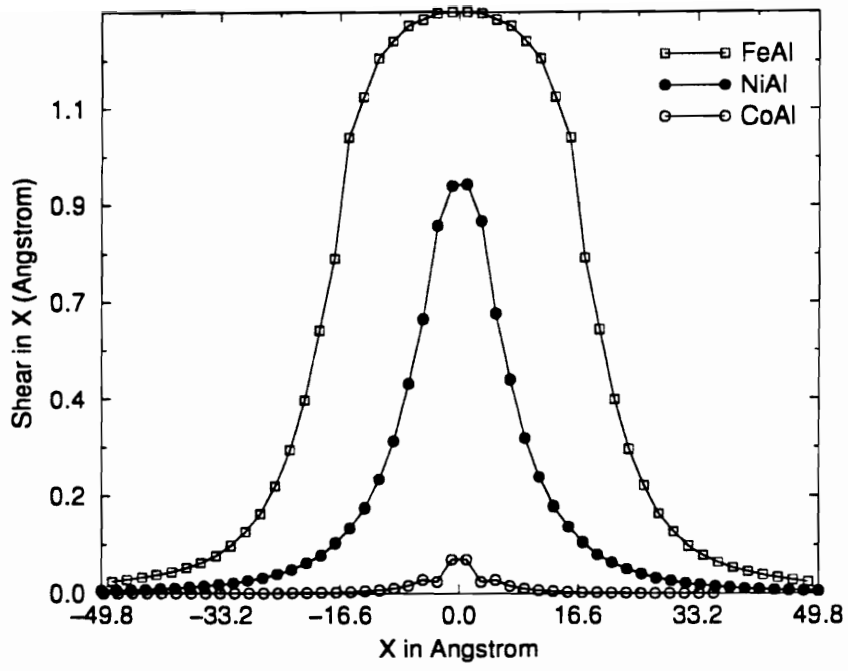
Figure 6.6: Shear in X as a function of the atom coordinates in X in the $\langle 100 \rangle$ $\{011\}$ screw dislocation in FeAl, NiAl and CoAl

138

**Energies in J/m²**
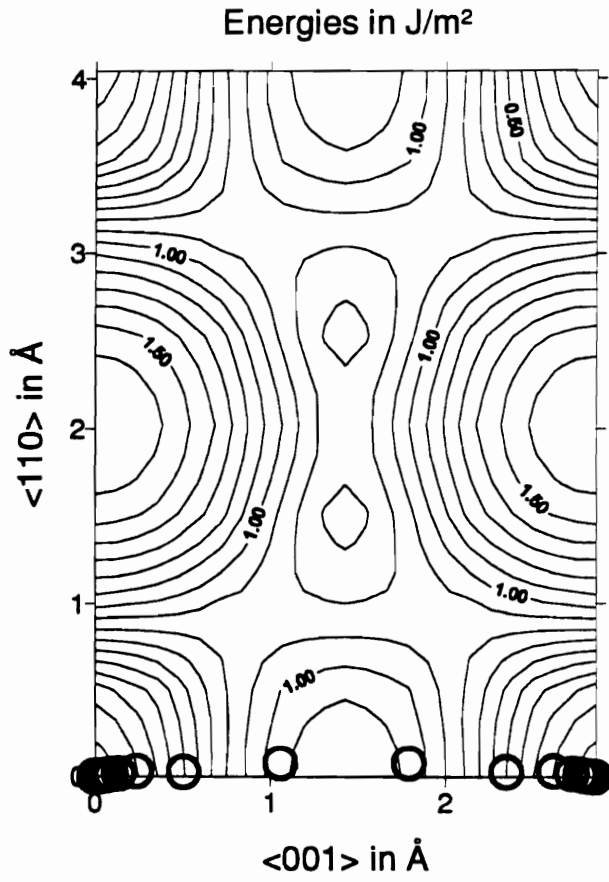
Figure 6.7: $\gamma$-b plot of shear in the core of the $\langle 001 \rangle$ screw dislocation and $\{110\}\gamma$-surface in CoAl
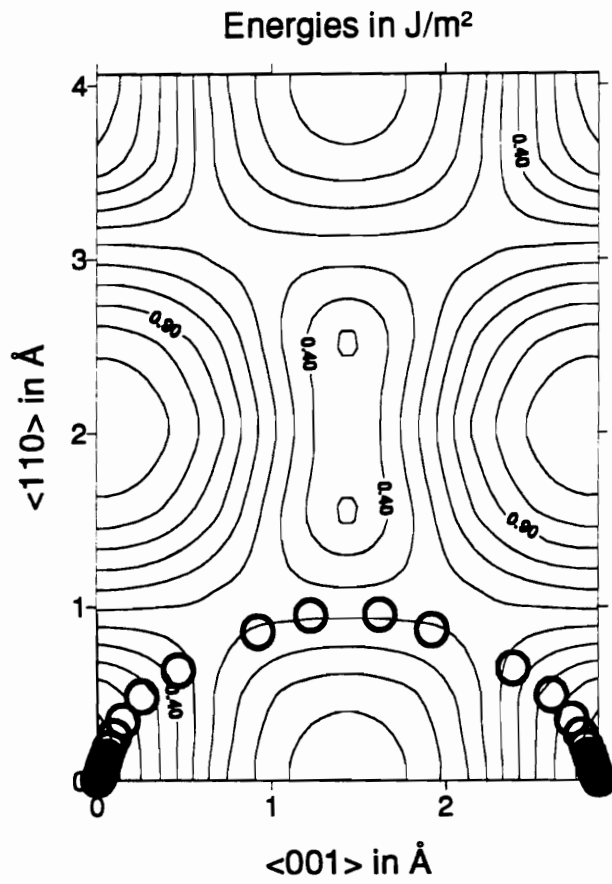
Figure 6.8: $\gamma$-b plot of shear in the core of the $\langle 001 \rangle$ screw dislocation and $\{110\}\gamma$-surface in NiAl

gested in previous experimental studies [78, 79] but cannot be explained with elasticity theory (violation of Frank's rule). The criteria of dislocation dissociation assumes that the dislocation energies are proportional to $b^2$. If the dislocation dissociates into two $1/8\langle 334 \rangle$ dislocations, the energy of the complete dislocation is still lower than to the sum of the energies of the two superpartials. The limit for Frank's rule is given by:

$$\langle 001 \rangle screw = 1/2 \langle \frac{\sqrt{2}}{2} \frac{\sqrt{2}}{2} 1 \rangle + SPF\{110\} + 1/2 \langle \frac{\bar{\sqrt{2}}}{2} \frac{\bar{\sqrt{2}}}{2} 1 \rangle \qquad (6.5)$$

which corresponds to an angle of $45^o$ between the $\langle 001 \rangle$ direction and the Burgers vectors of the partials. If the dissociation of the $\langle 001 \rangle$ dislocation generates an stable planar fault as in Equation 6.4, the dissociation is very close to Frank's rule limit. For more accuracy, the length of the Burgers vectors for the partials were measured on Figure 6.9. The two Burgers vectors were 2Å long and were closer to $1/6\langle 223 \rangle$ than $1/8\langle 334 \rangle$. In accordance with Figure 6.5, the partials were not entirely relaxed to the true minimum planar fault energy. As a result, the sum of the square of the two $1/6\langle 223 \rangle$ Burgers vectors (8.2) is inferior to the square of the complete $\langle 001 \rangle$ Burgers vector (8.4). According to Frank's rule, the dissociation is energetically favorable in this case. This finding can justify the prediction of this dissociation based on experimental observations [78, 79].

These $\gamma$-b plots show the strong influence of the $\gamma$- surface features on the dislocation core structure. The $\langle 001 \rangle$ screw dislocation in NiAl can be considered as a complete dislocation since no stable planar fault was created. However, because the core was spread in two dimension, the value of the unstable stacking fault that the dislocation experienced was along the $\langle 111 \rangle$ direction as if the dislocation was dissociated into two $1/2 \langle 111 \rangle$ superpartials. This phenomena corresponds to a continuous transition from dislocation core spreading to dislocation dissociation. In order to quantify the degree of dissociation of the $\langle 100 \rangle$ dislocation, the percentage of dissociation was computed by comparing the position of the stable planar fault in the $\langle 110 \rangle$ direction ($1/8\langle 330 \rangle$) to the maximum extend of the core in the same direction (see 6.6). FeAl was found to be 85% dissociated, NiAl 62% dissociated and CoAl 4% dissociated.

141
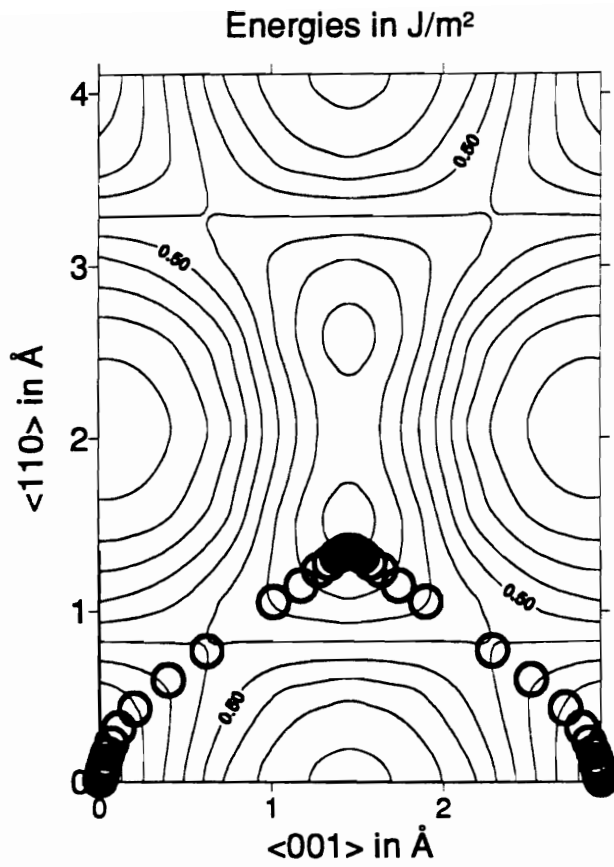
Figure 6.9: $\gamma$-b plot of shear in the core of the $\langle 001 \rangle$ screw dislocation and $\{110\}\gamma$-surface in FeAl

### 6.4.3 Core width of the ⟨001⟩ Screw Dislocation

In the Peierls-Nabarro model the core width of the screw dislocation is equal to the spacing between two {110} planes. This model gives similar core width for compounds with similar lattice parameters. For example, the core width in FeAl, NiAl and CoAl would be respectively 2.023, 2.033 and 2.054 Å for the ⟨001⟩ screw dislocation.

A different description of the core width was proposed by Rice [71] in a study related to dislocation emission from crack tip. In this study, the shear stress along the plane of shear and in the direction of the Burgers vector was described by the Frenkel sinusoid. The maximum of this function was related to the value of $\gamma_{us}$. The extend of the core in Rice analysis was given by the value of the parameter R which is proportional to the value of the unstable stacking fault, $\gamma_{us}$. The expression for R was as follows:

$$R = 2.48 \frac{\mu b^2}{2\pi^2(1-\nu)\gamma_{us}} \tag{6.6}$$

where b is the Burgers vector, $\mu$ is the shear modulus, $\nu$ is the Poisson's ratio and $\gamma_{us}$ is the unstable stacking fault energy. The use of $\gamma_{us}$ in this equation describes more specifically the restoring forces that limit the atomic displacements along the plane of shear. The $\gamma_{us}$ value is specific to the slip system considered and is obtained through atomistic computations. The core width defined by Rice was equal to 2/3 R in his study related to dislocation emission. This author also indicates that if the value of R is proportional to the core width, a correcting factor should be included for comparison with Peierls dislocation model. However, the correspondence between the two models is linear.

The values of R were computed for FeAl, NiAl and CoAl according to two assumptions. First it was considered that the ⟨001⟩ dislocation in CoAl was a complete dislocations and the value of $\gamma_{us}$ in the ⟨001⟩ direction was used. The other assumption was to consider that the ⟨001⟩ dislocation in FeAl was dissociated into two 1/6⟨223⟩ superpartials. The value of $\gamma_{us}$ in the ⟨111⟩ direction was used and the core width obtained was projected on ⟨001⟩, direction of the Burgers vector. This projection was necessary to compare the extend of the core structures independently of the deviation of the Burgers vector. For NiAl,

both hypothesis were tested. The values of the parameter R, presented in Table 6.1, were computed using the values of shear modulus computed for the EAM potentials describing the three B2 compounds.

The width of the cores simulated were also measured in Figure 6.5, following the Peierls-Nabarro definition. The core width was defined as the region of the core where the shear in the direction of the Burgers vector was between the values of -b/4 and b/4. The dislocation was assumed to be complete for CoAl and dissociated into two superpartials for FeAl. Both complete and dissociated configurations were considered in NiAl and two core widths were measured according to these two hypothesis. Since the distance in between two atoms in the $\langle 110 \rangle$ direction was 2 Å, the exact measurement of shear in the core was only possible every 2 Å. Therefore, the core widths were estimated according to the interpolated curves in Figure 6.6. The results of these measurements are presented in Table 6.1 in comparison with the computed values.

The core widths measured were plotted as a function of R (see Figure 6.10) to identify a correlation factor. The core widths of the complete $\langle 001 \rangle$ dislocation in CoAl and dissociated dislocations in NiAl and FeAl were linearly related to the values of R. The average correlating factor was equal to 2.25. The core width obtained for the complete $\langle 001 \rangle$ dislocation in NiAl does not follow this linear relationship. This result can be explained if the dislocation is considered to be closely dissociated. The measurement of the core width as a complete dislocation then includes the distance between the two partials. On this basis it is believed that two superpartials should be considered to measure the core width of the $\langle 001 \rangle$ dislocation in NiAl.

## 6.5   DISCUSSION

This study addressed the problem of representation of complex dislocation core structures simulated in B2 aluminides. The use of strain invariants permitted to identify the change in the shapes of the core structures of the $\langle 100 \rangle$ dislocations simulated in FeAl, NiAl
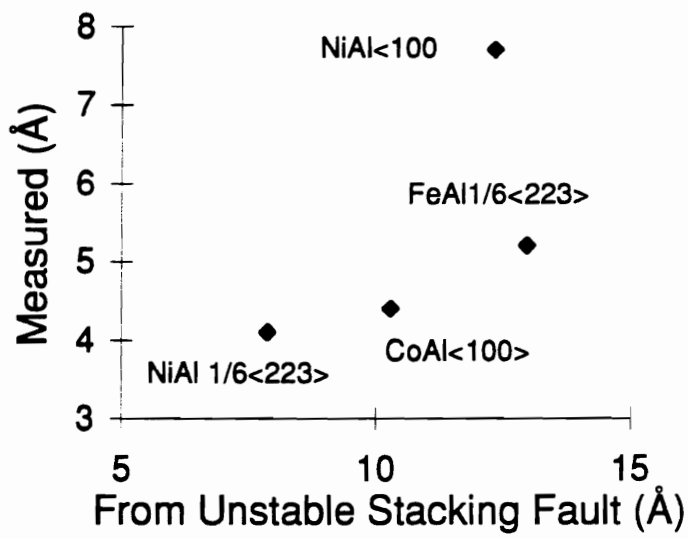
Figure 6.10: Core width measured as a function of the value of R

and CoAl. The effect of the core structure on the dislocation mobility was analyzed considering two other parameters obtained through atomistic simulations. These two parameters were the critical shear stress to move the dislocation and the unstable stacking fault energy in the direction of the Burgers vector along the slip plane.

The mobility of the dislocations was found to increase for increasing elongation of the core along the slip plane. In contrast, increasing core spreading in planes other than the slip plane decreased the dislocation mobility. This comparative study was conducted using the representation of the strain invariants. This technique defines the contour of the dislocation cores more accurately than the relative displacement map. Comparison of the non-planar cores also shows that the width of the core along the slip plane tends to decrease with increasing spreading of the core out of the slip plane. This phenomena corresponds to a transfer of the strain from the slip plane to other planes. The other variable considered in these comparisons was the value of the unstable stacking fault energy, specific to the material and slip system considered. Decreasing dislocation mobility was observed in B2 aluminides with increasing unstable stacking fault energies.

The analysis of shear in the planar core structures revealed some important features in the comparison of the $\langle 100 \rangle$ screw dislocation in three B2 alumindes. The dislocation simulated in CoAl created a shear mainly oriented in the direction of the Burgers vector. This dislocation is then similar to the Peierls-Nabarro dislocation model. The theoretical prediction of the Peierls stress computed for the core with of this dislocation is equal to 15 MPa. This stress value is in good agreement with the simulated stress value (95 MPa).

In contrast with CoAl, the planar dislocations in NiAl and FeAl do not follow Peierls-Nabarro model. The shear in the dislocation cores was along the slip plane but not exclusively in the direction of the Burgers vector. The core widths were then more accurately described by the values of the unstable stacking fault energies in the $\langle 111 \rangle$ direction considering two $1/2\langle 111 \rangle$ partial dislocations. While the $\langle 100 \rangle$ dislocation in FeAl was dissociated into two superpartials, the shear in the core of the $\langle 100 \rangle$ dislocation in NiAl indicates an intermediate configuration between the dissociated and non-dissociated dislocation. More

146

sophisticated model have been proposed to predict the dissociation of the $1/2\langle 101 \rangle$ dislocation into two Shockley partial dislocations in an FCC lattice [87]. However, this model does not predict a continuous transition in the dissociation mechanism.

## 6.6 CONCLUSIONS

The mobility of the $\langle 100 \rangle$ dislocations in FeAl, NiAl and CoAl were compared. The results show a strong dependence of the dislocation mobility on the low levels of deformation of the non-planar dislocation cores. Planar cores in the $\{110\}$ plane were obtained for the $\langle 100 \rangle$ screw dislocations in NiAl, CoAl and FeAl. Using the strain invariant representation, dissociation of this dislocation into two $1/6\langle 223 \rangle$ partials was only identified in FeAl. However, the analysis of the shear in these planar cores indicates a continuous transition from dissociated to complete dislocation which follows the trend of increasing APB energies from FeAl to CoAl. This continuous transition was found to be related to the fact that the core spreading path tends to avoid the positions of high shear fault energy.

Table 6.1: Values of the parameter R and measured values of the core width in the $\langle 110 \rangle$ direction for the cores of the $\langle 001 \rangle$ screw dislocations in FeAl, NiAl and CoAl. b is the length of the Burgers vector considered

| Compounds | R (Å) | Measured Core Width (Å) |
|---|---|---|
| CoAl b=$\langle 001 \rangle$ | 10.30 | 4.4 |
| NiAl b=$\langle 001 \rangle$ | 12.34 | 7.7 |
| NiAl b=1/6$\langle 223 \rangle$ | 7.86 | 4.1 |
| FeAl b=1/6$\langle 223 \rangle$ | 12.97 | 5.2 |

# Chapter 7

# INTERATOMIC POTENTIALS AND DISLOCATION SIMULATION FOR TERNARY B2 NI-35Al-12Fe ALLOY

## 7.1 ABSTRACT

Interatomic potentials of the embedded atom type were developed for the Fe-Ni. This potential was obtained by empirical fitting to the properties of FCC FeNi. The other potentials required for this fitting procedure were obtained from previous reports. The potentials predict the stability of the FCC disordered equiatomic phase with respect to the $L1_0$ and BCC phases. This potential permitted simulation the B2 ternary alloy Ni-35Al-12Fe which is known to have higher ductility than B2 NiAl. The $\langle 100 \rangle$ screw dislocation was simulated in Ni-35Al-12Fe for comparison with the previously reported results on the same dislocation in NiAl and FeAl. This study shows that the behavior of the $\langle 100 \rangle$ screw dislocation in the ternary alloy can be considered as an intermediate between NiAl and FeAl. The dislocation always dissociates into two superpartials along a $\{110\}$ plane as observed in FeAl. However, the distance between these superpartials depends on the actual distribution of the atoms in the simulation. The separation distances computed ranges from a complete dissociation, as in FeAl, to a very close dissociated configuration as in NiAl. The superpartials appeared to be highly mobile along the $\{110\}$ plane in order to reach energetically stable regions within the crystal.

## 7.2 INTRODUCTION

The intermetallic NiAl with the B2 structure exhibits excellent potential as a structural material for applications at high temperature [2, 15]. Unfortunately, NiAl is too brittle at room temperature to compete with the conventional alloys. Therefore, the mechanisms of deformation of this intermetallic have been studied intensely. Studies in single crystals revealed that the stress necessary to activate the slip in the ⟨100⟩ direction is far lower than the stress needed to activate the ⟨111⟩ slip. As a result, the deformation at room temperature is controlled by the ⟨100⟩ slip. Therefore, the lack of room temperature ductility of polycrystalline NiAl is believed to be related to the reduced number of independent slip systems in NiAl. Although a minimum of five slip system is required to satisfy the Von Mises criterion for polycrystal ductility, the ⟨100⟩ slip direction defines only three independent slip systems in NiAl.

In comparison, FeAl has the same crystal structure and very close lattice parameter but the principal slip direction is ⟨111⟩ at room temperature [24, 25]. In order to activate the ⟨111⟩ slip, new NiAl alloys containing a small percentage of Fe were studied to reduce the APB energy and promote the dissociation of the ⟨111⟩ dislocation into $1/2$⟨111⟩ superpartials [84]. However, the improved ductility at room temperature through microalloying was found to be only related to an increased mobility of the ⟨100⟩ dislocations. An alternate approach to solve the ductility problem is to use a ternary alloy based on Fe-Ni-Al. A recent study by Koss [88] indicates that composition in the range Ni-35Al-12Fe has the ordered B2 structure of NiAl and a polycrystal shows 1-2% tensile ductility at room temperature.

Atomistic simulations of dislocations and shear fault energies have been conducted in our group for NiAl and FeAl [53, 56]. The embedded atom potentials developed for these two B2 compounds were fitted to increasing APB values from FeAl to NiAl. The results of the dislocation simulations showed that the ⟨100⟩ dislocation dissociates into two $1/2$⟨111⟩ superparials in FeAl. In contrast, the same dislocation in NiAl does not dissociate. This phenomena agreed with the preferred ⟨111⟩ slip direction experimentally observed in FeAl.

150

In order to extend these results to the ternary alloy Ni-35Al-12Fe, development of an inter-atomic potential for Fe-Ni was necessary.

The objective of the present work was to develop embedded atom potentials that would enable atomistic simulation in the ternary Ni-Al-Fe. The lattice parameter, cohesive energy and elastic constants were predicted for B2 Ni-35Al-12Fe.These properties depend on the actual arrangement of atoms in the disorder solution. Based on the different possible atomic distributions, the properties computed were average values obtained for randomly distributed arrangements. The simulation results for the $\langle 100 \rangle$ screw dislocation were then compared with the behavior of the same dislocation in NiAl and FeAl.

## 7.3 SIMULATION TECHNIQUE

### 7.3.1 Embedded Atom Method for Ternary Systems

In addition to the pairwise potential contribution to the energy of the system, the embedded atom method also includes an embedding energy function of the local electronic density that each atom experiences due to the nearby atoms. The energy of the system is then written as:

$$E = \sum_{i,j} V(r_{ij}) + \sum_i F(\rho_i)$$
$$\overline{\rho}_i = \sum_{i,j} \rho(r_{ij})$$

where V is the pair potential, F is the embedding function, $\rho$ is the electronic density function, $\overline{\rho}_i$ is the density at atom i due to all its neighbors and $r_{ij}$ is the interatomic distance between atom i and j considered.

By definition, the pair term includes only interactions between two atoms at a time and therefore can be calculated on the basis of the binary interactions involved in the three binary systems that constitute the ternary system in question. The embedding function is defined separately for each of the components of the ternary system and therefore does

not require any additional fitting beyond that done for the pure components. The local electronic density is calculated as the sum of contributions of each neighboring atom and depends only on the strength of individual contributions of each of the three components, without any further information that corresponds to the ternary system.

It follows that if one has embedded atom potentials for the three binary systems involved in a particular ternary, one should be able to study the ternary system. The only requirement is that the interatomic interaction used for each of the pure components in the description of the two binaries involving that constituent be the same. Thus, in the Ni-Al-Fe it is required that the binary system Ni-Al be described using the same Al-Al interactions as in Fe-Al and the same Ni-Ni interactions as used in Fe- Ni. Similarly, the Fe-Fe functions used in Fe-Al binary potentials should be the same as those used in the Fe-Ni interactions. Although not a necessary condition, we chose to impose that all three constituent interatomic potentials be in effective pair form. In our fitting, there is no input that is specific to the ternary system. The behavior of the ternary is entirely inferred from the binaries through the embedded atom formalism.

### 7.3.2  Interatomic Potentials For Pure Metals and Binary Compounds

For Al-Al, Ni-Ni and Ni-Al interactions, the functions developed for B2 NiAl were used [53]. For Fe-Fe and Fe-Al, the functions developed for B2 FeAl were used [56]. The development of these functions was based on the interatomic potentials for pure Al and Ni originally described by Voter et al. [4] and the functions for pure Fe developed by Simonelli [57]. The construction of the pair potential function for Fe-Ni formed a part of this study and was obtained through a linear combination of the pair potential functions for pure Fe and pure Ni previously used in our studies on NiAl and FeAl [53, 56].

The mixed pair interaction potential for Fe-Ni was obtained by empirically fitting a combination of the pure metals effective pair interactions $V_{Ni}^{eff}$ and $V_{Fe}^{eff}$ . The general

form was as follows:

$$V_{NiFe}^{eff}(a + bx) = A[xV_{Fe}^{eff}(c + dx) + (1 - x)V_{Ni}^{eff}(e + fx)] \qquad (7.1)$$

where $x$ takes values from zero to unity .The values of a, b, c, d, e, f, A and B were fitting parameters and are given in Table 7.1. These parameters were fitted to predict stability of the disordered $Fe_{50}Ni_{50}$ FCC phase. The lattice parameter and cohesive energy for the disordered FCC were fitted to the average value of the lattice parameters and cohesive energies of FCC iron (0.3642nm, 4.28 eV) and FCC nickel (0.352 nm, 4.46) obtained with the potentials for pure metals. The pair potential function obtained is represented in Figure 7.1. The properties predicted for the Fe-Ni system are reported in Table 7.2.

### 7.3.3  Perfect Lattice Properties Predicted for B2 Ni-35Al-12Fe

For the study of the ternary alloy Ni-35Al-12Fe, a technique involving a random number generating routine was used and the results were statistically analyzed. The block of atoms initially created was only composed of nickel atoms. Then, nickel atoms were substituted randomly with 12 % of iron and 35 % of aluminum atoms. Because the B2 crystal structure has two sublattices, the control of the sublattice occupancy for the substitution strongly influenced the ternary alloy properties. It was found that the lowest cohesive energy was obtained for substitution of aluminum in a different sublattice than iron. Therefore, these substitution rules were applied to limit the random substitutions. As a result, 12% of the sublattices 1 were occupied with iron, 35% of the sublattices 2 were occupied with aluminum and rest of the crystal was nickel .

The properties of the perfect crystal were computed in a block of 250 atoms and the calculations were repeated for 500 different seeds for the random number generator. The use of 1000 different seeds did not show significant differences in the results. The analysis of the results gave a reliable average value of the energy for the ternary alloy and a measure local energy variations due to the chemically disordered nature of the alloy.

The lattice parameter, cohesive energy and elastic constants computed for Ni-35Al-12Fe
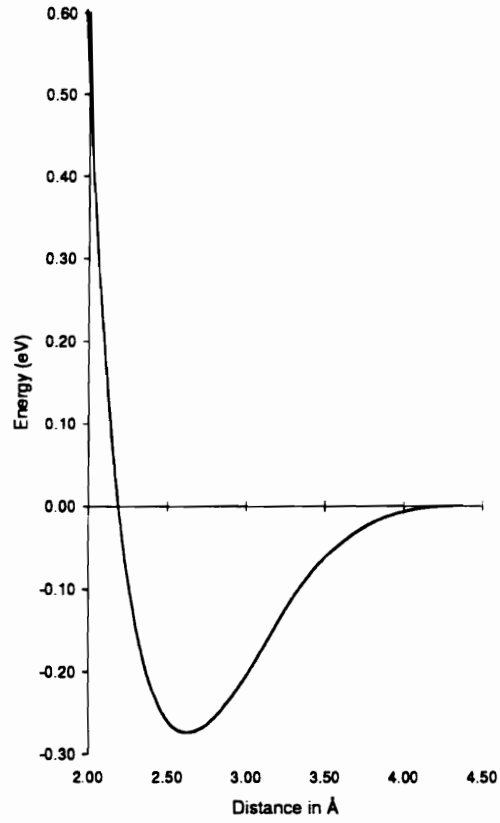
153

Figure 7.1: Pair potential function for Fe-Ni interactions.

Table 7.1: Parameters obtained for the function describing mixed interaction Fe-Ni. Energies are given in eV, and distances in $10^{-1}nm$.

| a | b | c | d | e | f | A |
|---|------|------|------|---|------|-----|
| 1 | 3.33 | 0.99 | 3.01 | 1 | 3.78 | 1.2 |

are presented in Table 7.3 in comparison with the NiAl [53] and FeAl [56]. The standard deviation for the cohesive energy of the ternary alloy was close to 0.1% and the maximum deviation was around ±0.3% from the average. This distribution corresponds to a variation of the total energy of the block of 250 atoms that can reach ±3 eV. This energy distribution is large in comparison with the energy of crystal defects.

The lattice parameter obtained was smaller than in NiAl and FeAl. This result agrees with the experimental observations of a decreasing lattice parameter of NiAl with increasing iron content in the ternary alloy [89]. The high cohesive energy for the composition studied also agree with the stability of this alloy.

## 7.4   SIMULATION OF ⟨100⟩ SCREW DISLOCATIONS IN Ni-35Al-12Fe

The technique to simulate the dislocations was the same as the one previously used for B2 NiAl [46, 47]. The core structures of the ⟨100⟩ screw dislocation were simulated in Ni-35Al-12Fe for different atomic distributions. A total of 17 dislocation core structures were simulated to study the effect of the atomic distribution of the behavior of the dislocation. The core structure presented in this study were plotted using the relative displacement map originally developed by Vitek [43].

All dislocations simulated were introduced in the center of the block of atoms as a complete dislocation. However, the dislocation always spontaneous dissociated into two 1/2⟨111⟩ superpartials in the {110} plane. The distances between the two superpartials varied with the local distribution of the alloy components. The statistical distribution of these separation distances indicates that the average equilibrium distance is probably between 0.6 and 0.8 nm (see Figure 7.2). These distances are larger than the one observed in the simulation of the same dislocation in NiAl and smaller than in FeAl [53, 56]. It is then predicted that the average value of the APB in the {110} plane is between the values computed for NiAl ($286 mJ/m^2$) and FeAl ($115 mJ/m^2$).

The core structures of the superpartials were planar (see Figure 7.3) or non-planar (see

Table 7.2: Properties obtained for the different phases of Fe-Ni. (a is the lattice parameter and $E_{coh}(eV)$ is the cohesive energy.

| Phase | Properties | Embedded Atom Results |
|---|---|---|
| Disordered FCC | a (nm) | 0.36 |
| | $E_{coh}(eV)$ | 4.40 |
| Ordered L1$_0$ | a (nm) | 0.286 |
| | $E_{coh}(eV)$ | 4.39 |
| Disordered BCC | a (nm) | 0.286 |
| | $E_{coh}(eV)$ | 4.38 |

Table 7.3: Properties obtained with embedded atom potentials for the ternary alloy Ni-35Al-12Fe, B2 NiAl and B2 FeAl. (a is the lattice parameter and $E_{coh}(eV)$ is the cohesive energy.

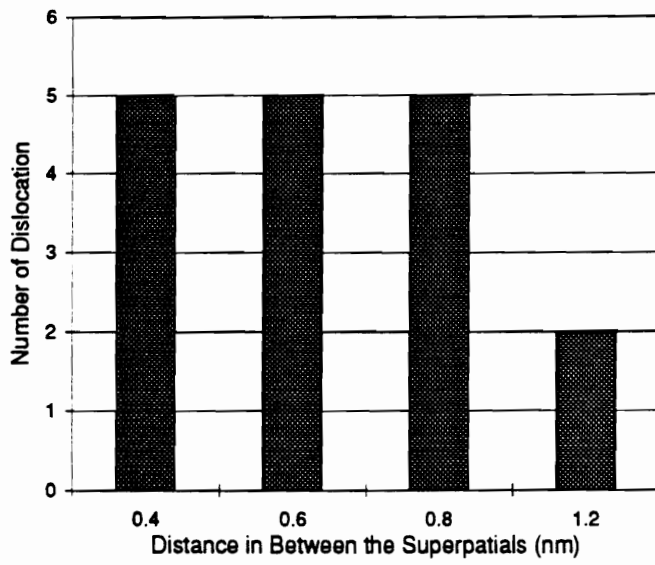| Properties | Ni-35Al-12Fe | NiAl | FeAl |
|---|---|---|---|
| a (nm) | 0.2857 | 0.2876 | 0.291 |
| $E_{coh}(eV)$ | 4.57 | 4.49 | 4.16 |
| $c_{11}$ (eV Å$^{-3}$) | 0.8 | 1.16 | 1.2 |
| $c_{12}$ (eV Å$^{-3}$) | 0.79 | 0.77 | 0.75 |
| $c_{44}$ (eV Å$^{-3}$) | 0.73 | 0.77 | 0.73 |

Figure 7.2: Number of dislocation as a function of the distance between the two $1/2\langle 111\rangle$ superpartials.

Figure 7.4) with a core spreading extended in the two perpendicular {110} planes. The core structures were more complex when the dislocations were closely dissociated (Figure 7.5). Some pairs of superpartials also moved together away from the initial position of the complete dislocation. This behavior indicates that the superpartials are very mobile since they can move easily to a region of the alloy where their stability is increased by the local distribution of the components. Therefore, it is believed that the transition from a sessile to glissile core structure has a low energetic barrier.

## 7.5   CONCLUSIONS

Embedded atom potentials were derived for the ternary system Ni-35Al-12Fe. These potentials were based on the function previously developed for B2 NiAl and B2 FeAl. The only new function needed for the ternary alloy was for the Fe-Ni interactions. These interactions were described as an average of the properties of pure FCC Fe and Ni and did not contain any information on the properties of the ternary alloy. Nevertheless, the properties obtained for Ni-35Al-12Fe were in good agreement with experimental observations.

The spontaneous dissociation of the $\langle 100 \rangle$ screw dislocation into two $1/2\langle 111 \rangle$ superpartials simulated in the ternary alloy is a behavior typical of FeAl. The distance between the superpatials were in a range of 0.4 nm to 1.2 nm indicating that the local value of the APB energy in the {110} plane is probably between the APB values for FeAl and NiAl. Both sessile and glissile core structures were obtained in our simulations. However, it is believed that the energetic barrier for the transition from non-planar to planar core structures is low. These results are in agreement with the observation of a more ductile behavior in the B2 Ni-35Al-12Fe ternary alloy than in NiAl.

$$[1\bar{1}0]$$
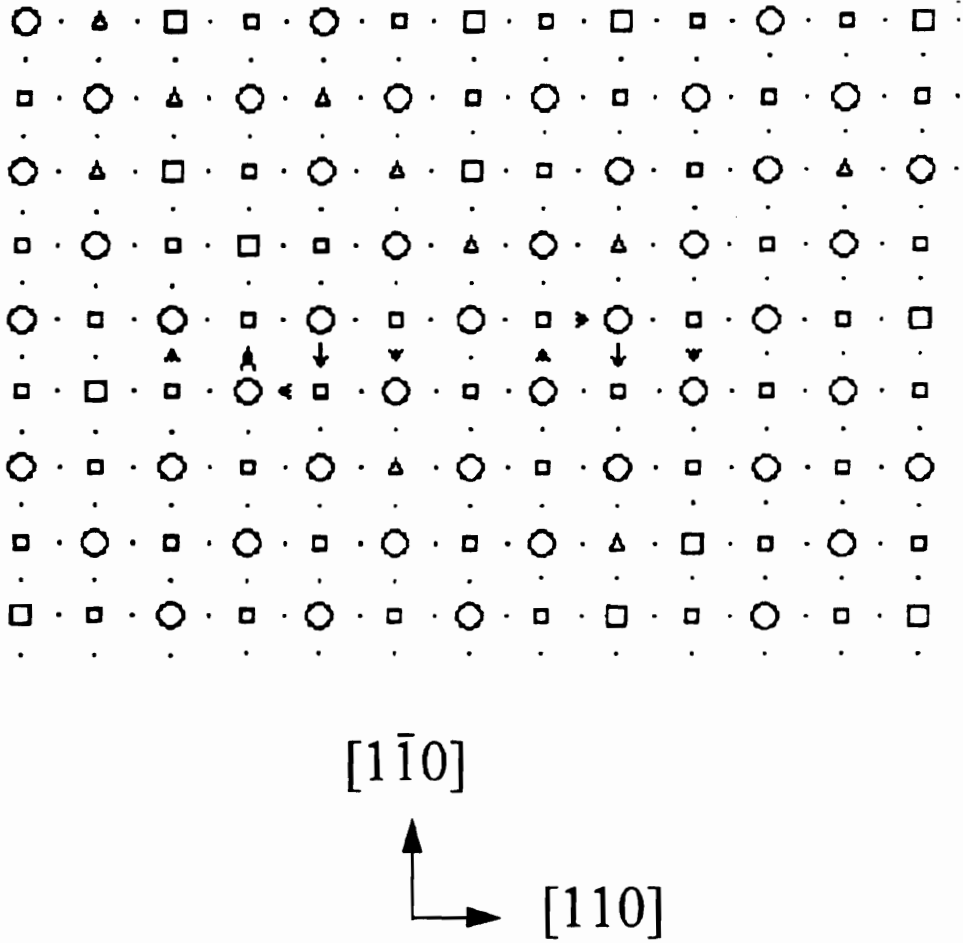
$$[110]$$
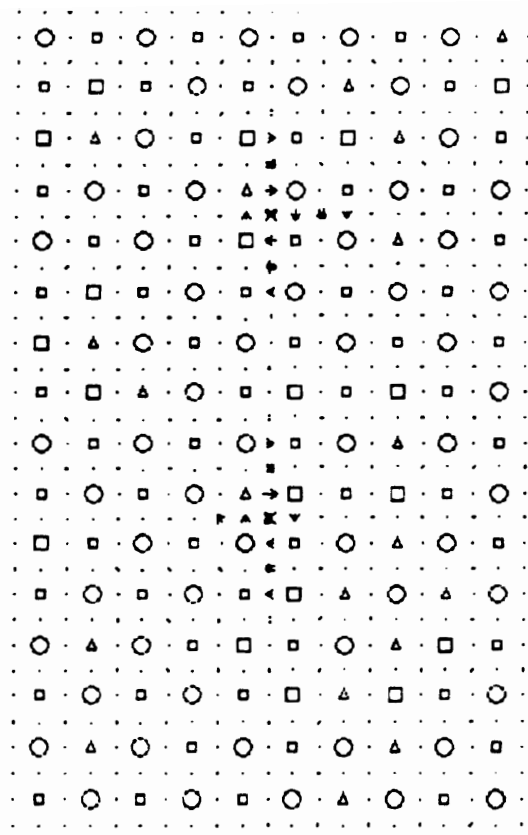
Figure 7.3: Planar cores of the $\langle 111 \rangle$ superpartials; $\triangle = Fe$, $\bigcirc = Al$, $\square = Ni$

159

$$[1\bar{1}0]$$

$$[110]$$
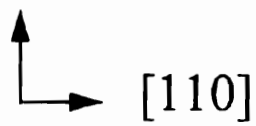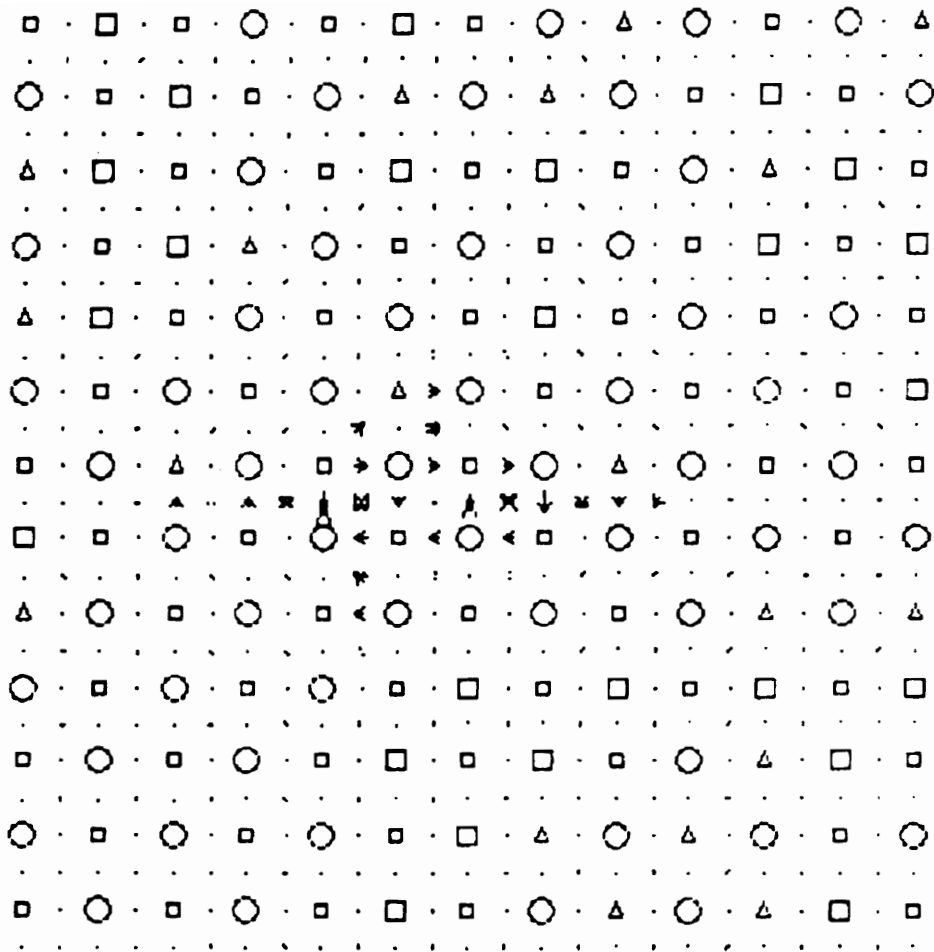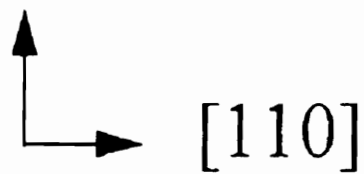
Figure 7.4: Non-planar cores of the ⟨111⟩ superpartials; $\triangle = Fe$, $\bigcirc = Al$, $\square = Ni$

160

Figure 7.5: Complex core structures of the ⟨111⟩ superpartials ; $\triangle = Fe$, $\bigcirc = Al$, $\square$=Ni

# Chapter 8
# CONCLUSIONS

-The stable planar faults in NiAl, FeAl and CoAl deviated from the APB faults in both {110} and {112} planes. These phenomena may actually be quite general for B2 alloys and independent of the particular potential used, since they were found for all the compounds studied.

-According to the unstable stacking fault energy values, it was predicted that the preferred slip direction is $\langle 111 \rangle$ and the preferred slip plane is {110} in all the B2 compounds simulated.

-Stable fault energies and unstable stacking fault energies follow the trend of increasing APB energies along the series FeAl-NiAl-CoAl in both {110} and {112} planes.

-Two criteria for brittle to ductile transition, based on the values of the unstable stacking fault energies and free surface energies, were applied to the series of B2 aluminides. These two criteria ($\gamma_{us}/\gamma_s$ and $\gamma_{us}/\mu b$) generally increased from FeAl to CoAl, following the trend of increasing APB energies and decreasing fracture toughness.

-In contrast with NiAl, the $\langle 111 \rangle$ screw dislocations spontanously dissociated in CoAl and FeAl. These results were in good agreement with the experimental observations of the $\langle 111 \rangle$ slip in CoAl and FeAl at room temperature. It was also predicted that the transition from $\langle 111 \rangle$ to $\langle 100 \rangle$ slip with increasing temperature in FeAl is the result of increasing cross-slip activity.

-Dissociation of the $\langle 100 \rangle$ dislocation into two $1/6\langle 223 \rangle$ partials was only observed in FeAl. This dissociation does not violate Frank's rule.

-Planar cores were obtained for the $\langle 100 \rangle$ screw dislocations in NiAl, CoAl and FeAl. The analysis of the shear in these planar cores indicated a continuous transition from dissociated

162

to complete dislocations, which follows the trend of increasing APB energies from FeAl to CoAl. This continuous transition was found to be related to the fact that the core spreading path tends to avoid the positions of high shear fault energies. As a result, these planar core structures cannot be described with the Peierls-Nabarro model.

-This study confirmed that planar core structures are in general more mobile than the non-planar ones. The mobility of the non-planar dislocations in FeAl, NiAl and CoAl strongly depends on the low levels of deformation of the dislocation cores.

-The spontaineous dissociation of the $\langle 100 \rangle$ screw dislocation into two $1/2\langle 111 \rangle$ super-partials simulated in the ternary alloy is a typical behavior of FeAl. The local value of the APB energy in the $\{110\}$ plane was predicted to be between the APB values for FeAl and NiAl. Both sessile and glissile core structures were obtained in our simulations. However, it is believed that the energy barrier for the transition from non-planar to planar core structure is low. These results are in agreement with the observation of a more ductile behavior in the B2 Ni-35Al-12Fe ternary alloy than in NiAl.

-The in-situ deformation of a single crystal of NiAl only revealed the motion of $\langle 100 \rangle$ dislocations along the $\{110\}$ and $\{100\}$ planes. Both in-situ observation and atomistic simulation agreed on the zig-zag shape of the $\langle 100 \rangle$ dislocation with an average screw orientation. A mechanism of dislocation pinning was proposed for the dislocations with a zig-zag shape.

-The experimental observations in NiAl of a continuous flow of dislocations emitted from the crack tips are characteristic of a ductile material.

# REFERENCES

[1] P. Nash, M. Singleton, and J. Murray, *Phase Diagrams of Binary Nickel Alloys*, 1991.

[2] D. Miracle, Acta Metallurgica et Materialia **41**, 649 (1993).

[3] D. Farkas, B. Mutasa, C. Vailhé, and K. Ternes, Modelling and Simulation in Materials Science and Engineering **3**, 201 (1994).

[4] A. Voter and S. Chen, Accurate interatomic potentials for Ni, Al and $Ni_3Al$, in *Materials Research Society Symposium Proceedings*, volume 82, pages 175–180, 1987.

[5] F. Froes, C. Suryanarayana, and D. Eliezer, ISIJ International **10**, 1235 (1991).

[6] D. Dimiduk, D. Miracle, Y. Kim, and M. Mendirata, ISIJ International **31**, 1223 (1991).

[7] I. Baker and P. Munroe, Properties of B2 compounds, in *High Temperature Aluminides and Intermetallics*, edited by S. Whang, C. Liu, D. Pope, and J. Stiegler, page 425, TMS, Warrendale, PA 15086, 1990.

[8] S. Ashley, Mechanical Engineering **Dec.**, 49 (1991).

[9] J. Larsen, K. Williams, S. Balsone, and M. Stucke, in *High Temperature Aluminides and Intermetallics*, page 521, Mineral, Metals and Materials Society, 1990.

[10] M. Yamaguchi, Materials Science and Technology **8**, 299 (1992).

[11] S. Naka and M. T. anf T. Khan, Materials Science and Technology **8**, 291 (1992).

[12] T. Khan, P. Caron, and S. Naka, in *High Temperature Aluminides and Intermetallics*, page 219, Mineral, Metals and Materials Society, 1990.

[13] C. Liu, C. White, and J. Horton, Acta Metallurgica et Materialia **33**, 213 (1985).

[14] G. Meier and F. Pettit, Materials Science and Technology **8**, 331 (1992).

[15] R. Noebe, R. Bowman, and M. Nathal, International Materials Reviews **38**, 193 (1993).

[16] C. Fu and M. Yoo, Acta Metallurgica et Materialia **40**, 703 (1992).

[17] Y. Zhang, S. Tonn, and M. Crimp, Deformation structures in oriented NiAl and CoAl single crystals deformed at elevated temperature, in *Materials Research Society Symposium Proceedings*, volume 288, pages 379–384, 1993.

[18] K. Chang, R. Darolia, and H. Lipsitt, Acta Metallurgica et Materialia 10, 2727 (1992).

[19] D. Yaney and W. Nix, Journal of Materials Science 23, 3088 (1988).

[20] D. Yaney, A. Pelton, and W. D.Nix, Journal of Materials Science 21, 2083 (1986).

[21] C. Drelles, M.S. Thesis, Mich. Tech. Univ. (1985).

[22] C. Liu, E. Lee, and C. McKamey, Scripta Metallurgica et Materialia 23, 875 (1989).

[23] Y. Umakoshi and M. Yamaguchi, Philosophical Magazine A 41, 573 (1980).

[24] Y. Umakoshi and M. Yamaguchi, Philosophical Magazine A 44, 711 (1981).

[25] M. G. Mendiratta, H.-M. Kim, and H. A. Lipsitt, Metallurgical Transactions A 15, 395 (1984).

[26] H. Xiao and I. Baker, Scripta Metallugica et Materialia 28, 1411 (1993).

[27] I. Ray, R. Crawford, and D. Cockayne, Philosophical Magazine 21, 1027 (1970).

[28] M. Crimp and K. Vedula, Philosophical Magazine A 63, 559 (1993).

[29] J. Hirth and J. Lothe, *Theory of Dislocations, 2nd edition*, Wiley & Sons, 1982.

[30] M. Yamaguchi, V. Vítek, and D. Pope, Philosophical Magazine A 43, 1027 (1981).

[31] T. A. Parthasarathy, S. I. Rao, and D. Dimiduk, Philosophical Magazine A 67, 643 (1993).

[32] D. Farkas and C. Vailhé, Journal of Materials Research 8, 3050 (1993).

[33] M. Loretto and R. Wasilewski, Philosophical Magazine 23, 1311 (1971).

[34] P. Veyssiere and R. Noebe, Philosophical Magazine A 65, 1 (1992).

[35] A. Ardell, *Intermetallic Compounds, Principles and Practice*, volume 2, chapter 12, J. Wiley, 1993.

[36] M. Sluiter, P. Turchi, F. Pinski, and G.M.Stocks, Materials Science and Engineering A 152, 1 (1992).

[37] T. Hong and A. Freeman, Journal of Materials Research 7, 68 (1992).

[38] R. Pasianot, D. Farkas, and E. Savino, Physical Review B 43, 6952 (1991).

[39] P. Clapp et al., in *Materials Research Society Symposium Proceedings*, volume 133, page 29, 1989.

[40] A. Rao, C. Woodward, and T. Parthasarathy, Empirical interatomic potentials for $L1_o$ TiAl and B2 NiAl, in *Materials Research Society Symposium Proceedings*, volume 213, pages 125–130, Materials Research Society, 1991.

[41] C. Lloyd and M. Loretto, Physica Status Solidi (a) **39**, 163 (1970).

[42] J. Kim and R. Gibala, in *High Temperature Ordered Intermetallic Alloys*, volume 213, page 261, Materials Research Society, 1991.

[43] V. Vítek, R. Perrin, and D. Bowen, Philosophical Magazine **21**, 1049 (1970).

[44] V. Vítek and D. Srolovitz, editors, *Atomistic Simulation of Materials*, Plenum, New York and London, 1989.

[45] M. Yamaguchi and Y. Umakoshi, 1983.

[46] R. Pasianot, D. Farkas, and E. Savino, Dislocation core structure in ordered intermetallic alloys, in *Journal de Physique III*, volume 1, pages 997–1014, 1991.

[47] D. Farkas, R. Pasianot, E. Savino, and D. Miracle, Comparison of TEM observations with dislocation core structure calculations in B2 ordered compounds, in *Materials Research Society Symposium Proceedings*, volume 213, pages 223–228, Materials Research Society, 1991.

[48] K. Ternes, D. Farkas, and Z. Xie, Atomistic simulation of dislocation motion as determined by core structure, in *Materials Research Society Symposium Proceedings*, volume 350, pages 293–298, 1994.

[49] M. Norgett, R. Perrin, and E. Savino, Journal de Physique **F2**, L73 (1972).

[50] M. Daw and M. Baskes, Physical Review B **29**, 6443 (1984).

[51] J. Rose, J. Smith, and J. Ferrante, Physical Review B **28**, 1835 (1983).

[52] S. Foiles, M. Baskes, and M. Daw, Physical Review B **33**, 7983 (1986).

[53] D. Farkas, Modelling and Simulation in Materials Science and Engineering **2**, 975 (1994).

[54] S. Foiles and M. Daw, Journal of Materials Research **2**, 5 (1987).

[55] P. Khadikikar, I. Locci, K. Vedula, and G. Michal, Metallurgical Transactions A **24**, 83 (1993).

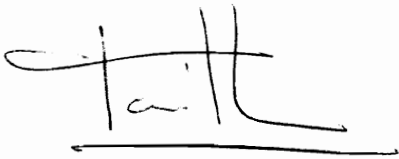[56] C. Vailhé and D. Farkas, Shear faults and dislocation core structures in B2 FeAl, to be published.

[57] G. Simonelli, R. Pasianot, and E. Savino, in *Materials Research Society Symposium Proceedings*, volume 291, page 567, 1993.

[58] R. Harrisson, F. Spaepen, A. Voter, and A. Chen, in *Innovations in Ultrahigh-Strength Steel Technology*, edited by G. Olson, M. Azrin, and E. Wright, page 651, Plenum, 1990.

[59] R. Jhonson and D. Oh, Journal of Materials Research **4**, 1195 (1989).

[60] D. Farkas, S. Zhou, C. Vailhé, B. Mutasa, and J. Panova, Embedded atom calculations of unstable stacking fault energies and surface energies in intermetallics., accepted, to be published in Journal of Materials Research.

[61] P. Villas and L. Calvert, *Pearson's Handbook of Crystallographic data for Intermetallic Phases*, Materials Park,OH : ASM International, 2nd edition, 1991.

[62] D. Oh and R. Johnson, Journal of Materials Research **3**, 471 (1988).

[63] M. Igarashi, M. Khantha, and V. Vítek, Philosophical Magazine B **63**, 603 (1991).

[64] R. Pasianot and E. Savino, Physical Review B **45**, 12704 (1992).

[65] C. Vailhé and D. Farkas, Shear faults and dislocation core structures in B2 CoAl, submitted to Journal of Materials Research.

[66] R. Hultgren, P. D. Desai, D. T. Hawkins, M. Gleiser, and K. K. Kelly, *Selected Values of Thermodynamic Properties of Binary Alloys*, ASM, Metals Park, OH, 1973.

[67] S. Bafuk, M.S. Thesis, Mich. Tech. Univ. (1981).

[68] M. Mehl, J. Osburn, D. Papaconstantopoulos, and B. Klein, First principles calculations of the equilibrium mechanical properties of simple metals and ordered intermetallic alloys, in *Materials Research Society Symposium Proceedings*, volume 186, page 277, 1991.

[69] J. Panova and D. Farkas, Effects of angular dependent terms in the interatomic potential on defect properties in TiAl, in *Materials Research Society Symposium Proceedings*, volume 364, pages 151–156, 1995.

[70] V. Vítek, Philosophical Magazine **18**, 773 (1968).

[71] J. Rice, Journal of the Mechanics and Physics of Solids **40**, 239 (1992).

[72] S. Zhou, A. Carlsson, and R. Thomson, Physical Review Letters **72**, 852 (1994).

[73] M. Finnis and J. Sinclair, Philosophical Magazine A **50**, 45 (1984).

[74] Y. Sun, G. Beltz, and J. Rice, Materials science and Engineering A **170**, 67 (1993).

[75] D. Yaney, A. Pelton, and W. Nix, Journal of Materials Science **21**, 2083 (1986).

[76] Z. Xie, C. Vailhé, and D. Farkas, Materials Science and Engineering A **170**, 59 (1993).

[77] C. Vailhé and D. Farkas, Shear faults and dislocation core structures in B2 CoAl, to be published.

[78] A. Fourdeux and P. Lesbats, Philosophical Magazine A **45**, 81 (1982).

[79] C. Feng and K. Sandananda, Scripta Metallugica et Materialia **24**, 2107 (1990).

[80] G. Molenat, Ph.D. Dissertation, Universite Paul Sabatier de Toulouse, France (1991).

[81] G. Molenat and D. Caillard, Philosophical Magazine **64**, 1291 (1991).

[82] G. Molenat and D. Caillard, Philosophical Magazine **65**, 1327 (1992).

[83] M. Legros, A. Couret, and D. Caillard, In-situ observations of prismatic glide in ti$_3$al, in *Materials Research Society Symposium Proceedings*, volume 288, page 323, Materials Research Society, 1993.

[84] M. Morris, J. Perez, and R. Darolia, in *High Temperature Ordered Intermetallic Alloys*, volume 364, page 413, Materials Research Society, 1995.

[85] V. Vítek, Crystal Lattice Defects **5**, 1 (1974).

[86] F. Nabarro, Proc. Phys. Soc. **59**, 256 (1947).

[87] G. Schoeck, Philosophical Magazine **69**, 1085 (1994).

[88] J. Kostrubanic, L. Breedis, D. Koss, I. Locci, and J. Poole, The influence of processing and thermal history on the properties of nial-based alloys containing iron, Submitted to International Symposium on Structural Intermetallics.

[89] H.Lipson and A. Taylor, in *Proceedings of the Royal Society.*, volume A, page 232, Royal Society, 1939.

# VITA

The author was born on August 11th, 1967 in Bordeaux (France). He completed his undergraduate studies in Physical Chemistry, graduating from the University of Bordeaux I in 1990. In September 1990, "Frenchy" left the city of wine to join the Departement of Materials Science and Engineering at Virginia Tech where he completed a Master's degree. In October 1992, he joined the French Army for ten months and returned to Virginia Tech in 1993 to join the Materials Engineering Science Ph.D. Progam.

Christophe N.P. Vailhé